# Point Spread Function Reconstruction for Next Generation Adaptive Optics Systems

by

Onur Keskin
B.Sc. Yildiz Technical University, 2000
M.A.Sc. University of Victoria, 2003

A Dissertation Submitted in Partial Fulfillment of the
Requirements for the Degree of

DOCTOR of PHILOSOPHY

in the Department of Mechanical Engineering

Point Spread Function Reconstruction for Next Generation Adaptive Optics Systems

By

Onur Keskin

B.Sc., Yildiz Technical University, 2000

Supervisory Committee

Dr. Colin Bradley, Supervisor
(Department of Mechanical Engineering)

Dr. Sadik Dost, Departmental Member
(Department of Mechanical Engineering)

Dr. Andrew Rowe, Departmental Member
(Department of Mechanical Engineering)

Dr. Jean-Pierre Véran, Outside Member
(NRC, Herzberg Institute of Astrophysics)

Dr. Laurent Jolissaint, External Member
(University of Leiden, Leiden Observatory)

**Supervisory Committee**

Dr. Colin Bradley, Supervisor
(Department of Mechanical Engineering)

Dr. Sadik Dost, Departmental Member
(Department of Mechanical Engineering)

Dr. Andrew Rowe, Departmental Member
(Department of Mechanical Engineering)

Dr. Jean-Pierre Véran, Outside Member
(NRC, Herzberg Institute of Astrophysics)

Dr. Laurent Jolissaint, External Member
(University of Leiden, Leiden Observatory)

# Abstract

In adaptive optics (AO) applications, point spread function (PSF) is defined as the impulse response of the system, and the PSF reconstruction is used in calibrating image analysis techniques for astrometry and in the deconvolution of images to enhance their contrast. The partial correction provided by the AO systems is due to the finite sampling of the wavefront sensor (WFS), the deformable mirror (DM) and the finite bandwidth of the overall system. This partial correction is mainly due to the high spatial frequencies introduced by the atmospheric turbulence, which translates into a halo artifact on the

PSF. Furthermore, the correction provided by the AO system in direction of target objects degrades at greater angular distances from the guide star. This is called anisoplanatism. Consequently, the dimmer details of the AO images may not be detectable. One possible way to counteract this halo effect is through PSF reconstruction. In order to achieve accurate results, the analysis of the AO corrected images must account for the PSF temporal variation. The most promising and reliable technique to achieve PSF reconstruction is to use the wavefront sensor data measured synchronously with the observation (AO exposure).

With the off-axis PSF reconstruction from a dual DM AO system as a general objective, a model based experimental evaluation of PSF reconstruction from classical AO systems has been performed. Building on the success from on-axis classical AO systems, the complexity of the model and the experimental set-up has been gradually increased to a multi DM AO system and a methodology has been proposed. The good agreements between the numerical and experimental evaluation of the reconstructed PSF comparisons ensured the successful implementation of the methodology. Last, the complexity of the analysis and of the model is further extended from a single light source to a multi-light source scheme, and the off-axis PSF reconstruction is achieved from a dual DM AO scheme in order to accommodate for the anisoplanatic errors.

One of the challenges in interpreting PSF over wide fields arises from the temporal and field-dependent evolution of the adaptive optics PSF. The methodologies described in this thesis allow a quantitative analysis of wide-field observations that can account for these effects. The outcome of this research is important for post-processing of images obtained by next generation AO systems. Although the results are unique to the UVic

experimental AO bench, the proposed PSF reconstruction methodologies will be applicable to other dual DM systems and to multi DM AO systems. More precisely, the importance of this thesis is to offer a PSF reconstruction technique for the adaptive optics instruments for the Thirty Meter Telescope (TMT). Once operational in 2016, TMT will be the first extremely large ground based optical telescope. It will have a primary mirror diameter of 30 m.

# Table of Contents

# List of tables

# List of Figures

# Nomenclature

| | |
|---|---|
| **AO** | Adaptive Optics |
| **CCD** | Charge Coupled Device |
| **CFHT** | Canada-France-Hawaii Telescope |
| **DM** | Deformable Mirror |
| **ELT** | Extremely Large Telescope |
| **FWHM** | Full-Width at Half Maximum |
| **GS** | Guide Star |
| **HIA** | Herzberg Institute of Astrophysics |
| **MEMS** | Micro-Electromechanical Systems |
| **NFIRAOS** | Narrow Field Infrared Adaptive Optics System |
| **NRC** | National Research Council of Canada |
| **OTF** | Optical Transfer Function |
| **PSD** | Power Spectral Density |
| **PSF** | Point Spread Function |
| **RMS** | root-mean-square |
| **SH** | Shack-Hartmann |
| **SH WFS** | Shack-Hartmann Wavefront Sensor |
| **SLODAR** | Slope Detection and Ranging |
| **SR** | Strehl Ratio |
| **TMT** | Thirty Meter Telescope |
| **WFS** | Wavefront Sensor |

# Acknowledgments

I would like to thank a number of people for their support and contribution towards my Ph.D. program. I would like to thank my supervisor *Dr. Colin Bradley* for his motivation and encouragement, for the funding that he provided and for the guidance he gave me towards success. The broad scope of the AO test-bench required the contributions of several other researchers for success. I would like to thank *Dr. Rodolphe Conan* for his work on control-system development, for software development, and inputs towards the project. I also would like to extend my gratitude to *Dr. Sadik Dost* and *Sema Dost* for their support through my master's and Ph.D. program.

In an academic quest such as this, it is critical to have moral support and friendship to enjoy life along the way. I would like to thank all my friends, members of *UVic Adaptive Optics* and *Ocean Technology Laboratories* who have made this time valuable.

Family is the oldest and most fundamental human institution. I would like to thank all the members of my family for their love and support.

Finally, I would like to express my deep and eternal gratitude to my mother *Dr. Fügen Keskin* and to my father *Dr. Haluk Keskin* for their support and encouragement through every step in my life.

# Dedication

*To my grandmother,*

*Nurten Göknar*

*&*

*In loving memory of my grandfather,*

*Korgeneral Fikret Göknar*

# 1. Introduction

In astronomical applications, *adaptive optics* refers to optical systems that compensate in real time for wavefront aberrations introduced by the atmospheric turbulence between the object of interest and its image on the science detector. Writing in *Opticks* in 1730, Isaac Newton [1] described the problem of atmospheric turbulence and its limitation on astronomical observations:

> "For the Air through which we look upon the Stars, is in a perpetual Tremor; as may be seen by the tremulous Motion of Shadows cast from high Towers, and by the twinkling of the fix'd Stars."

The development of military telescopes for observing satellites (in the late 1960s) laid the groundwork for the development of basic adaptive optics (AO) systems that correct the effects of turbulence. In 1991, much of the military work was declassified [2] and AO concepts started to be applied in the astronomical community. The effects of atmospheric blurring can be avoided by using telescopes in space; however, facilities like the Hubble Space Telescope (HST) are extremely costly to build and operate, and have relatively small apertures that limit their light-collecting power. The HST cost 20 times more to build and launch than a 10-meter ground-based telescope. If a ground-based telescope employs AO, however, it has 20 times the light-gathering power and potentially 4-5 times better resolution.

The concept of adaptive optics was first proposed by Babcock [3] in 1953. AO was defined as a method of using a deformable optical element called a deformable mirror (DM) that corrects for the phase aberrations in the incoming wavefront. In this

architecture, the DM is driven by wavefront sensor measurements. The role of the WFS is to detect the degree of aberration in the wavefront. This basic operating principle has not changed.

The effect of atmospheric turbulence on a telescope's ability to image distant stars is called *seeing*. To understand the importance of this thesis and of the PSF reconstruction techniques in general, one has to realize that even though we are able to correct for seeing effects with AO systems, first, the correction is only partial, and second, it varies across the field, depending on the distance to the guide stars. Consequently, when doing analysis of the AO-corrected science images (morphology, photometry and the astrometry of objects) the PSF variation has to be taken into account, via, for instance, image deconvolution, in order to get accurate results. It is therefore mandatory to have a calibrated PSF model across the corrected field. Unfortunately, because seeing is highly variable, calibrating the PSF with pre- or/and post-observation of bright stars across the field does not give reliable results. The PSF calibration should therefore be done during the AO exposure itself. Reconstructing the PSF from wavefront sensor data is certainly the most promising and reliable technique to achieve this objective. The research goal of this Ph.D. research can be defined as an accurate estimation of the PSF for various adaptive optics schemes that will be used in the next-generation telescopes.

## 1.1 Adaptive Optics Systems Overview

### 1.1.1 Wavefront Phase Distortions

Figure 1 illustrates the wavefront transformation from a star to its arrival on a telescope aperture. If one considers a planar wavefront of light passing through a vacuum, a slice across this wavefront will contain a flat pattern of phase, which will move uniformly at the speed of light in the direction of the beam. If the beam passes through a uniform medium, its speed is slowed by refractive index fluctuations, but the phase relationship is unchanged and it still moves together. In the free atmosphere, however, the speed of light will vary as the inverse of the refractive index. The light propagating through regions of high index will be delayed compared to the light propagating through other regions. Therefore, the wavefront will no longer be flat but distorted.

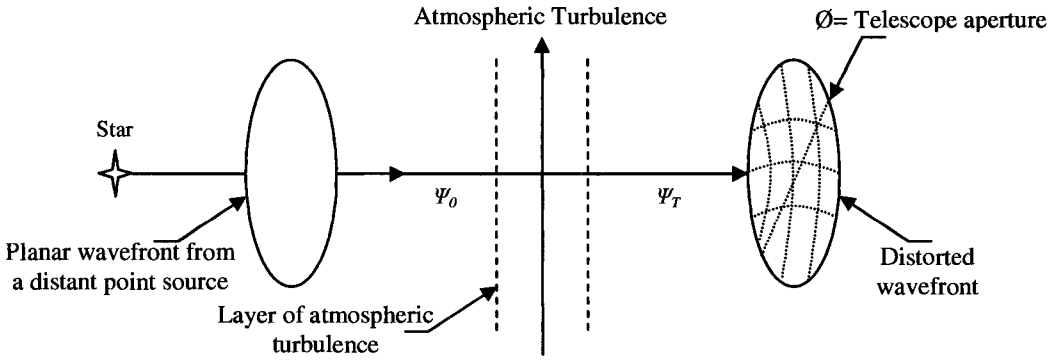


**Figure 1: Transformation in a wavefront from a star to the telescope aperture due to the atmospheric turbulence layer containing air pockets of variable temperature and refractive index.**

A wavefront can be described by a complex number, $\Psi$, called the wave complex amplitude. A planar wavefront generated by a point source can be described as

$$\Psi_0 = A\, e^{i\varphi} \tag{1.1}$$

where $A$ is the wave amplitude, and $\varphi$ is the phase of the field fluctuation. A surface over which $\varphi$ takes the same value is called the wavefront surface. A distorted wavefront (e.g., after the wavefront has passed through the layer of atmospheric turbulence shown in Figure 1), can be defined as

$$\Psi_T = A\, e^{i\varphi(r,\rho,\, t)} \tag{1.2}$$

where $r$ and $\rho$ are two points in the telescope pupil plane, and $t$ is time.

In an optical system, it is sometimes useful to present the phase ($\varphi$) as a 2D surface over a circular pupil (e.g., telescope pupil). The derivation from the flat (planar) wavefront is the wavefront error and is conveniently represented by a series of orthogonal polynomials over the circular pupil.

A commonly used series is the Zernike series, described in Appendix E. The specific properties of the Zernike polynomials that are useful for optical systems are:

- The root mean square (rms) can be defined as the statistical measure of the magnitude of a varying quantity. One property of the Zernike modes is that they have an rms error over the telescope pupil.
- Zernike polynomials form a complete orthogonal set, which provides a convenient way of expanding an arbitrary function into an infinite series over a circular area.

The series efficiently represents well-known optical aberrations such as tip, tilt, defocus, astigmatism and coma. Figure 2 shows graphs of the first six modes of aberration represented by these polynomials.

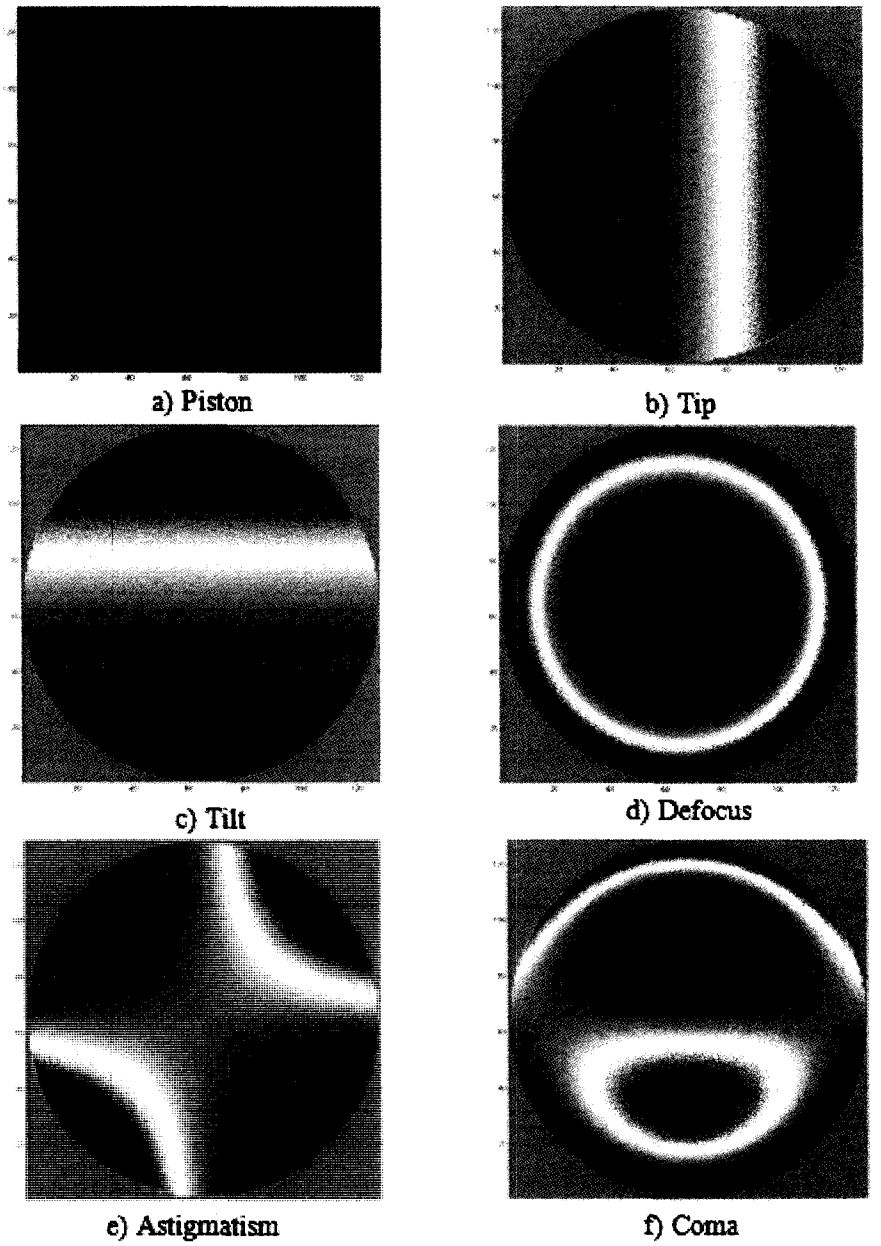


**Figure 2: (a) *Piston*: A typical unsensed mode is the piston mode, which is a constant-phase value across the surface of the deformable mirror; (b) *Tip*: The imaging consequence of tip is to shift the image on the x-axis; (c) *Tilt*: The imaging consequence of tip is to shift the image on the x-axis; (c) *Tilt*: The imaging consequence of tip is to shift the image on the y-axis; (d) *Defocus*: The imaging consequence of defocus is the image degradation; (e) *Astigmatism*: The imaging consequence of astigmatism is the orientation-dependent shift of focus; (f) *Coma*: The imaging consequence of coma is the image asymmetry and pattern-dependent shift of image.**

### 1.1.2 Wavefront Phase Measurement

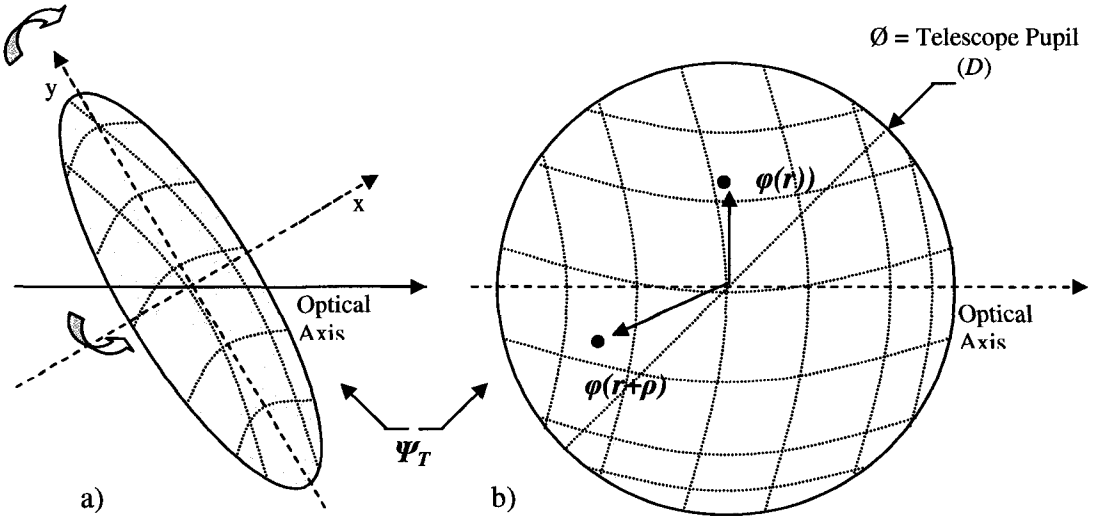


**Figure 3: Illustration of the structure function of the atmospherically introduced phase aberration: (a) wavefront phase with tip/tilt modes; (b) wavefront phase when tip/tilt modes are removed.**

The wavefront error can be more conveniently described as having two major components:

1. Tip/tilt modes, which are the aberrations containing the largest component of the wavefront error shown in Figure 3(a).
2. All the higher modes above tip/tilt as shown in Figure 3(b).

Figure 3 shows the snapshot of a wavefront surface deformation from a top view across the pupil of a telescope with a diameter $D$. As illustrated in this figure, from the phase fluctuations in different points across the telescope's pupil, the structure function of the phase aberrations can be computed as the variance of the difference between the value of the phase aberration at a point $\vec{r}$ and the value at a nearby point $(\vec{r}+\vec{\rho})$

$$D_{\varphi}(\vec{\rho}) = \left\langle \left|\varphi(\vec{r}+\vec{\rho}) - \varphi(\vec{r})\right|^2 \right\rangle_D \tag{1.3}$$

where, $D_{\varphi}(\rho)$ is the atmospherically induced variance of the phase aberration field at two points within the telescope's aperture plane ($D$). Here $<\ldots>_D$ represents the radial average over the pupil.

As described earlier, a surface over which $\varphi$ takes the same value is called a wavefront surface.

The deformation on the wavefront surface after turbulence can be given as

$$\delta = \int n(z)dz \tag{1.4}$$

where $n(z)$ is the refractive index fluctuation along the beam that travels through atmospheric turbulence. It must be noted that the deformation on the wavefront surface is generally expressed in microns or nanometers.

The phase fluctuations is related to wavefront surface deformation by

$$\varphi = k \int n(z)dz \tag{1.5}$$

where $k$ is the wave number ($2\pi/\lambda$), and $\lambda$ is the wavelength of the incoming beam.

As shown in Figure 4, the wavefront error is measured by a device called the wavefront sensor (WFS). The wavefront sensor measures the slope (the first derivative) of the distorted wavefront surface at each specified sampling point (depending on the specific sensor design). The WFS sampling resolution (the spacing of the sub-apertures) determines the number of Zernike modes that can be measured (i.e., higher WFS resolution enables the system to detect higher frequency modes introduced by atmospheric turbulence).

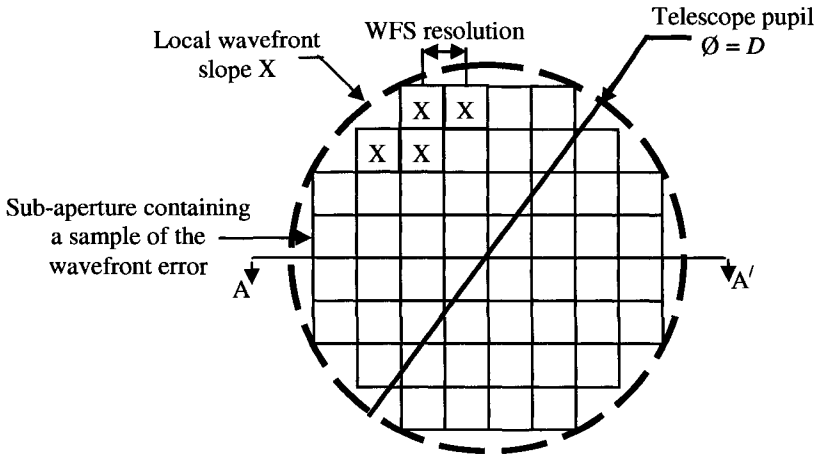


**Figure 4: The schematic design illustration of a wavefront sensor.**

### 1.1.3 Wavefront Phase Correction

A deformable mirror (DM), as shown in Figure 5, is used to correct for the wavefront error aberrations in the incoming wavefront. In adaptive optics, a deformable mirror uses a grid of actuators to deform the physical shape of its reflective membrane to correct the distorted wavefront over the entire pupil, *D*. The location of the actuators typically corresponds to the WFS sub-aperture intersections. The WFS locally measures the wavefront error and under a suitable control scheme, the DM locally corrects for this error. The deformation on the aberrated wavefront surface is a wavelength independent quantity. Consequently, this deformation can be compensated by means of a deformable mirror having the same surface deformation (DM modes) as the incoming wavefront surface but with only half the amplitude (stroke of the DM).

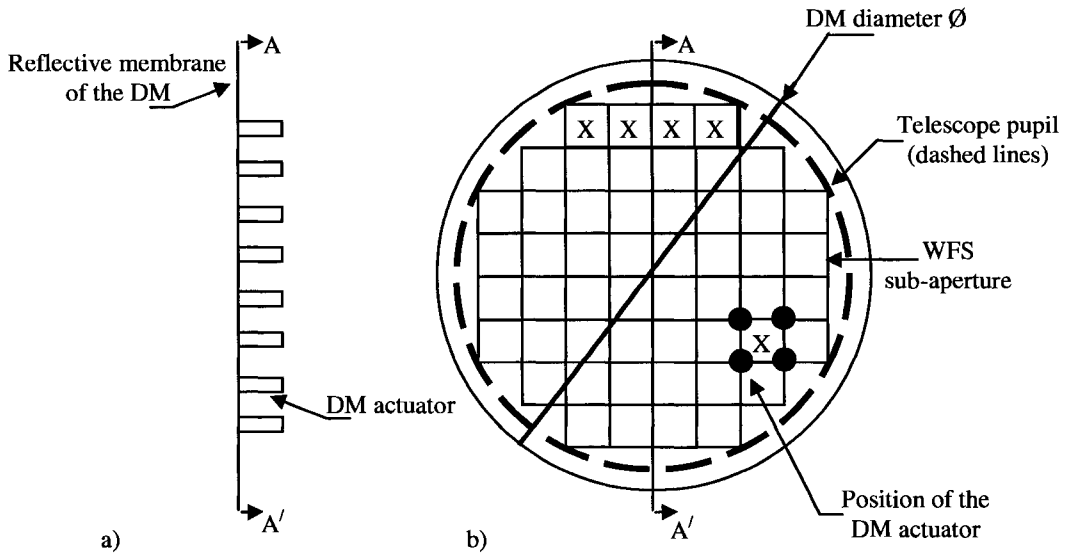


**Figure 5: Schematic diagram of a deformable mirror of diameter Ø: (a) location of the DM actuators with respect to the reflective membrane; (b) registration of the DM with the WFS.**

As described earlier, a distorted wavefront that has passed through the atmospheric turbulence layer is defined as:

$$\Psi_T = A\, e^{i\varphi(r,\rho,\, t)} \tag{1.6}$$

Based on the WFS measurements, the DM attempts to reverse the phase of the distorted wavefront and compensates for the atmospheric turbulence. A perfect phase correction by the DM can be described as the mathematical conjugate of the wavefront error. This means changing the sign of the term behind the imaginary number. This mathematical conjugation corresponds to the phase conjugation of the optical field. For a perfect correction, the DM surface shape can then be defined as:

$$\Psi_{DM} = A\, e^{-i\varphi(r,\rho,\, t)} \tag{1.7}$$

Ideally, the DM surface shape and the wavefront surface shape would cancel and the outcome of an AO correction would result in a planar wavefront but the correction

provided by an AO system is partial. This partial correction is due to the finite sampling of the wavefront sensor, the limited number of degrees of freedom of the DM (i.e., the number of actuators of the DM), and the finite bandwidth of the overall system. Hence, the outcome is not a perfect planar wavefront. There is a residual wavefront error. This is illustrated in Figure 6, where a distorted wavefront propagates through a telescope's pupil plane. The AO system applies the phase conjugate to this distorted wavefront by means of a WFS, a control system and a deformable mirror. The result is an almost flat wavefront that contains residual errors from the AO correction.

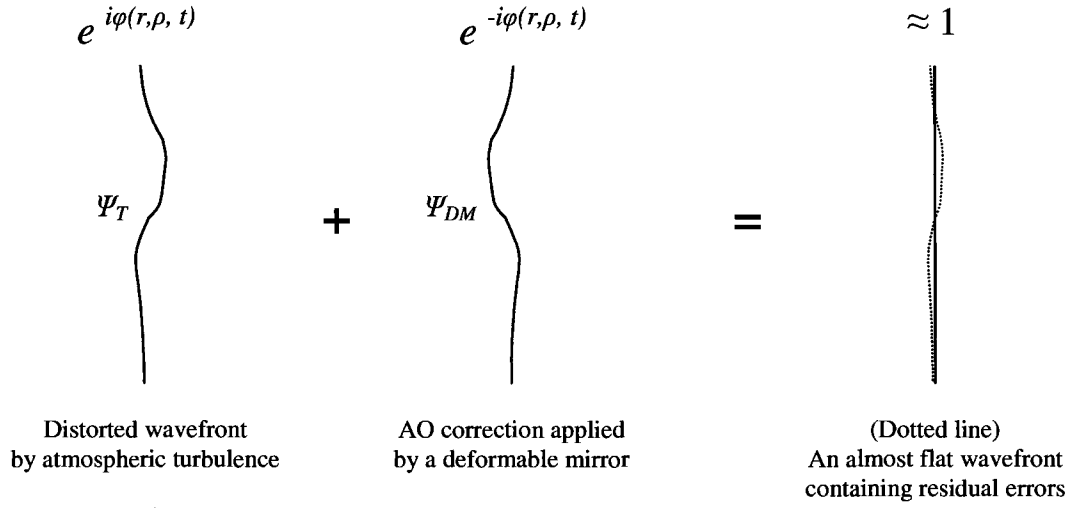


**Figure 6: Illustration of phase conjugation by means of a phase corrector.**

Figure 7 illustrates the transformation of a wavefront from a distant star as it passes through the atmosphere and is corrected by the AO system. When a DM is used on the compensation of a wavefront, each segment of this DM can be approximated as a circular mirror. Each of these segments will correct for the mean value of the phase distortion averaged over the segment area. In wavefront compensation, zonal- or modal-control

methods can be used. In the zonal-control approach, each segment (or zone) of the DM is controlled independently by wavefront measurements corresponding to that zone.

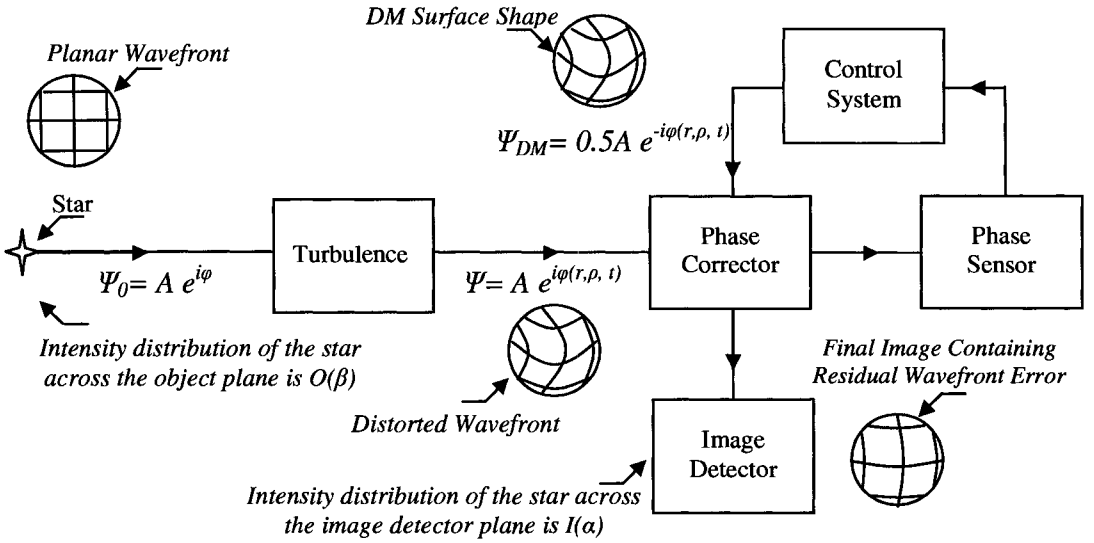


**Figure 7: The schematic illustration of wavefront transformation from a star to the telescope aperture, and through the adaptive optics correction.**

### 1.1.4 Adaptive Optics System Performance

In Figure 8, the temporal power spectrum of atmospheric turbulence is presented. The temporal power spectrum shows behaviour in regimes related to the modes of atmospheric turbulence and its optical effects. In Figure 8 (a), based on Kolmogorov's atmospheric turbulence theory [4], in the low-frequency regime (below the cut-off frequency ($f_c$), the tilt-included phase spectrum follows a (-2/3) power law. Above the cut-off frequency, the power law follows a (-8/3) law. Here the cut-off frequency can be

described as the transition from the forming of large turbulent eddies to their progressive breakdown into smaller eddies. It can be approximated from the turbulence wind velocity, and the telescope's aperture diameter.

$$f_c = 0.7\frac{v}{D} \tag{1.8}$$

where $v$ is the turbulence wind velocity and $D$ is the diameter of the telescope's aperture. In Figure 8(b), the tilt-removed power spectrum follows a (4/3) power law. Atmospheric tilt in x- and y-direction (called tip and tilt) is responsible for almost 87% of the Kolmogorov phase variance (refer to Section 3.4.1). These two modes are compensated for by a separate control loop and by a separate phase corrector called the tip/tilt mirror to achieve the highest possible accuracy.

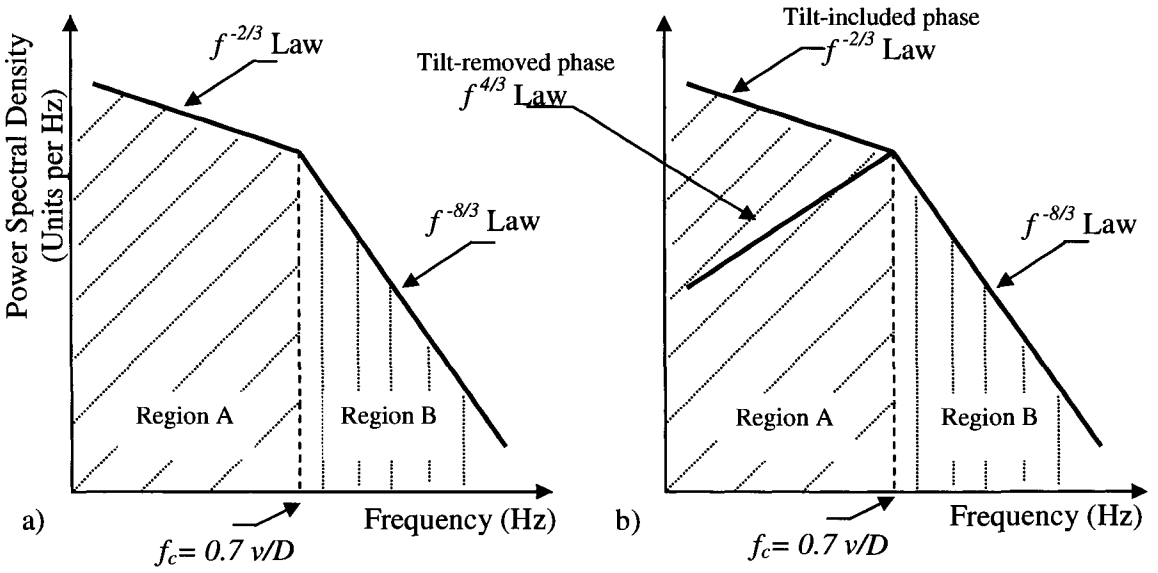


**Figure 8: Power spectral density of the atmospheric turbulence, that exhibits behaviour in regimes related to the modes.**

The diagrams in Figure 8 show two major regions, A and B. In Region A, it can be seen that most of the turbulence energy is concentrated at low spatial frequencies, and requires a large stroke to correct the first modes of the atmospheric turbulence; whereas at high spatial frequencies (Region B), the stroke requirement for the AO correction drops substantially. For next-generation extremely large telescopes, it is planned to use a new AO architecture through dual DMs, the so-called Woofer/Tweeter configuration. In this architecture, the Woofer is a low-order-high-stroke DM used to compensate for the low-frequency effects introduced by atmospheric turbulence. The Tweeter is a high-order-low-stroke DM used to compensate for high-frequency effects.

The adaptive optics system performance can be evaluated by the residual errors of the system components.

- Due to the limited degree of freedom of the phase corrector, the DM cannot exactly match the shape of the atmospheric-turbulence-induced distorted wavefront surface. This is referred as a *fitting error*, shown in Figure 8, Region B.
- The finite sampling of the phase sensor and the delay in the control system result in a delay in compensation for the changes in the atmospheric-induced wavefront distortions. This delay is referred to as *servo-lag error*, shown in Figure 8, Region A.
- The source of the wavefront (i.e., a point source object or a star) used on the calibration of an AO system may be positioned away from the object of interest. Hence, the phase sensor measures slightly different turbulence. This is termed *isoplanatic error.*

- The noise levels of the CCD used as the phase sensor may also limit the accuracy of the measurements. This is referred as *sensor-noise error.*

It can be assumed that all these errors are uncorrelated and have Gaussian random distributions. Therefore, their variance can be summed to determine the overall system error. This system error can be given as:

$$\sigma^2_{system} = \sigma^2_{fitting} + \sigma^2_{servo\text{-}lag} + \sigma^2_{isoplanatic} + \sigma^2_{sensor\ noise} \quad (1.9)$$

where the $\sigma$ is given in square radians.

### 1.1.5 Image Formation through Adaptive Optics

Figure 9 illustrates the bi-dimensional angular vector of the image plane on the image detector as $\vec{\alpha}$, and the bi-dimensional angular vector of the object of interest on the object plane as $\vec{\beta}$. The object plane is considered to be at an infinite distance from the image plane. The angular vectors $\vec{\alpha}$ and $\vec{\beta}$ are orthogonal to the optical axis. The intensity distribution of the object of interest across the object plane is $O(\vec{\beta})$. Similarly, the intensity distribution of the long-exposure image measured on the image detector is $I(\vec{\alpha})$. The formation of an image through an AO system can then be defined as:

$$I(\vec{\alpha}) = \int O(\vec{\beta})\, PSF(\vec{\alpha}, \vec{\beta})\, d\vec{\beta} \quad (1.10)$$

where the PSF can be defined as the response of an imaging system to a point source of light. More generally, the PSF is the impulse response of an optical system. The PSF of a point source coherent light represents the intensity received at the point $\vec{\alpha}$ of the image plane when the point-source object's intensity at position $\vec{\beta}$ is observed.

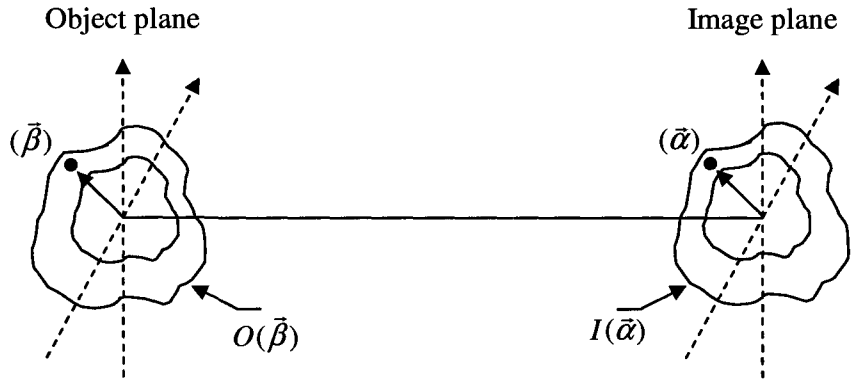


**Figure 9: The relation between the object and the image.**

The isoplanatic patch is the area where the distortion level of the atmospheric turbulence is statistically the same (isotropic) everywhere in the field. It is generally assumed that the long-exposure PSF has the same shape regardless of the viewing direction within this isoplanatic patch. The image formed on the image plane can then be seen as a superposition of points in the image plane. Using the Fredholm approximation, the stationary $PSF\ (\vec{\alpha},\vec{\beta})$ can be described as $PSF\ (\vec{\alpha}-\vec{\beta})$, and the equation above can be rewritten as a convolution:

$$I(\vec{\alpha}) = \int O(\vec{\beta})\, PSF(\vec{\alpha}-\vec{\beta})\, d\vec{\beta} = O(\vec{\alpha}) \otimes PSF(\vec{\alpha}) \tag{1.11}$$

In the Fourier domain, this convolution becomes a product:

$$\tilde{I}(\vec{f}) = \tilde{O}\ (\vec{f})\ .\ OTF\ (\vec{f}) \tag{1.12}$$

where OTF is the optical transfer function of the system. To improve the final AO images, the PSF must be accurately estimated in the post-processing stage. This will be achieved by use of the residual wavefront error data measured by the phase sensor and the commands sent to the phase corrector. Once the PSF is known, by using the PSF and the image ($I$) obtained by the science camera of the adaptive optics system, the object ($O$)

can be partially rebuilt up to the spatial cut-off frequency of the telescope through a deconvolution process. This is shown in Figure 10, where the improvement to the final AO image obtained by the image detector of the AO system is noticeable.

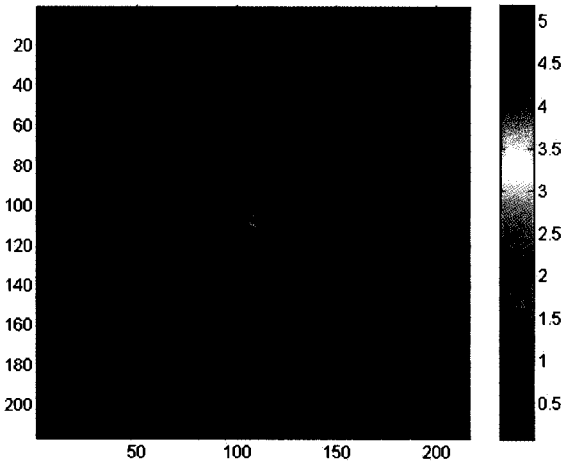


a) Planar wavefront in space

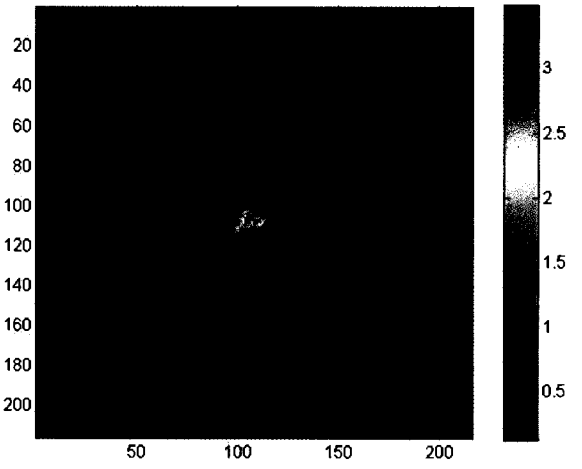


b) Distorted wavefront in atmosphere

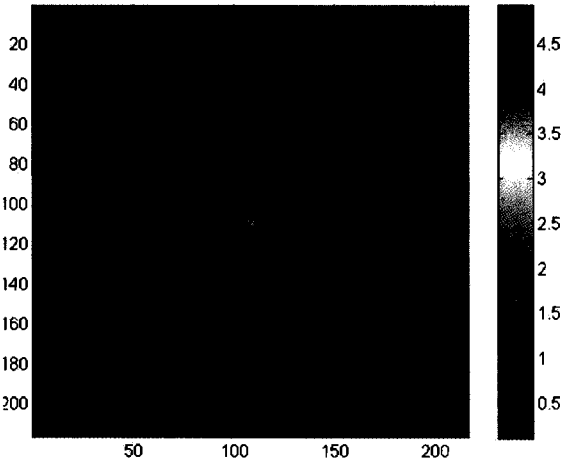


c) AO correction to the distorted wavefront

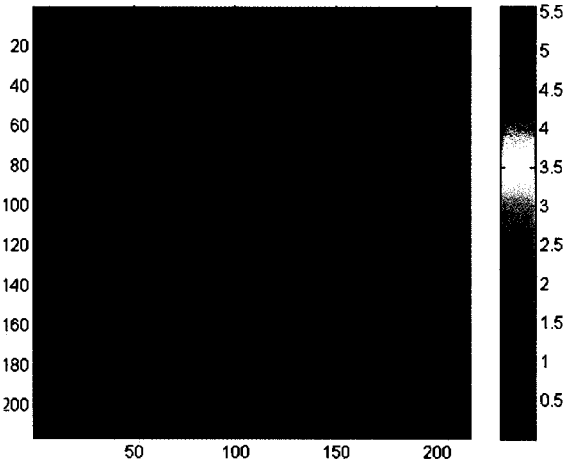


d) Improvement to the final image by PSF deconvolution

**Figure 10: In this figure (a) illustrates a planar wavefront generated by a point source object in space; (b) the wavefront gets distorted by the atmospheric turbulence; (c) the AO system compensates for the distortions but the correction is only partial; (d) once the PSF is accurately estimated, the object image can be re-built up to the spatial cut-off frequency of the telescope.**

## 1.2 Contributions of this Thesis

The principal contributions of this research are in the improved methodology and the new technology.

The first contribution of this thesis is the experimental evaluation of vertical properties of atmospheric turbulence, created in the laboratory environment by the UVic hot-air turbulence generator. In this characterization, slope detection and ranging (SLODAR) methodology has been adapted and experimentally evaluated.

The second contribution is the numerical and experimental evaluation of PSF reconstruction for a classical (single DM) AO system. PSF reconstruction was previously investigated by other researchers, but the methodology is experimentally evaluated for the first time at the UVic AO test-bed. The numerical model is composed of the individual models of the optical elements of a classical AO bench. The end-to-end model is entirely coded in Matlab, where the atmospheric turbulence is introduced by generating phase screens. The experimental evaluation has proved the validity of the adapted methodology.

The third contribution of this thesis is the model-based experimental evaluation of an improved PSF reconstruction methodology for the UVic AO laboratory dual-DM AO test-bed. The methodology has been proposed, implemented, and published. This test-bed is developed at the University of Victoria AO laboratory, and the concept is called Woofer/Tweeter (W/T) architecture. The research concept of having two DMs allows the W/T AO system to have a high degree of correction over a large amplitude wavefront distortion. It must be noted that the proposed method is also applicable to an N number of DMS, and can be adapted to other multi-DM AO systems.

The last contribution is the numerical evaluation of an off-axis PSF reconstruction from a dual-DM AO system. The complexity of both the analysis and the model is extended to a multi-light source scheme. In order to accommodate for the anisoplanatic errors, which degrade the performance of AO systems at greater angular distances from the guide star, the methodology is proposed, implemented, and numerically evaluated. It will also be applicable to multi-DM AO systems.

More precisely, the importance of this thesis is to offer a PSF reconstruction technique for the instruments that will be used on the Thirty Meter Telescope (TMT). When operational in 2016, TMT will be the first extremely large ground-based optical telescope. It will have a primary mirror diameter of 30 m.

## 1.3 Dissertation Organization

In Section 2, the characteristics and effects of the atmospheric turbulence in astronomical observations are discussed. Section 3 gives an overview of AO systems and describes AO systems for large ground-based telescopes. Section 4 will describe the point-spread function of an AO system, and the PSF reconstruction work at the UVic AO Laboratory.

The contribution of this thesis will be presented in four articles:

- O. Keskin, L. Jolissaint, C. Bradley, "Hot air turbulence generator for the testing of adaptive optics systems: Principles and characterization," *Applied Optics*, Vol. 45, issue 20, pp. 4888-4897, (2006).
- O. Keskin, R. Conan, C. Bradley, "Point-spread function reconstruction from woofer/tweeter adaptive optics bench," Proc. of SPIE, *Advances in Adaptive Optics*, Vol. 6272, pp. 62724I, (2006).
- O. Keskin, R. Conan, P. Hampton, C. Bradley, "Derivation and experimental evaluation of a point-spread function reconstruction from a dual deformable mirror adaptive optics system," *Optical Engineering*, Vol. 47 No, 4 (to appear/April 2008).
- O. Keskin, R. Conan, C. Bradley, "Derivation and numerical evaluation of an off-axis point-spread function reconstruction from woofer/tweeter adaptive optics system," *Optical Engineering*, (under review), (2008).

# 2 Effect of Atmospheric Turbulence in Astronomical Observations

Atmospheric turbulence is caused by random variations in temperature and pressure that spatially and temporally alter the air's index of refraction. As electro-magnetic radiation from distant astronomical objects propagates through the atmosphere, the waves of light are distorted by these fluctuations in the refractive index and the information stored in the wavefront is corrupted. For astronomers, this loss of information manifests as degradation in the angular resolution that can be achieved with a ground-based telescope. The images captured by the telescope are blurry when compared to the ideal diffraction-limited resolution of the telescope's imaging optics. In the 20th century, modelling the effects of turbulence on wave propagation received a great deal of attention. The emphasis on building a statistical model of the atmosphere has resulted in several useful theories. The most widely accepted of these theories, due to its consistent agreement with observations, was proposed by Kolmogorov [5] in 1941.

## 2.1 Chapter Overview

This chapter was written as part of the Ph.D. thesis project; it details the effect of atmospheric turbulence in astronomical observations. All important turbulence parameters are thoroughly defined.

The following chapter sections present key parameters used in the characterization of atmospheric turbulence:

- Section 2.2 defines the atmosphere's effect on astronomical observations, called *seeing*. The key parameters used in the measurement of seeing will be introduced.
- Section 2.3 defines the optical effects of turbulence that changes the structure constant of the refractive index in the atmosphere ($C_N^2$) according to *Kolmogorov's theory of optical turbulence.*
- Section 2.4 defines the *Fried coherence length* ($r_0$), which is a widely used descriptor of the level of atmospheric turbulence at a particular site.

## 2.2 Seeing – The Atmosphere's Effect on Astronomical Observations

The effect of atmospheric turbulence on a telescope's ability to image distant stars is called *seeing*. Figure 11 shows a layer of atmospheric turbulence and its effect on a planar wavefront from a distant star. If one considers a planar wavefront of light passing through a vacuum, a slice across this wavefront will contain a flat pattern of phase that will move uniformly at the speed of light in the direction of the beam. If the beam passes through a uniform medium, its speed is slowed by refractive index fluctuations but the phase relationship in unchanged and it still moves together. In a non-uniform medium (e.g., free atmosphere), however, some parts of the wavefront are slowed more than others, leading to distortions in the uniform wavefront. The planar wavefront is progressively distorted by the turbulence and it arrives at the telescope aperture ($D$) containing severe optical aberrations. The degree of distortion is related to the statistical properties of the atmospheric turbulence layers (Region A in Figure 11). The thicknesses of those layers vary from 100 m to a few km.

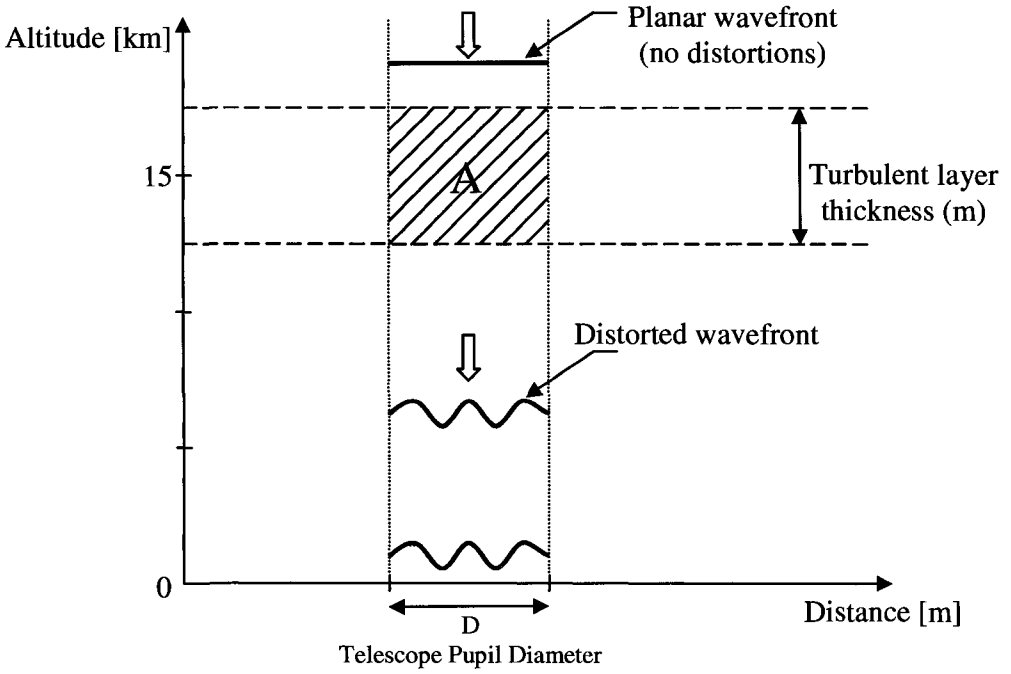


**Figure 11: The effect of atmospheric turbulence on a wavefront.**

The seeing can be quantified by the following set of parameters:

**1) $C_N^2$[h]:** A measure of the strength of the atmospheric turbulence (in $m^{-2/3}$) at a specific location. $C_N^2$ is experimentally evaluated at each telescope location by means of balloons launched to observe the structure of the optical turbulence by measuring the micro-fluctuations of the temperature field and other meteorological parameters, such as wind velocity. The changes in the structure constant of the refractive index ($C_N^2$), within the turbulence Region A, define the strength of the atmospheric turbulence within these layers. The atmospheric turbulence Region A, shown in Figure 11, is further illustrated in Figure 12. The atmosphere can be defined as a fluid in a continuous motion. In laminar flow, fluid particles move along in layers, with one layer sliding over an adjacent layer. Laminar flow is governed by Newton's law of viscosity, which relates shear stress to

angular deformation. In laminar flow, the viscosity dampens out turbulent tendencies. Laminar flow is not stable in situations involving combinations of low viscosity, high velocity, or large flow passages (containing different temperature variables $T_1$ and $T_2$, and wind speeds $V_1$ and $V_2$) and breaks down into turbulent flow. As the flow advances, air parcels with varying velocities and temperatures are brought together by the convective process and the variations in wind and temperature become concentrated in the layers.

The presence of a velocity gradient ($u$) in fluid results in a shear stress in a plane perpendicular to the direction of that gradient. The proportionality constant will be called the viscosity. In a turbulent flow with a certain thickness, $z$, an equation similarly to Newton's law of viscosity can be written:

$$v = \eta \frac{du}{dz} \tag{2.1}$$

where $v$ is the eddy viscosity, and $\eta$ is the viscosity coefficient. Eddy viscosity is the main factor that directs the formation of the boundary layer when fluid flows past a surface. The relative velocity and surface between two fluids in different directions and shearing forces on the surfaces of the fluid velocities result in irregularities, which form a turbulent boundary layer. Taking into account the variations expected between turbulence in the boundary layer and the free atmosphere, the larger-scale atmospheric structures (large-scale turbulent eddies) form. These eddies are associated with the transfer of energy to the turbulent motion.

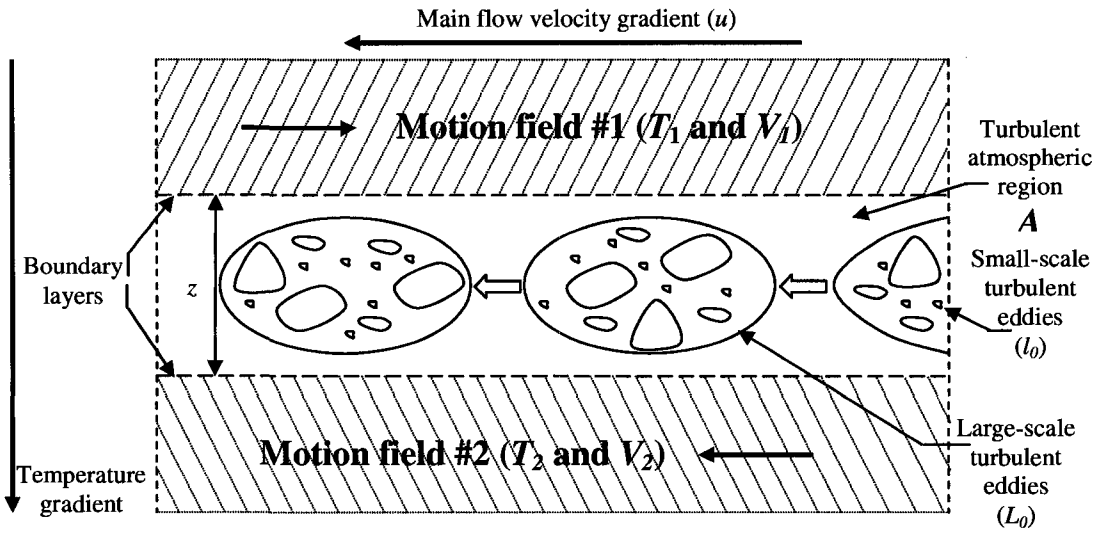


**Figure 12: Turbulent atmospheric Region A.**

**2) Fried's coherence length ($r_0$):** A widely used descriptor of the level of atmospheric turbulence at a particular site. Under atmospheric turbulence, the resolution of a telescope is limited by Fried's coherence length rather than the physical diameter of the telescope's aperture. Fried defined the $r_0$ value as the size of the diameter of a smaller the telescope having the same angular resolution as a big one. It must be noted that even in the best seeing conditions, a large-diameter telescope without adaptive optics does not provide any better resolution than a telescope with a smaller diameter. In Figure 13(a), an image obtained by a telescope of diameter 10 m can be seen in the absence of atmospheric turbulence. The atmospheric turbulence degrades the resolution of an image obtained by a telescope, and this is simulated in order to illustrate the Fried coherence length. In (b) the degradation on the resolution after a long-exposure observation is noticeable. In (c) the telescope's aperture size is 1 m, which is the $r_0$ value simulated in Matlab as also 1 m. Typical $r_0$ values are measured to be within 5 to 20 cm, where 5 cm relates to bad seeing and 20 cm to good seeing.

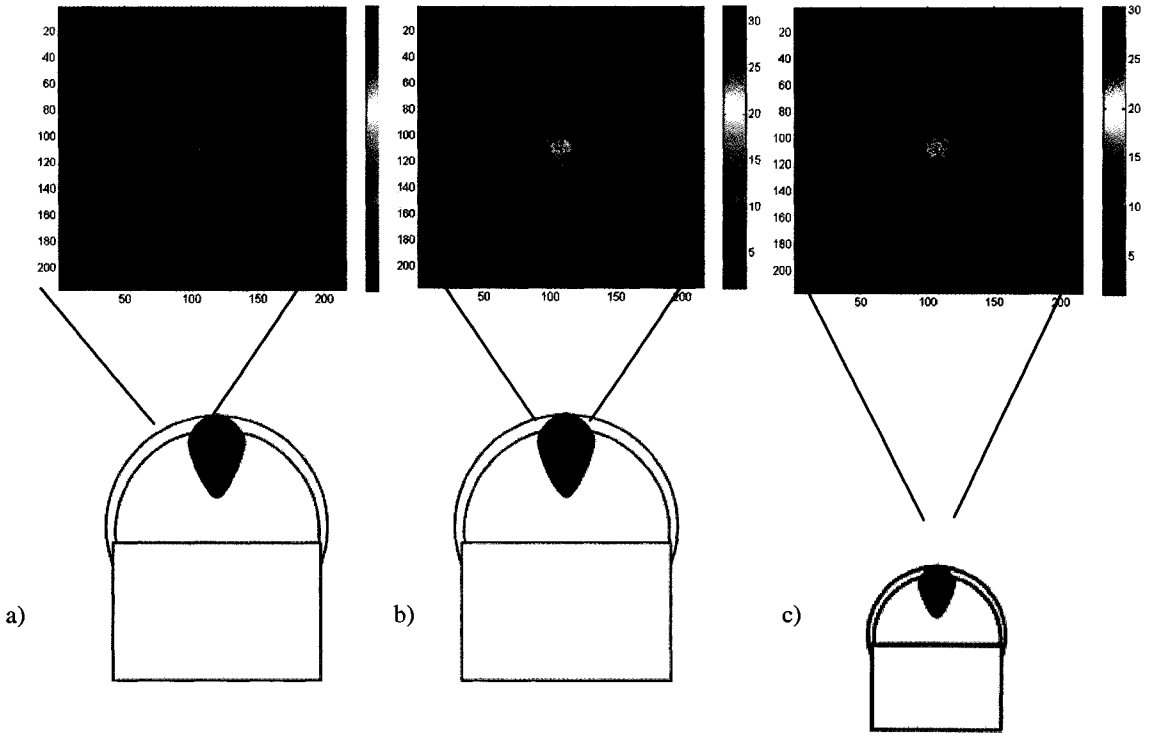


**Figure 13: (a) Resolution of the image in the absence of turbulence obtained by a 10 m telescope: (b) Resolution of the image in the presence of turbulence obtained by a 10 m telescope; (c) Resolution of the image in the presence of turbulence obtained by a 1 m telescope.**

**3) The outer ($L_0$) and the inner ($l_0$) scale of turbulence:** In Figure 14, the energy cascade of atmospheric turbulence is illustrated according to Kolmogorov's theory of atmospheric turbulence. The spatio-temporal properties of the turbulence [5] are as follows: The length of the large turbulent eddies formed by solar heating is called the outer scale of the turbulence ($L_0$). The size of the outer scale varies from 100 m to a few km. In this region, the kinetic energy is injected by a large-scale displacement forced by the wind. These large eddies are characterized by random relative motions of individual fluid volumes with diameters in the order of the characteristic flow dimensions. The velocity of these relative displacements is less than the mean velocity, and they take place

in the low frequencies of atmospheric turbulence. Following a progression over time, the air flow breaks those large eddies into progressively smaller eddies up to an inner spatial scale where the kinetic energy is converted to thermal energy by dissipation, the heat is radiated to space and the cycle is completed. This region is called the inner scale of turbulence ($l_0$), and it represents the high-frequency region of turbulence. The size of the inner scale is measured to approximately 10 cm.

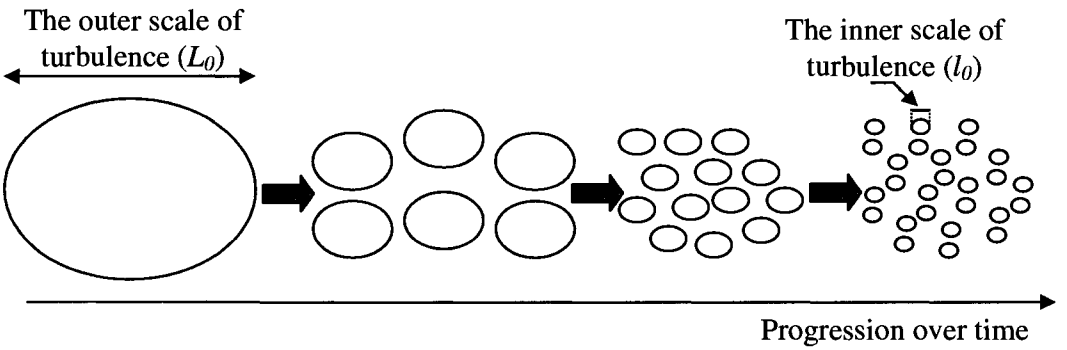


**Figure 14: Energy cascade of the atmospheric turbulence.**

**4) Point-spread function (PSF):** The PSF can be defined as the response of an imaging system to a point source of light. More generally, the PSF is the impulse response of an optical system, and in the absence of atmospheric turbulence, the PSF has a central core width and an angular width proportional to $\lambda/D$, where $\lambda$ is the wavelength of the incoming beam, and $D$ is the telescope's diameter. The atmospheric turbulence degrades the PSF and smears the image, as shown in Figure 13. The fact that the AO system provides only a partial correction due to the limited degrees of freedom of the DM and the spatial sampling of the wavefront sensor, a halo surrounds the core of the PSF with an angular size of roughly $\lambda/r_0$, where $r_0$ represents Fried's coherence length.

**5) Anisoplanatism:** A bright star near the object of interest that the wavefront sensor uses to measure the distortions in the wavefront is called a guide star (GS). In the case of off-axis observations, an AO system senses the degree of aberration in the phase of the incoming wavefront of the guide star (GS) that arises from atmospheric turbulence, and compensates for this aberration. If the final image quality is degraded due to the angular separation between the GS and the object of interest in a different direction, this is called *anisoplanatism.* Figure 15 illustrates anisoplanatism in adaptive optics, which depends on a number of parameters, namely: (i) the vertical distribution of turbulence,(ii) angular offset from the reference source, and (iii) the zenith angle. The vertical distribution of turbulence at higher altitudes generates greater anisoplanatic errors due to the larger geometric cut between the columns of atmosphere (Figure 15, black area). Angular offset between the reference source and the target object ($\theta$) degrades the image quality, and since further turbulence can be encountered along the line of sight to the target object, zenith angle increases the anisoplanatic error.

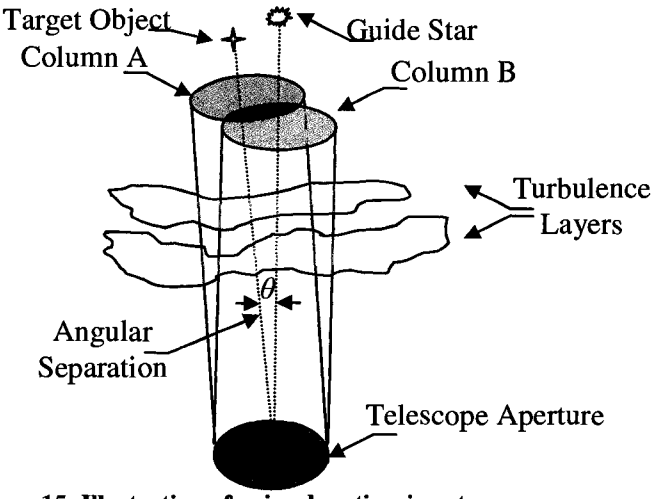


**Figure 15: Illustration of anisoplanatism in astronomy.**

## 2.3 Kolmogorov's Theory of Optical Turbulence

Based on the fundamental Kolmogorov hypothesis, which states that the energy flow rate is constant from larger to smaller eddies, it has been shown that in homogeneous and isotropic turbulence, the temperature fluctuations are assumed to have a Gaussian random distribution [5]. Figure 16 (a) illustrates a snapshot side view of atmospheric turbulence; in the telescope's field of view, eddies with sizes varying from $L_0$ to $l_0$ can be seen. These eddies not only contain varying temperatures but also different refractive indexes. Figure 16(b) shows the snapshot from the top view across the pupil of a telescope with a diameter $D$. From the temperature ($T$), and refractive index ($\alpha$) fluctuations in different points across the telescope's pupil, Tatarski [6] defined a structure function of the temperature field using the variance of the temperature difference between the value of the temperature at a point $\vec{r}$ and the value at a nearby point $(\vec{r}+\vec{\rho})$:

$$D_T(\vec{\rho}) = \left\langle \left| T(\vec{r}+\vec{\rho}) - T(\vec{r}) \right|^2 \right\rangle_D \tag{2.2}$$

where, $D_T(\rho)$ is the atmospherically induced variance of the temperature field at two points in the telescope's aperture plane ($D$). Here $<\ldots>_D$ represents the radial average over the pupil.

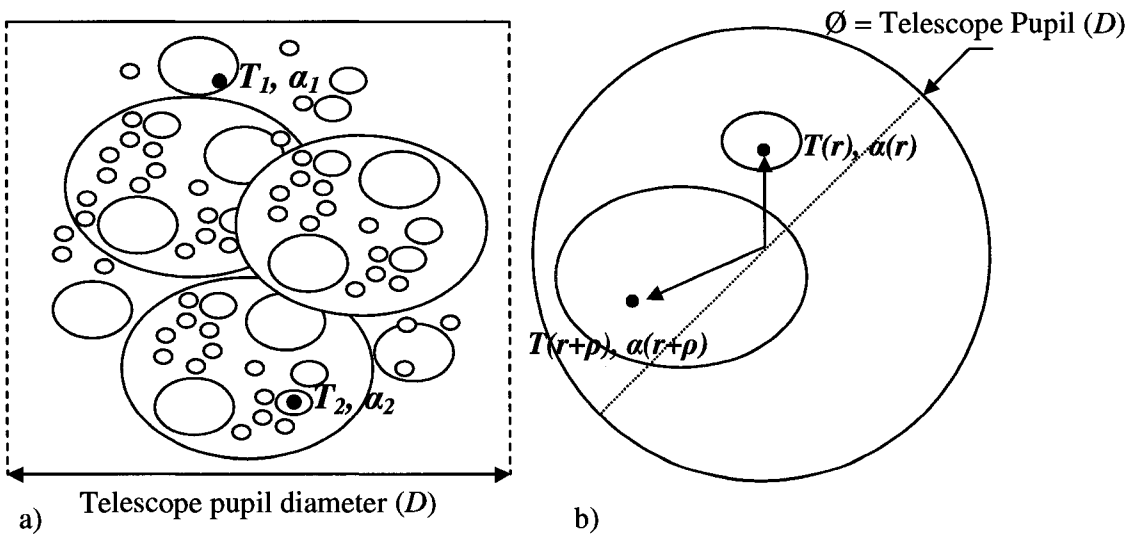


**Figure 16: Illustration of the structure function: (a) snapshot of the side view of atmospheric turbulence; (b) snapshot of the top view of atmospheric turbulence across the telescope's pupil.**

A useful relationship between the structure function of the temperature field and the structure constant of the temperature field is given by Obukhov and Yaglom [7, 8]:

$$D_T(\vec{\rho}) = C_T^2 \rho^{2/3} \tag{2.3}$$

where $C_T^2$ defines the structure constant of the temperature field, and $\vec{\rho}$ is the distance between two points in the pupil. This equation is the starting point for the development of the theory of the optical effects of atmospheric turbulence.

The mixing of air masses at different densities, due to dynamic turbulence, creates a random and turbulent refractive-index field. The refractive-index fluctuation is directly proportional to the air density and temperature as given by the Dale-Gladstone law:

$$N - 1 = \alpha_N P / T \tag{2.4}$$

where $\alpha_{air} = 80.10^{-8} K/Pa$ , $P$ is the air pressure and $T$ the air temperature. The most important parameter is the variance of the difference between the value of the refractive index (Figure 16(b)) at a point $\vec{r}$ and the value at a nearby point $(\vec{r}+\vec{\rho})$. If the temperature field is turbulent, then in a similar manner, the structure function of the refractive ($C_N^2$) index is:

$$D_N(\vec{\rho}) = \left\langle \left| N(\vec{r}+\vec{\rho}) - N(\vec{r}) \right|^2 \right\rangle = C_N^2 \vec{\rho}^{2/3} \tag{2.5}$$

Provided that the separation $\rho$ is smaller than the turbulence outer scale ($L_0$), then:

$$D_N(\vec{\rho}) = C_N^2 \vec{\rho}^{2/3} \tag{2.6}$$

Experimentally, this power law has been found to be accurate for distances of less than 1 m. This random process is both homogeneous (i.e., not position dependent), and isotropic. The structure constant of the refractive index $C_N^2$ can then be linked to $C_T^2$ by:

$$C_N^2 = \left( \frac{\alpha_n P}{T^2} \right)^2 C_T^2 \tag{2.7}$$

and as derived by Tatarski, $C_T{}^2 \sim \Delta T^2$, equation 2.7 becomes [6]:

$$C_N^2 \sim \left( \frac{\alpha_n P}{T^2} \right)^2 (\Delta T)^2 \tag{2.8}$$

where $\Delta T^2$ is the temperature fluctuation variance within the turbulent flow. In Chapter 3, this relation is experimentally proved for the atmospheric-turbulence simulator on the AO test-bed.

## 2.4 Fried's Coherence Length

The Strehl ratio can be defined as the ratio of the peak intensity in the PSF of an optical system to that of the perfect theoretical image that can be obtained from the equivalent system. The Fried [9, 10] coherence length ($r_0$) is defined as the diameter of the telescope having the same Strehl resolution as the atmospheric PSF. In other words, $r_0$ is defined as the diameter of the circular pupil for which the diffraction-limited image and the seeing-limited image obtained from a telescope have the same angular resolution (Figure 13).

The structure function of the phase aberrations was previously given in Equation 1.3. By replacing Equation 1.5 into Equation 1.3, it is possible to express the structure function of the phase aberrations in terms of index structure functions integrated along the sight of the telescope. Using Equation 2.5 for the structure function of the refractive index and performing the integration yields to:

$$D_{\varphi}(\vec{\rho}) = 2.91k^2 \int C_N^2(z)\,dz\,\rho^{5/3} \tag{2.9}$$

where $k$ is the wave number ($k = 2\pi/\lambda$); it varies as the inverse of the wavelength. The remaining integral can be described along the line of sight because it represents the light propagating through the atmosphere until it reaches the telescope's aperture. In Equation 2.10, the dependence of $C_N^2$ can be related to the height of the atmospheric turbulent layer above the ground $h$, and Equation 2.9 can then be rewritten as:

$$D_{\varphi}(\vec{\rho}) = 2.91k^2(\cos\gamma)^{-1} \int C_N^2(h)\,dh\,\rho^{5/3} = 6.88(\rho / r_0)^{5/3} \tag{2.10}$$

where, $\gamma$ is the angular distance of the point source from the zenith. The quantity $(\cos\gamma)^{-1}$ is the air mass, and $r_0$ is the Fried coherence length.

The Fried coherence length is wavelength dependent, and related to the refractive index structure constant [11] by:

$$r_0^{-5/3} = 0.4234(2\pi/\lambda)^2 \int_0^{\infty} C_N^2(h)dh \tag{2.11}$$

where $\lambda$ is the optical-beam wavelength, and $h$ is the height of the atmospheric turbulence layer's height above the ground. In the development of an AO turbulence simulator, the Fried coherence length is experimentally determined. In Equation 2.11, the integral can be replaced by the factor $C_N^2 \Delta h$, where $\Delta h$ is the turbulent layer thickness.

The mean square error of the wavefront phase aberrations over a circular area of diameter $D$ can be calculated by using Equations 2.9 and 2.10:

$$\sigma_1^2 = \left\langle \frac{4}{\pi D^2} \iint_{area} \left|\varphi(x) - \varphi_0(x)\right|^2 dx \right\rangle \tag{2.12}$$

where $\varphi_0$ is the phase-averaged wavefront over the area, and can be given as:

$$\varphi_0 = \frac{4}{\pi D^2} \iint_{area} \varphi(x)\, dx \tag{2.13}$$

According to Fried [9] and Noll [12]:

$$\sigma_1^2 = 1.03(D/r_0)^{5/3} \tag{2.14}$$

Hence, one interesting property of Fried's coherence length is that the root mean square (rms) of the phase distortion over a circular area of diameter $r_0$ is about 1 radian. This will be the starting point for the mean square phase aberration calculations when a plane wave is fitted to the wavefront over this area, and its phase is subtracted from the distorted wavefront phase (removal of Zernike modes) by use of deformable mirrors (refer to Chapter 4).

# 3. Characterization of a Laboratory Atmospheric Turbulence Simulator

This chapter presents a laboratory technique for re-creating the optical effects of atmospheric turbulence on a telescope image. The experimental apparatus is embedded in an AO tes- bed, and the combination of the AO test-bed and turbulence simulator emulates an 8-meter diameter telescope.

## 3.1 Chapter Overview

In Appendix A, the paper *"Hot air turbulence simulator for the testing of adaptive optics systems: Principles and characterization"* was written as part of the Ph.D. thesis project. The article describes the design and implementation of a test-bed turbulence simulator, where the all-important turbulence parameters ($C_N^2$, $r_0$, $L_0$, $l_0$) are characterized for the AO test-bed.

The following chapter sections present key methods and results from this paper:

- Section 3.2 defines the design and implementation of a test-bed turbulence simulator.
- Section 3.3 defines the methods used to extract the Fried coherence length ($r_0$) for the turbulence simulator.
- Section 3.4 defines the effect of outer ($L_0$) and inner scale ($l_0$) of atmospheric turbulence; results obtained from the characterization of the turbulence simulator will be presented.

- Section 3.5 explains the principle of the slope detection and ranging (SLODAR) technique on the AO test-bed. This technique is used to determine the number of turbulent layers within the turbulence simulator.

## 3.2 Design of a Hot-Air Atmospheric Turbulence simulator

To generate real optical turbulence (i.e., turbulent fluctuation of the refractive index), one needs to create dynamic turbulence (i.e., velocity) and temperature fluctuation in the airflow. This is achieved by mixing two airflows with different temperatures in a confined space, the hot-air turbulence simulator. In the laboratory testing of an AO system, the turbulence simulator is a crucial component. It generates the optical effects of the atmospheric turbulence to the wavefront that is used to test the AO control system (Section 4.5).

The top view of the turbulence simulator built at the UVic AO laboratory can be seen in Figure 17. The box is divided into two flow channels with an open mixing zone 17.5 cm in length in the centre. This zone represents the outer scale ($L_0$) of the atmospheric turbulence. The ends of both channels are connected to open pipes to allow air intake and exhaust. Fans and heating elements are used in the forcing of the air, and honeycomb materials are used to laminarise the airflow into the mixing zone of the turbulence simulator.

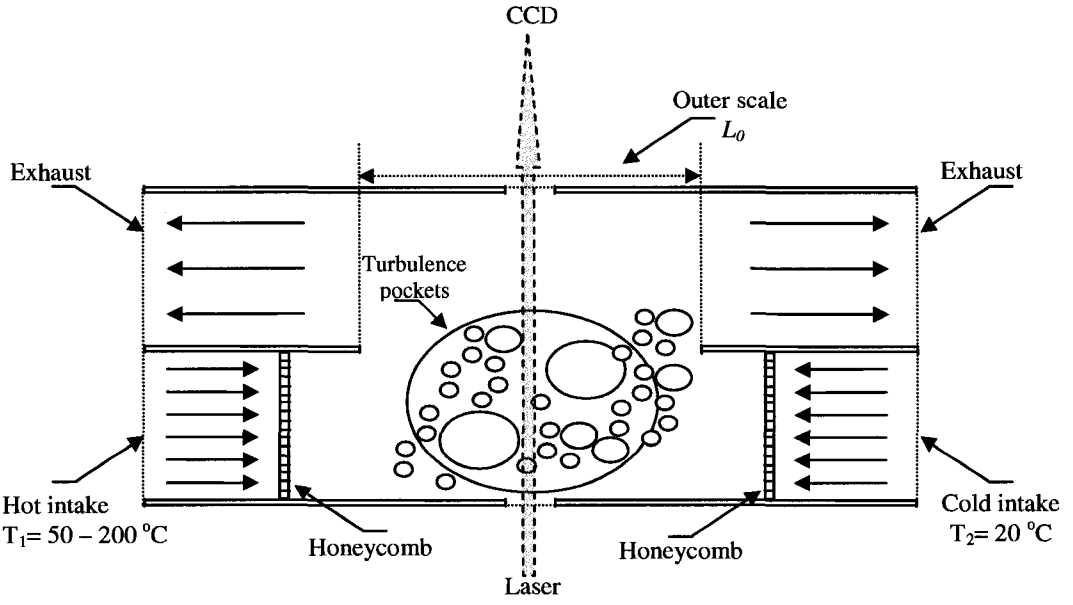


**Figure 17: Schematic diagram of the turbulence simulator. Similarly to Figure 16, the snapshot of turbulence can be seen where the turbulent eddies arise by forcing the air with different temperature and refractive indexes. The inner scale ($l_0$) has been found to be within 7.6±3.8 mm.**

The experimental set-up in the characterization of the emulated turbulence can be seen in Appendix A, Figure 2. The key features of this arrangement are:

- *A collimated laser beam* is created from a point light source (a laser through a spatial filter in the experiment).
- *Neutral density filters* are used to prevent saturation or damage to the CCD chip.
- *A stop* is placed after the turbulence simulator having the role of the entrance pupil on a telescope, with a diameter ($D$).
- *A lens* has the function of simulating the telescope optics as seen from the CCD camera.

- *The long-exposure focused images* of the turbulent beam are collected by the CCD camera for the full width at half-maximum experiment (FWHM).

The FWHM experiment has been performed to assess the seeing. The results of this experiment can be seen in Appendix A. It must be noted that the FWHM characterization does *not* take into account the damping effect of the outer and inner scales of the turbulence. Thus, it was decided to implement the angle of arrival experiment for increased accuracy (Appendix A, Section 4.2).

In the set-up, both fans are operated at identical fixed velocities to achieve $D/r_0$ ratios compatible with the average working conditions at good astronomical sites, and necessary ducting is used to allow air exhaust. The ratio $D/r_0$ is critical for optical systems; it represents the main effect of optical turbulence on a beam of diameter $D$. The variance of the phase aberrations due to atmospheric turbulence is shown to be proportional to this ratio. This will be explained in the next section.

## 3.3 Angle of Arrival Experiment to Determine Fried Coherence Length in the Turbulence Simulator

The Angle of Arrival (AoA) is defined as the mean slope of the turbulent wavefront $W(x,y)$ into the pupil $P(x,y)$ of the telescope, or the exit pupil of the turbulator in the experiment:

$$\alpha_P = \frac{X_C}{F_L} = \frac{\iint P(x,y)\frac{\partial W}{\partial x}(x,y)dxdy}{\iint P(x,y)dxdy} \tag{3.1}$$

where $F_L$ is the focal length, and $X_C$ is the x-coordinate of the image centroid. The image centroid is tracked by spot-tracking software developed at the UVic AO Laboratory; it provides the time and centroid displacement on $x$- and $y$-axes. Equation 3.1 is given for the x-coordinate on the focal plane. The relation for the y-coordinate is the same as the x-coordinate and is obtained by derivation versus y instead.

In the general case of a limited flow, the AoA variance for the phase aberrations is given, for a turbulent layer of thickness $\delta h$, by [25]:

$$\sigma_{AoA}^2[x,y] = (2\pi)^{4/3} 0.033 C_N^2 \delta h \iint_{R^2} f_{X,Y}^2 (f^2 + L_0^{-2})^{-11/6} e^{-l_0^2 f^2} \left[ \frac{2J_1(\pi D f)}{\pi D f} \right]^2 df_X df_Y \quad (3.2)$$

Only in the infinite-scale regime ($L_0 = \infty$ *and* $l_0 = 0$), can this equation have an analytic solution:

$$\sigma_{AoA}^2[x,y] = 2.8375 C_N^2 \delta h D^{-1/3} = 0.1698(\lambda / D)^2 (D / r_0)^{5/3} \quad (3.3)$$

The main effect of optical turbulence on a beam of diameter $D$ is the creation of phase aberrations, for which the aberration variances can be shown to be proportional to the ratio of pupil diameter to the Fried coherence length [12], $(D/r_0)^{5/3}$. It can be seen that the AoA variance of these aberrations decreases when the pupil diameter is increased. In the limited regime, this is still the case, but with the departure from the $D^{-1/3}$ law at small and large values of $D$, due to the damping effect of $L_0$ and $l_0$. Masciadri [25] has suggested using this dependency as a way to measure the $L_0$ and $l_0$ in turbulent flows.

The characterization of the turbulence simulator using the AoA method is done in two steps:

- The heaters and the fans are set to a fixed temperature difference and wind velocity. The displacement of the instantaneous image centroid $(x_c, y_c)$ is tracked at

a sampling frequency of 522 frames/sec for 20 seconds. The results can be seen in Appendix A, Figure 4. The tracked displacements are later divided by the focal length $F_L$ to get the AoA.

- The empirical variance of the AoA is calculated by Equation 3.1 for each diameter, and the $C_N^2 \Delta h$, $L_0$ and $l_0$ values are assessed by the fit of the theoretical model to the empirical variances (the result is shown in Appendix A, Figure 6).

The flow apparent velocity modulus can be determined from the knee frequency of the AoA temporal power spectrum: It can be shown [13] that, at low and high temporal frequency, the AoA spectrum has a power-law dependency in, respectively, $f^{-2/3}$ and $f^{-11/3}$ (instead of $f^{-17/3}$ at high frequencies for Zernike polynomials [14]). The intersection of these two asymptotes defines the power-spectrum knee frequency:

$$f_c = 0.7\, v/D \tag{3.4}$$

where $V$ is the main layer velocity, $n$ the radial order of the polynomial, and $D$ is the diameter of the telescope. To reproduce the same dynamic behaviour in the turbulator, it is (in principle) sufficient to reproduce the $v/D$ ratio. This equation assumes a single layer, frozen turbulence [15] in the beam of the telescope. In this hypothesis, the turbulence is modelled as a set of parallel layers and the evolution in each layer is dominated by a horizontal displacement caused by wind. For the wind velocity $v(z)$ of a layer at height $z$, the displacement is $(v(z)\cdot\Delta t)$. Under the Taylor hypothesis [15], the required timescale to reconstruct and apply the wavefront correction can be predicted by the horizontal wind speeds.

In Figure 18, this knee frequency is measured on the graphs of the experimental AoA temporal power spectrum from which the apparent flow velocity $V$ can be extracted. This is done by extrapolation of the low- and high-frequency asymptotes in a log-log representation, carefully avoiding the outer-scale and inner-scale damping areas. The procedure was repeated for a range of different voltages applied to the fans, which allowed the calibration of the air velocity inside the turbulator.

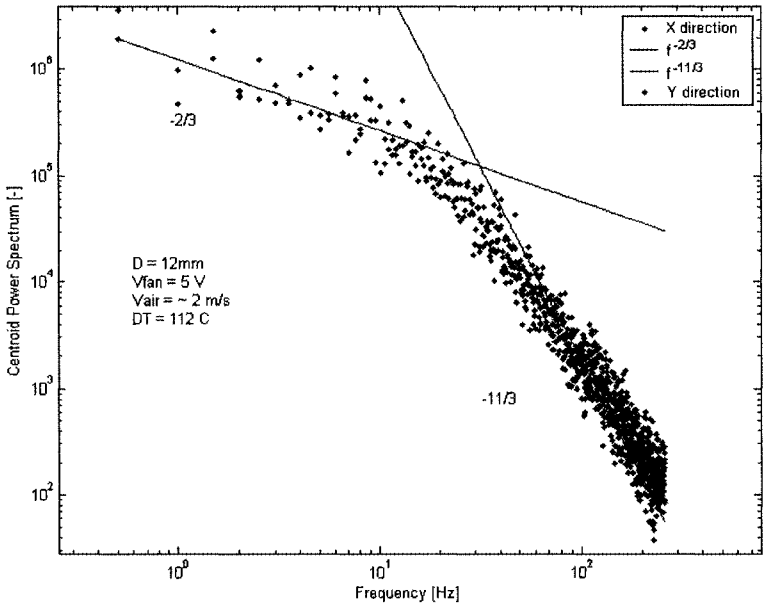


**Figure 18: Power spectrum of the centroid displacement (arbitrary units).**

The turbulence simulator is versatile for emulating $C_N^2$ and wind velocity by changing the fan speeds and $\Delta T$. The experiment has been implemented for temperature differences from 30 to 160 K; the results are presented in Table 1

**Table 1: Experimentally Measured $C_N^2$ and Associated $r_0$ Values.**

| ΔT (°C) | $C_N^2\Delta h$X ($10^{-10}m^{-2/3}$) | $r_0$X (mm) | $C_N^2\Delta h$Y ($10^{-10}m^{-2/3}$) | $r_0$Y (mm) | $C_N^2\Delta h$(mean) ($10^{-10}m^{-2/3}$) | $r_0$Y(mean) (mm) |
|---|---|---|---|---|---|---|
| 33 | 2.55 | 2.89 | 2.21 | 3.15 | 2.38 | 3.01 |
| 63 | 4.28 | 2.12 | 3.61 | 2.35 | 3.95 | 2.23 |
| 103 | 4.38 | 2.09 | 3.95 | 2.22 | 4.17 | 2.15 |
| 133 | 5.47 | 1.83 | 4.83 | 1.97 | 5.15 | 1.90 |
| 163 | 6.16 | 1.70 | 5.53 | 1.82 | 5.85 | 1.76 |

In the experimental evaluation, it is found that the turbulence simulator is able to create one well-characterized turbulence layer and it is assumed that by keeping the ΔT constant, the $C_N^2$ remains constant in this layer. This layer is later characterized by using slope detection and ranging (SLODAR) methodology. The details of the SLODAR method and experimental results can be seen in Section 3.5.

## 3.4 Outer and Inner Scale Damping Effects of Atmospheric Turbulence

The outer scale $L_0$ is the upper limit of the turbulent flow extension. This scale limit has the effect of damping the low-order optical aberrations. The damping effect is relative to the case of an infinite extension of the flow [16] because it is assumed in the Kolmogorov [5] model; therefore, the Kolmogorov model overestimates the damping effect of

turbulence. The Von Karman [17] (VK) empirical-phase power spectrum is generally used to take into account the effect of the $L_0$-damping effect in the low spatial frequencies of turbulence, and is given by:

$$\phi(f) = \frac{0.023}{r_0^{5/3}} \left( f^2 + \frac{1}{L_0^2} \right)^{-11/6} \tag{3.5}$$

where $f$ is the spatial frequency.

The inner scale $l_0$ has the same effect for the high-order aberrations, and the $l_0$-damping factor of the phase power spectrum can be approximated by:

$$\eta[l_0] = \exp(-l_0^2 f^2) \tag{3.6}$$

Another more sophisticated model for inner-scale damping is provided by the Hill-Andrew empirical damping factor [18], but is not discussed here.

Due to the strong decrease of the VK power spectrum at high frequencies, the $l_0$ damping effect is generally negligible for astronomical telescopes, where the telescope's aperture (D) is much larger than $l_0$. In Figure 18 of the experimental results for the turbulator, however, the effect of $l_0$ must be taken into account. Here, the $l_0$ damping is noticeable as $D$ (the entrance pupil in the bench Ø =42 mm) is close to $l_0$. Because $L_0$ and $l_0$ are related only to the dynamic properties of the turbulent flow, the outer and inner scales are not dependent on the temperature differences occurring on the turbulence, and the mean values of $L_0$ and $l_0$ among all temperature-difference measurements have been found to be $L_0$=133±60 mm and $l_0$=7.6±3.8 mm. The $L_0$ value is compatible with the dimensions of the turbulence simulator's mixing chamber (17 cm x 17 cm), and the $l_0$ value is compatible with measurements made by other authors (e.g., Masciadri and Vernin [19]).

## 3.5 Characterization of the $C_N^2$ Profile for the Turbulence Simulator

The principle of the SLODAR technique is the following [20]:

- Two stars a few arcseconds apart are observed with a Shack Hartmann wavefront sensor (SH WFS will be explained in the next chapter).
- The cross-correlation of the time series of the slopes from lenslet to lenslet can be interpreted as a measure of the $C_N^2$ profile within the altitude range where the two star beams overlap.

Practically, the cross-correlation has to be deconvolved with the single-star auto-correlation (taken from either of the two stars), and the $C_N^2$ is given by:

$$C_N^2 \sim F^{-1}\left\{\frac{F\left[C(\delta_i,\delta_j)\right]}{F[A(\delta_i,\delta_j)]}\right\}(\delta_i,0) \tag{3.7}$$

where $F$ is the Fourier transform operator $\delta_{i,j}$ are the lenslet cross-correlation shifts in the WFS focal plane, $C(\delta_i,\delta_j)$ is the cross-correlation between the stars' slopes (or centroid) time series $\delta_i,\delta_j$, and A is the auto-correlation for the same shift.

$C_N^2$ can be retrieved from the deconvolved cross-correlation matrix along a line corresponding to the guide star's separation. The result can be seen in Appendix A, Figure 11. In the experiment, the two emulated stars have been oriented along the x-axis of the WFS.

### 3.5.1 Experimental Set-up for the SLODAR Technique

The vertical resolution of the $C_N^2$ measurement in SLODAR [20] mode is given by:

$$\delta H = D/n_s/\theta \tag{3.8}$$

where $D$ is the optical-beam diameter, $ns$ is the number of Shack Hartmann lenslets across the beam diameter (in the experimental evaluation a 10 x 10 lenslet is used), and $\theta$ is the angular separation of the two stars as seen from the entrance pupil of the SLODAR set-up (45 degrees in our case). The maximum sensing altitude is given by:

$$H_{max} = D/\theta \tag{3.9}$$

The two stars are emulated using a pig-tailed laser diode unit (LD-2310 Solid State Laser Diode coupled to a single mode fiber). The fibers are separated by a known angle (1.7 arcsec as seen from the entrance pupil). For that purpose, a laser mount unit has been manufactured by Micro-Electro Discharge Machining in order to obtain a precise 140-μm separation between the two star images on the SH WFS focal plane. This corresponds to a separation of 2.48 pixels. The diverging light from the fibers was collimated by a Melles Griot lens with a 150-mm focal length, which produced a collimated beam of 25-mm diameter.

The SLODAR experiment has been implemented for temperature differences from 30 to 160 K, generating $r_0$ values from 3 to 1.7 mm as calculated from the AoA characterization (Table 1). The centroid position for each star is tracked using an algorithm that is able to read separately both regions on the CCD sub-lenslet images around each star centroid. Ten thousand samples are taken, with a frame rate of 522 Hz, short enough to freeze the centroid motion during the exposure. The figure obtained by centroid tracking for one of the measurements can be found in Appendix A, Figure 9,

where it can be seen that the displacement amplitude is practically the same for both axes and for both stars. From Figure 9, it can be concluded that the optical turbulence is isotropic, according to Kolmogorov's theory.

Figure 19 shows the relation of $C_N^2$ to temperature difference. The over-plotted curve is a model in $C_N^2 \sim \Delta T^2$, predicted by the theory [21] (Equation 2.8). The agreement is quite sound. The next step would be to calibrate these profiles in absolute intensity using the calibration curve shown above.

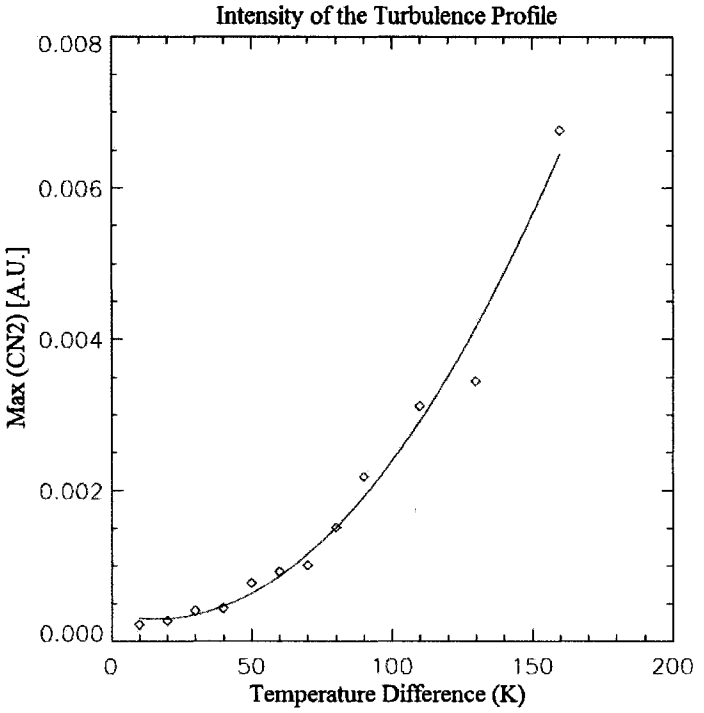


**Figure 19: Intensity of $C_N^2$ profile.**

In this experiment, the SLODAR procedure has been implemented and tested, but a $C_N^2$ characterization has not been accomplished due to the poor resolution of the test-bed. In the outcome of this experiment, a single layer at the apparent altitude has been

detected. For further details on the SLODAR experiment and the results, refer to Appendix A.

# 4. Adaptive Optics for Giant Segmented Mirror Telescopes

Modern ground-based telescopes use AO systems to detect and compensate, in real time, phase aberrations on the target's wavefront caused by turbulent atmosphere. This process takes place while the observations are in progress. In principle, very faint objects can be imaged during long exposures, provided there is a bright reference beacon nearby to allow the AO system to analyze the atmospheric effects. Furthermore, the real-time nature allows that spectroscopy becomes possible on very small angular scales, and it follows that fainter objects can be studied because less of the night-sky background needs to be included in the light being analyzed. In essence, AO systems enable Earth-based telescopes to see fainter objects further away.

## 4.1 Chapter Overview

This chapter provides an overview of classical and two deformable mirror adaptive optics systems. The aforementioned AO systems are used on the experimental evaluation of PSF reconstruction from the UVic AO test-bed.

The following sections in this chapter are:

- Section 4.2 defines a two DM AO system, used in the UVic AO Laboratory, called a Woofer/Tweeter AO system.

- Section 4.3 describes the UVic Woofer/Tweeter AO test-bed and the optical components used to measure and correct the aberrations.
- Section 4.4 describes the control system used in the numerical modelling and experimental evaluations from the UVic AO test-bed.

## 4.2 The Woofer/Tweeter AO System

Extremely Large Telescopes (ELTs) will have primary mirror diameters that are at least three times larger than the current major optical telescopes. The RMS amplitude of turbulence-induced wavefront distortions increases with the five-sixths power of the telescope aperture diameter $D$ [22], while at the same time, the number of DM degrees of freedom required to compensate for the distortions to any given level of correction is growing as $D^2$. This would require DMs with at least 2.5 times greater stroke and 9 times the number of actuators to achieve equivalent correction comparable to current AO systems. It appears that, due to the unavailability of a manufacturing technology for such a DM, it will not be possible to satisfy both these requirements for the ELTs with a single high-order and high-stroke DM. The power spectrum of atmospheric turbulence follows a decaying ($f^{-11/3}$) power law [23]. Therefore, most of the turbulence energy is concentrated at low spatial frequencies, and requires large stroke to correct the first modes of atmospheric turbulence. In contrast, at high spatial frequencies, the stroke requirement for the AO correction drops substantially. A solution to this problem is the use of dual DMs, the so-called W/T configuration. In W/T architecture, the Woofer (WR) is a low-order-high-stroke DM used to compensate for the low-frequency effects introduced by atmospheric turbulence. The Tweeter (TR) is a high-order-low-stroke DM used to

compensate for the high-frequency effects. Having dual DMs allows the W/T AO system to have a high degree of correction of large-amplitude wavefront distortion. Therefore, an improved PSF reconstruction methodology has been developed for W/T AO architecture.

Next-generation AO systems are planned for the TMT. TMT fulfils the goal of a concept called the Giant Segmented Mirror Telescope (GSMT), which was identified as the highest-priority new ground-based facility for the first decade of the 21$^{st}$ century [24, 25]. NFIRAOS will be the main facility adaptive optics system for TMT and will carry a dual DM AO system. The research concept of having two DMs will allow the W/T AO system to have a high degree of correction of large-amplitude wavefront distortion.

## 4.3 The UVic Woofer/Tweeter Test-Bed

The principle of operation of the UVic W/T AO system is illustrated in Figure 20. A planar wavefront, generated by a collimated point light source, goes through the hot-air atmospheric turbulence generator [26] (Appendix A) and becomes aberrated. The degree of distortion of the wavefront is detected by the SH WFS. The purpose of the W/T AO system is to make this distorted wavefront as flat as possible. The TT mirror is a flat mirror that adjusts the angle-of-arrival variations (tip/tilt variations) in the light of the target object due to atmospheric turbulence by counteracting the apparent motion of the star. Both DMs use a grid of actuators to deform their physical shape to a shape opposing the distorted wavefront. In the wavefront-compensation process, the commands of both WR and TR and the TT mirror are determined by the AO controller (in closed loop, indicated by long dashed lines), which uses the SH WFS measurements. During this

closed-loop operation, the WFS measures only the residual wavefront error reflected onto the DMs and the TT mirror (i.e., the uncorrected phase distortions of the wavefront). This process takes place in real time to compensate for the constantly changing optical effects of atmospheric turbulence.

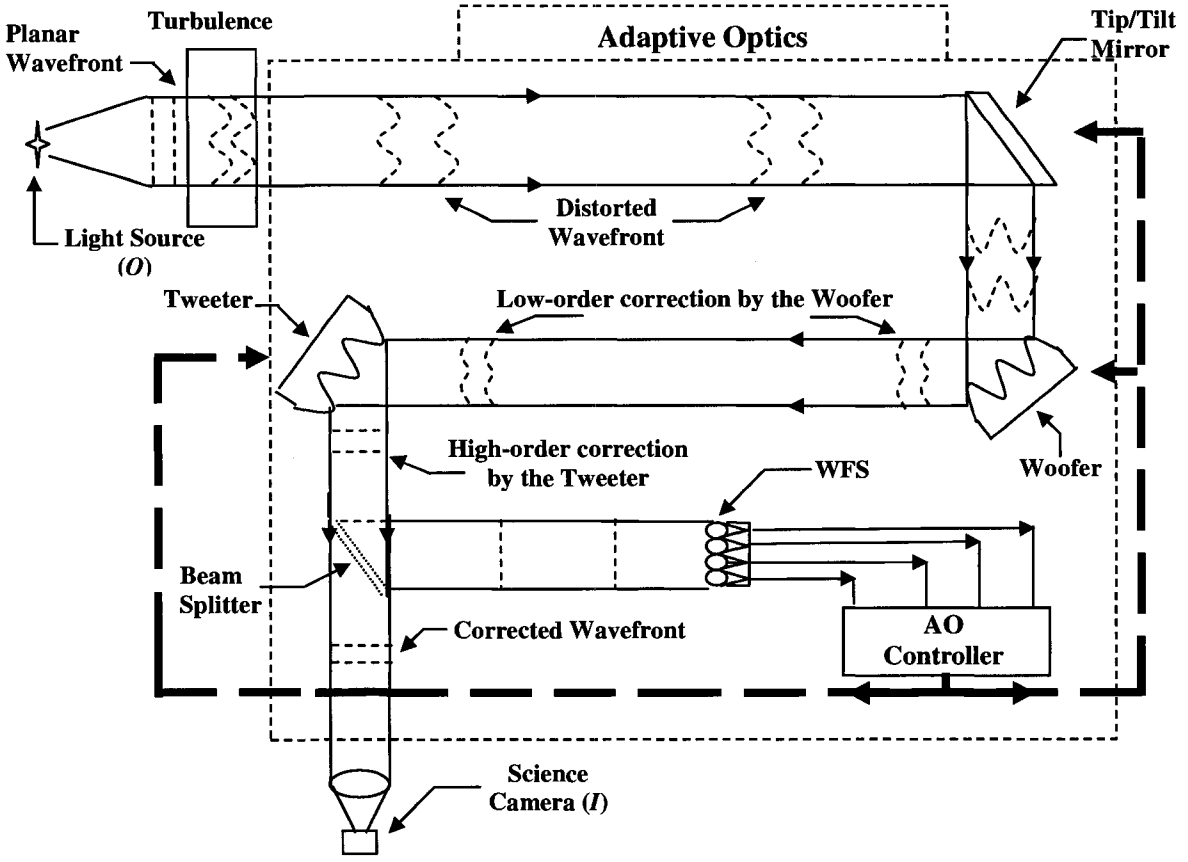


**Figure 20: Working scheme of the W/T AO bench (dashed area represent the AO system).**

The major components of the W/T test-bed will be described in the following sub-sections. These components are used in the experimental evaluation of the improved PSF reconstruction methodology (Appendix C), and in the numerical evaluation of off-axis PSF reconstruction (Appendix D).

### 4.3.1 Tip/Tilt Mirror

Tip/tilt mirror (TT) is a flat mirror that adjusts the position offsets of the incoming distorted wavefront by counteracting the apparent motion of the star. Atmospheric tip and tilt is responsible for almost 87% of the Kolmogorov phase variance [12]. These two modes are compensated for by a separate control loop and by the TT mirror to achieve the highest possible accuracy. Modes can be referred to as (a) the shape of the phase in the incoming wavefront, or (b) the shape of the wavefront corrector corresponding to this phase. The compensation of tip and tilt modes also assists in reducing the required stroke of the higher-order wavefront correctors, namely the Woofer and the Tweeter. This is also called a first-order correction involving the removal of the random displacements of the image, also referred to as tip-tilt correction. Tyler demonstrated that the bandwidth required for tip-tilt correction is about nine times lower than that required for complete atmospheric compensation [13]. As described earlier in Equation 2.14, the main effect of optical turbulence on a beam of diameter $D$ is the creation of phase aberrations, for which the aberration variances can be shown to be proportional to the ratio of pupil diameter to the Fried coherence length [12], $(D/r_0)^{5/3}$:

$$\sigma_{1\ modes\ removed}^2 = 1.0299\left(\frac{D}{r_0}\right)^{5/3} \tag{4.1}$$

The wavefront variance terms for the *tip* mode can be expressed as:

$$\sigma_{2\ modes\ (tip)\ removed}^2 = 0.582\left(\frac{D}{r_0}\right)^{5/3} \tag{4.2}$$

The wavefront variance terms for the *tilt* mode can be expressed as:

$$\sigma_{3\ modes\ removed}^2 = 0.134\left(\frac{D}{r_0}\right)^{5/3} \tag{4.3}$$

The TT mirror axes of rotation are defined in Figure 21(a). The TT mirror adjusts the position offsets of the incoming distorted wavefront by counteracting the apparent motion of the star in two axes (X and Y). The TT mirror uses multilayer piezo-actuators: piezoelectric materials change dimension when an electric field is applied; they are shown in Figure 21(b). A multilayer piezo-actuator is a stack of thin films of zirconium titanate electrically connected in parallel. The thinner the film, the lower the voltage required for the maximum expansion of the multilayer stack.

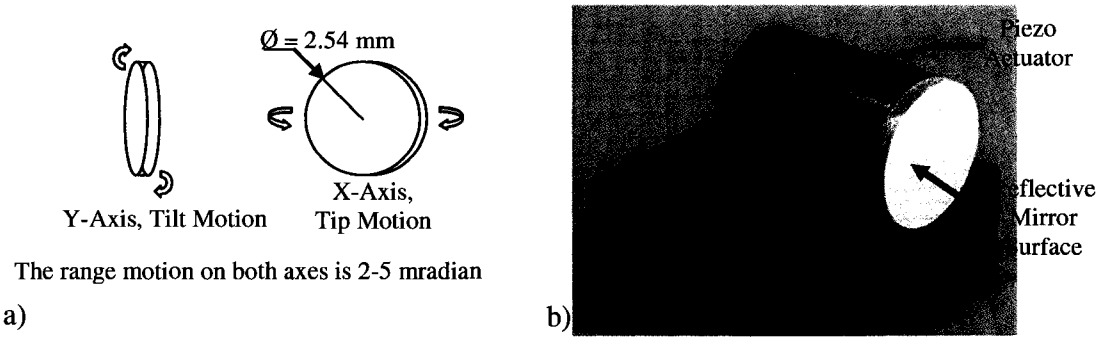


**Figure 21: (a) Configuration of the TT mirror; (b) multilayer piezo-actuator, the thin film layers of zirconium titanate are separated by conducting layers.**

The key tip/tilt mirror parameters are:

- Mirror diameter = 2.54 mm
- Scanning frequency = 1 kHz
- Range of motion = 2-5 milli-radian
- Resolution = 4 nano-radian

### 4.3.2 The Woofer Deformable Mirror

The low-order-high-stroke DM or Woofer is manufactured by LAOG (Laboratoire d'Astrophysique de l'Observatoire de Grenoble). Figure 22(a) illustrates the construction of the magnetic DM; it is a disk-shaped mirror. The Woofer is made of a continuous membrane that is deformed by a set of miniature voice-coil actuators that can be seen in (b). The flexible membrane is coated on its optical side with a reflective layer and on the other side with a magnetic layer. The reflective layer is a 2-5 μm thick polyimide film set onto a rigid ring and coated with an optical reflective layer. The magnetic element is an array of permanent micro-magnets glued onto the membrane, seen in Figure 22(c). The magnetic layer is actuated by the local magnetic fields generated by an array of planar micro-coils (voice coils) deposited on a Si substrate opposite the membrane. Voice-coil actuators are direct-drive, limited-motion devices that use a magnetic field and coil winding (conductor) to produce a force (F) that is proportional to the current applied to the coil. This process is governed by the Lorentz force principle. According to this law, if a current carrying conductor is placed in a magnetic field, the force $F$ will act upon it. The key parameters of the magnitude of this force will be the current ($i$), the magnetic flux destiny ($B$), a constant $k$, the total number of conductors ($N$), and the conductor length ($L$). This is shown in Figure 22(d).

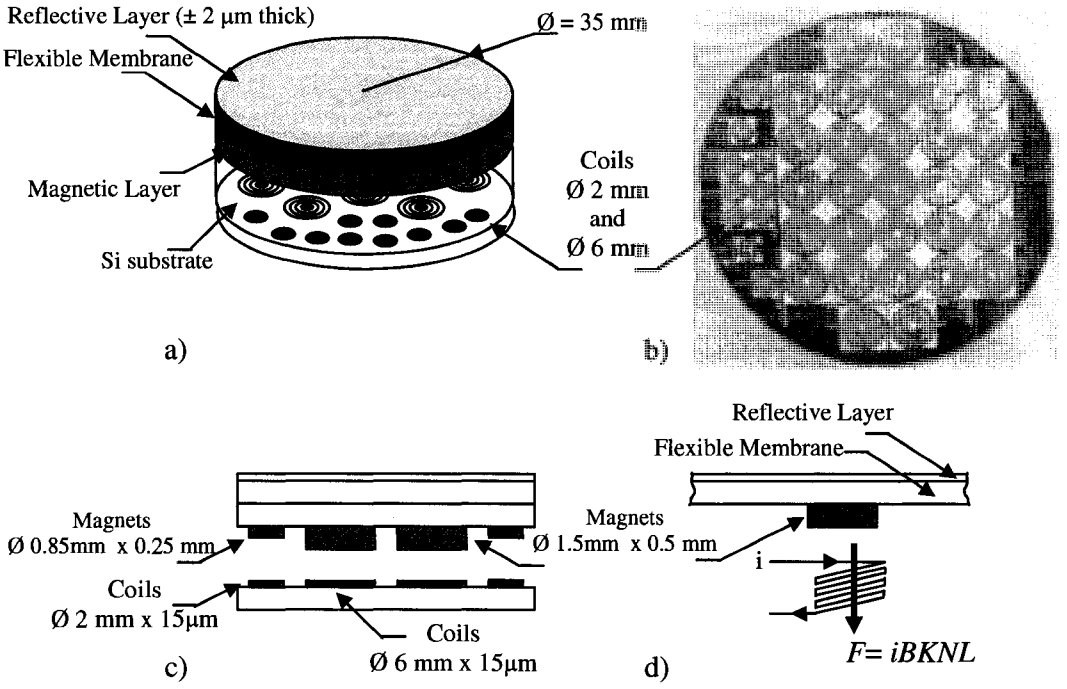


**Figure 22: Diagram showing the construction and principle of operation of the magnetic DM: (a) the construction of the magnetic DM; (b) illustration of voice coils actuators; (c) side view of the magnetic DM; (d) inductive force F acting on the magnet due to the coil current *I* under the Lorentz force principle.**

The Woofer has a 35mm diameter mirror that is used to compensate for the low-order aberrations introduced by the turbulence generator. Figure 23(a) illustrates the configuration of the Woofer. The magnetic DM contains 64 (8 x 8 scheme) actuators within the flexible membrane (Ø = 35 mm). It must be noted that the Woofer is conjugated to the entrance pupil of the telescope. The role of the entrance pupil is to emulate the telescope's aperture size. Therefore, the physical diameter of the light is limited by the telescope's aperture. In the experimental evaluation, the size of the beam is adjustable, by an iris, in order to emulate the $D/r_0$ ratios in the AO test-bed. But the pupil

size is chosen to be 20 mm for this particular set-up because there are 8 actuators across, with an actuator pitch of 2.5 mm. Within this pupil, the Woofer has 52 actuators.

It was decided to correct the following 50 modes after correcting for the tip/tilt. The wavefront variance terms for these Woofer modes can be expressed as:

$$\sigma^2_{50\ woofer\ modes\ removed} = 0.2944 N_{Zernike}^{-\sqrt{3}/2} \left(\frac{D}{r_0}\right)^{5/3} \tag{4.4}$$

where $N$ is the number of Woofer modes.

Influence functions can be defined as a map of the physical deformations in the DM surface after applying voltage to a given actuator. This is illustrated for a single actuator in Figure 23(b). The flexible membrane of the Woofer is clamped from both ends to limit surface deformation in the corners; this can be seen in (c). In addition, the mirror surface has 5 nm rms flatness. The Woofer provides 25μm of maximum stroke and because there is no contact between the membrane and the coil array, large surface deformations are possible. Figure 23(d) illustrates the Woofer surface deformation in a downward direction.

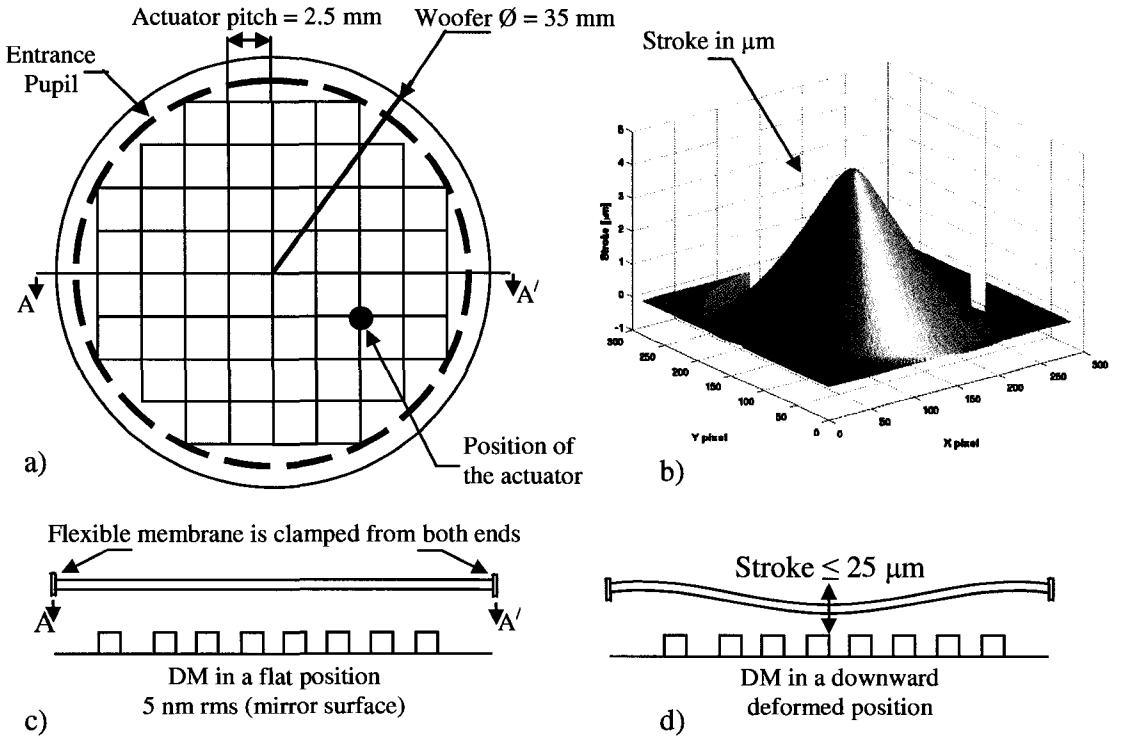


**Figure 23: Design and layout of actuators in the Woofer DM: (a) actuators in the flexible membrane; (b) illustration of an influence function on a single actuator, here the Z-axis is defined in μm; (c) flexible membrane with no deflection, mirror surface is flat to within 5 nm rms; (d) flexible membrane in a downward position.**

### 4.3.3 The Tweeter Deformable Mirror

The Tweeter mirror is a Micro Electro Mechanical Systems (MEMS) mirror manufactured by Boston Micromachines. It is a high-order-low-stroke DM that is used to compensate for the high-order aberrations introduced by the turbulence generators. Figure 24 illustrates the working principle of the continuous deformable mirror. The actuator membrane serves as the upper electrode of a parallel plate capacitor. The stationary layer on the bottom actuator electrode serves as the second electrode of the capacitor. When a voltage difference is applied between the lower electrode and the grounded upper electrode, the actuator membrane deflects downwards/upwards. The attachment post and mirror surface are correspondingly deflected. In order to provide the high surface quality of the DM, a chemo-mechanical polishing process is followed up with a gold coating process. This has improved the reflectivity without introducing a significant amount of stress in the mirror membrane.

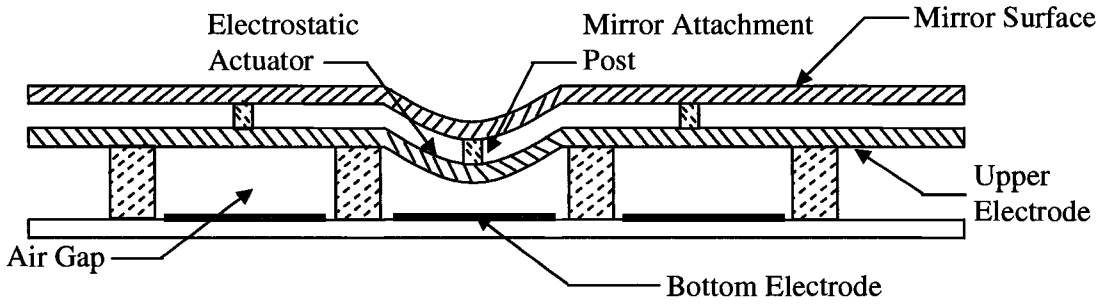


**Figure 24: Deformation principle of the continuous mirror.**

The Tweeter is a square-shaped mirror (3.3 x 3.3 mm). Figure 25(a) illustrates the configuration of the continuous DM, which contains 144 (12 x 12 scheme) actuators. The actuators on the border of the DM are not used for correction. This reduces the number of

actuators to 10 x 10. It must be noted that the Tweeter is conjugated to the entrance pupil of the telescope. The role of the entrance pupil is to emulate the telescope's aperture size. Therefore, the physical diameter of the light is limited by the telescope's aperture. In the experimental evaluation, the size of the beam is adjustable (by an iris) to emulate the $D/r_0$ ratios in the AO test-bed. However, the pupil size was chosen as 2.7 mm for this particular set-up as there are 9 actuators across, with an actuator pitch of 300 μm. Within this pupil, the Woofer has 80 actuators.

It was decided to correct the following 80 modes after correcting for the tip/tilt and for the Woofer modes. The wavefront variance terms for these Tweeter modes can then be expressed as:

$$\sigma^2_{80\ tweeter\ modes\ removed} = 0.2944 N_{Zernike}^{-\sqrt{3}/2} \left(\frac{D}{r_0}\right)^{5/3} \tag{4.5}$$

where $N$ is the number of Woofer modes.

Influence functions can be defined as a map of the physical deformations in the DM surface after applying voltage to a given actuator. Given the fact that this is a continuous mirror, one poked actuator influences its neighbour actuators as well; this is illustrated for a single actuator [26] in Figure 25(b). The reflective surface of the mirror is flat to within 1 nm rms; this can be seen in (c). Figure 25(d) illustrates the Tweeter surface deformation in a downward direction, where the mirror provides 1.5 μm of maximum stroke.

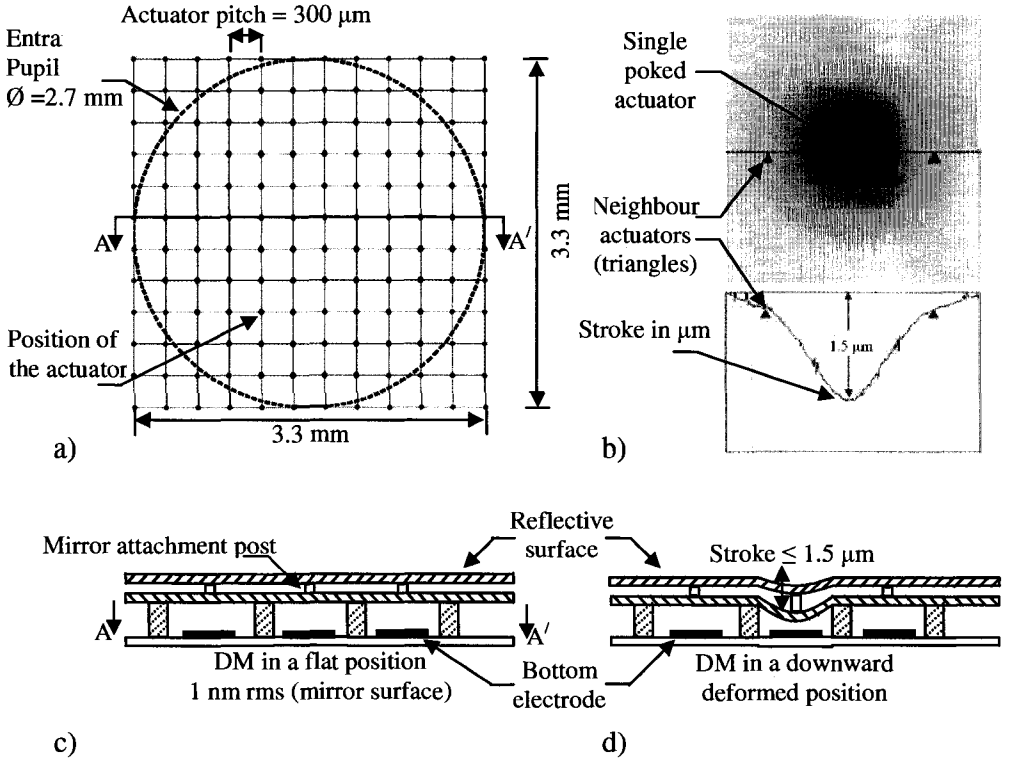


**Figure 25: Design and layout of actuators in the tweeter DM: (a) the configuration of actuators inside the pupil; (b) illustration of an influence function on a single actuator, here the single actuator affects its neighbours given that this is a continuous mirror; (c) reflective surface with no deflection, mirror surface is flat to 1 nm rms; (d) the mirror in a downward position.**

### 4.3.4 Shack Hartmann Wavefront Sensor and the Camera

The Shack-Hartmann wavefront sensor placed on the experimental test-bed (SH WFS) is made of 132 x 132 square lenslets with a pitch of 188 μm and 8 mm focal length. The registration affects the control algorithm and the stability of the control system. Therefore, on the experimental bench and in numerical evaluations, a subset of 9 x 9 lenslets is used to match the 10 x 10 Tweeter actuators according to Fried geometry [27]; this can be seen in Figure 26. According to Fried geometry, the number of lenslets across the WFS aperture needs to be at least half as many as there are actuators projected across the aperture in order to avoid any confusion in the control system for the right number of degrees of freedom as the measurements. Once the lenslet array is set, the TR mirror actuators are registered to the vertices of these lenslets.

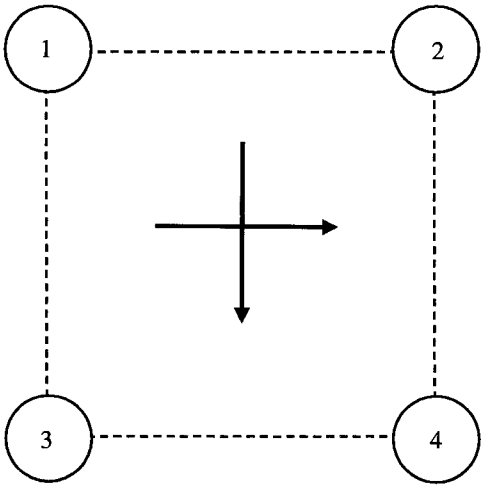


**Figure 26: Fried geometry; the numbered small circles represent actuator positions and the dotted large square represents one of the square sub-apertures with the orthogonal slope measurements represented by the arrows.**

Figure 27 illustrates the design and layout of SH WFS used in the experimental bench and (a) shows the 9 x 9 portion of the SH WFS used in the bench where the position of the lenslets can be seen. The lenslet is formed from a sheet of micro-lenses, also termed a *lenslet array*, and is placed in a plane conjugate to the pupil. Each lenslet is a sub-aperture. The sub-apertures intercept the light from a section of the full pupil image, and form an image of the source at the lenslet focal plane. Here, the used portion of the lenslet array is 1.7 x 1.7 mm. Within this portion, the WFS is conjugated to the pupil, as well; only the section corresponding to the entrance pupil will be illuminated. In Figure 27(b), the optical windows are polished to a flatness of $\lambda/4$, a broadband anti-reflection coating is provided on the flat, glass side of each epoxy substrate. A four-cell detector, or quad-cell, is placed at the image of each lenslet, as in (c), representing a reference plane wave; it is further zoomed in at (d). The intensity of the light is equal in each quadrant. Alternatively, in case of a disturbed wavefront, the aberrations on the incoming wavefront across a lenslet sub-aperture will cause the focused spot to displace an amount proportional to the local wavefront slope. This is shown in (e); from the angle of arrival calculation (Section 2.6.2), the centroid movement can be calculated. Further zoomed in: in Figure 27(f), the centroid tracking in x- and y-coordinates can be determined from the intensities in those quadrants, where the signal from one quadrant ($i_4$) is increased, while that from the other three quadrants is reduced.

In the numerical and experimental evaluations performed in the UVic AO Laboratory, centroid estimation is accomplished using a centre-of-gravity calculation [28]:

$$cent_x = \frac{\sum_{i,j} x_{i,j} I_{i,j}}{\sum_{i,i} I_{i,i}} \qquad \textit{and} \qquad cent_y = \frac{\sum_{i,j} y_{i,j} I_{i,j}}{\sum_{i,i} I_{i,i}} \tag{4.6}$$

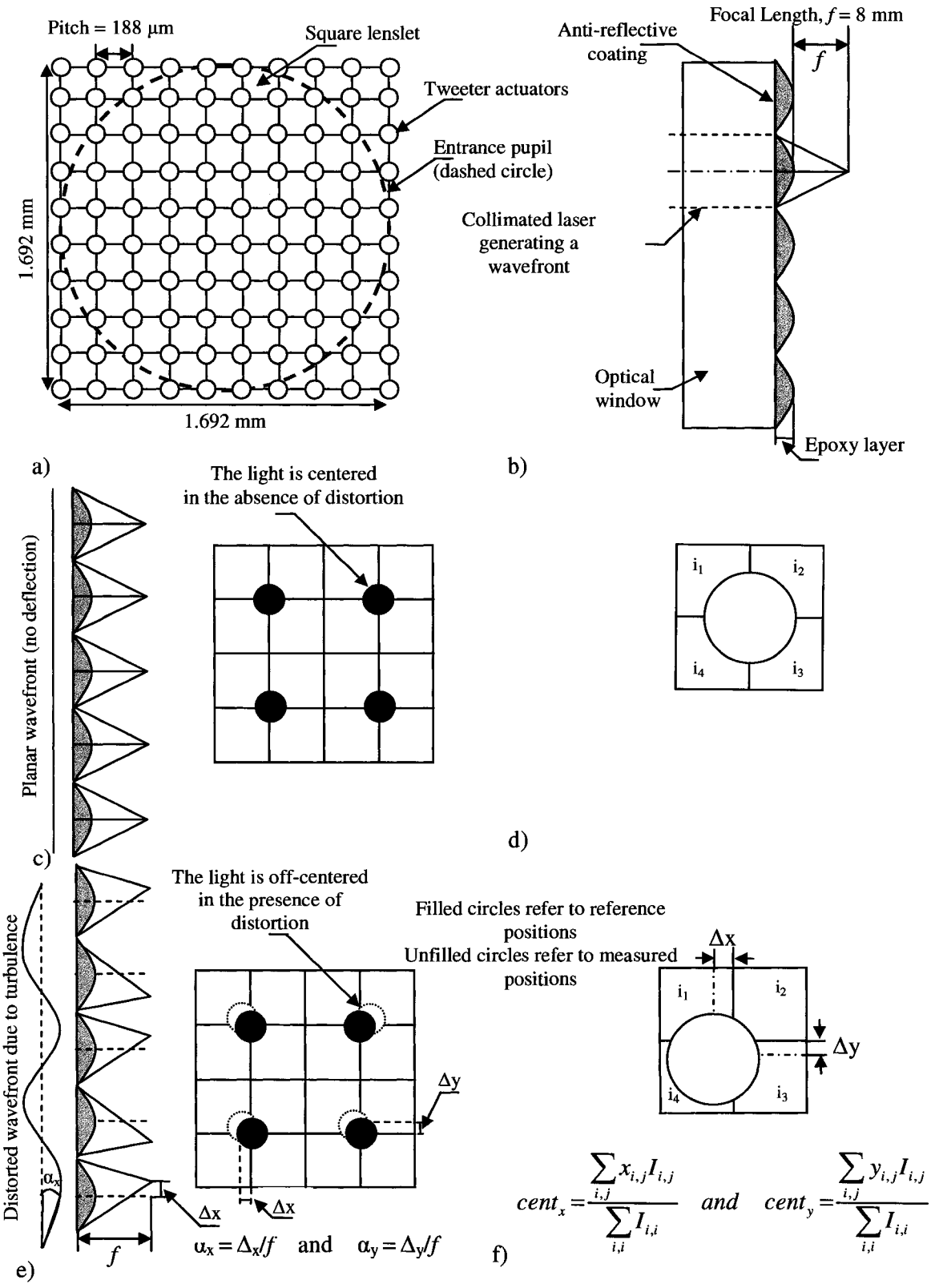


**Figure 27: Working principle of a Shack Hartmann wavefront sensor.**

Coupled with the high quantum efficiency and low-noise CCD cameras, SH WFS has become desirable for use in AO applications as the detector in the lenslet focal plane.

A detailed view of the final design, where the lenslet array is integrated with the CCD, is seen in Figure 28. The lenslet array rests on an extension at the base of the lenslet retention barrel. The lenslet barrel can be rotated to allow adjustment of the orientation. The lenslet array is placed at its focus from the CCD. The lenslet barrel slides inside the translation barrel. The translation barrel is attached to the camera housing by threads. This threading allows up to ±2.5 mm of travel about the mid-point to fine-tune the lenslet focus on the CCD. The lenslet retention barrel remains levelled against the translation barrel due to a pair of tensioning springs attached between the hooks at the front of the retention barrel and the Z-axis alignment. The Z-axis aligner bolts directly to the camera housing and tightly fits the translation barrel, providing the rigidity required to maintain the lenslet to CCD alignment.

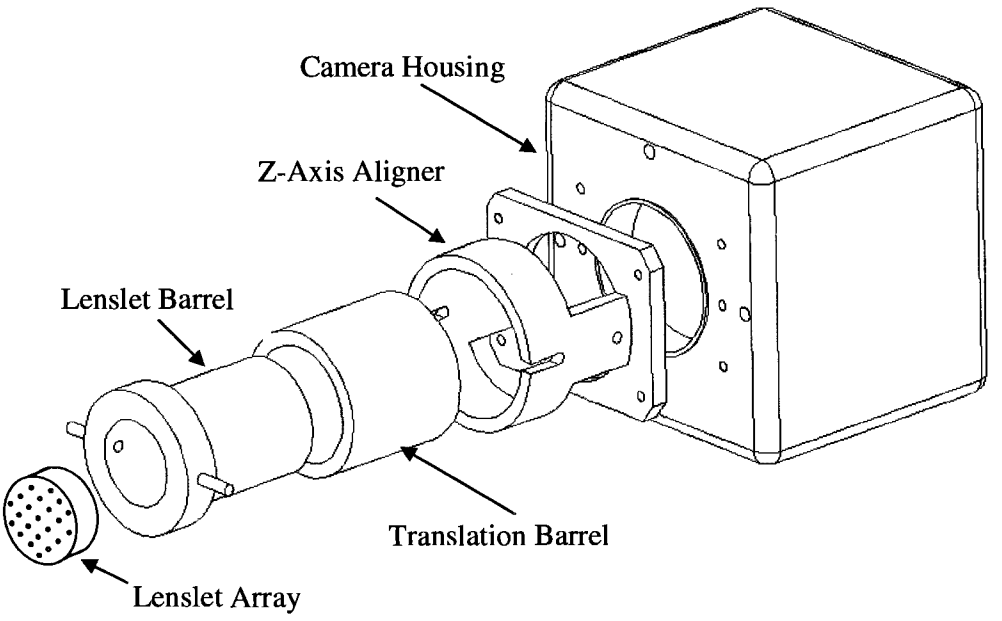


**Figure 28: Detailed view of Shack Hartmann wavefront sensor and its integration with the CCD.**

In the UVic AO test-bed, the selected camera for this application was the Dalsa CA-D1 digital camera. It has a frame rate of 736 fps, and is quite well suited for the bench because it operates at frame rates high enough to adequately sample the temporal variations of turbulence. The binning mode can be defined as reading the neighbouring pixel(s) and combining them directly from the CCD of the camera. The 128 x 128-pixel resolution is adequate for calculating centroids for 10 x 10 sub-apertures, where the pixel size is 16 μm.

The dynamic range and noise levels of the camera are not sufficient for low-intensity light work, but are acceptable in a laboratory environment.

## 4.4 Control System

The controller's role is to interpret the WFS data and to determine what adjustments are necessary to the physical shape of the two DMs and to the angle adjustments of the TT mirror in order to compensate for the present aberrations in the light path. The controller is used in both numerical and experimental evaluations (Appendix B, C, and D).

As described earlier, a mode is a DM surface shape. A modal basis is an orthogonal set of modes that can restrict the DM correction to a spatial frequency domain. The methods used to derive each DM modal basis are based on a model of the zonal influence function of each DM [29]. These DM modal bases are constrained to prevent specific modes from being produced.

The control scheme is illustrated in Figure 29. In the Woofer-Tweeter AO system, the WR is capable of correcting all the low-order modes (modes that require high stroke) including the tip/tilt. The TR can also reproduce all the shapes from tip/tilt to high-order aberrations. However, the limited stroke of the Tweeter does not allow it to compensate for the full amplitude of the tip/tilt or for the low-order modes. In the simulation and in experimental evaluation, DM commands among those different devices are split. Because neither the Woofer nor the Tweeter will compensate for the tip/tilt, this mode is removed from the influence function of the Woofer and from the influence function of the Tweeter along with the piston mode in which the WFS is insensitive. Later, to prevent TR actuator saturation, the WR influence functions are removed from the TR modes because the TR is capable of very little stroke with respect to the Woofer. Lastly, TR modes are split for that particular device.

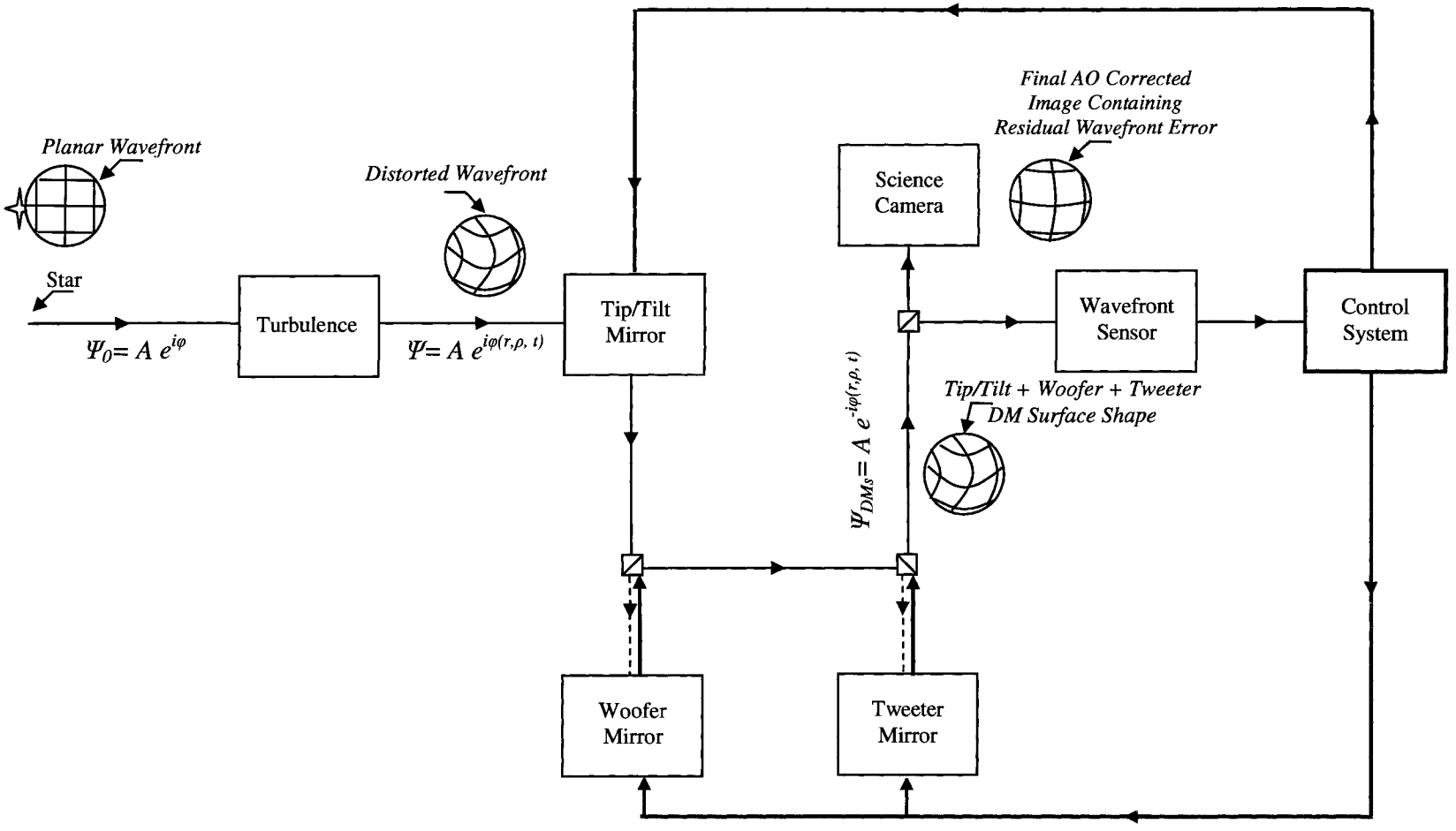


**Figure 29: Illustration of the control system (red lines). To compensate for the distortions in the incoming wavefront, the control system sends separate commands to the TT mirror, WR mirror and the TR mirror.**

The interaction matrix is a matrix of sensor measurements that correspond to DM actuation. A zonal interaction matrix has rows that represent WFS measurement and columns that represent an individual DM actuator. The zonal interaction matrices are measured by applying an identical positive and negative stroke to the actuators. For each actuator, half the normalized difference between the centroids corresponding to each successive push and pull gives the interaction matrix column of this actuator.

The interaction matrix $D$ is the link between the actuator command vector $c$ and the SH WFS measurement vector **s** is:

$$\vec{s} = D\vec{c} \tag{4.7}$$

Figure 30 shows the three zonal interaction matrices of the tip/tilt $D_{TT}$, the Woofer $D_W$, and the Tweeter $D_T$. Here, those three matrices have been concatenated into the single zonal matrix $D_z$. In this figure, the first two columns correspond to the tip/tilt interaction matrix. The following 52 columns represent the interaction matrix for the woofer actuators and then the 80 columns for the Tweeter actuators. The top half corresponds to the $x$-component of the WFS centroids, and the bottom half corresponds to the $y$-component of the centroids. The colour bar represents the centroid motion amplitude in CCD pixel values. It clearly appears that the WR-influence functions are much broader than the TR-influence functions. By comparison, the TR actuators mainly affect the centroids of the four lenslets that surround them, the adjacent lenslets.

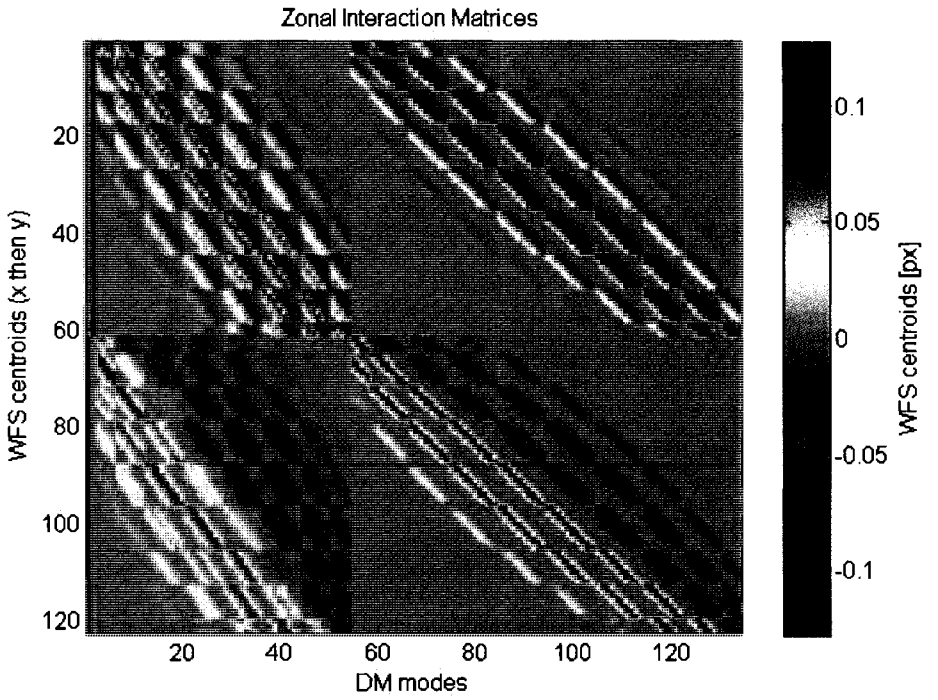


**Figure 30: Measured zonal interaction matrices concatenated into a single zonal matrix Dz = [DT DW DT], from left to right the tip/tilt, the zonal Woofer and the zonal Tweeter.**

In the control of the UVic AO system, the SH WFS measurements, vector *s*, are used to correct for the phase aberrations. The command matrix *M* relates the DM actuator commands (vector *c*) to the SH-WFS measurements *s* through the equation:

$$\vec{c} = (D^T D)^{-1} D^T \vec{s} = D^{\dagger} \vec{s} \tag{4.8}$$

where $D^{\dagger}$ is usually called the generalized inverse, or pseudo-inverse of *D*. $(D^T D)^{-1}$is generally an ill-conditioned matrix; therefore, $D^{\dagger}$ is preferably deduced from the singular values decomposition of *D* by:

$$D = U \Sigma V^T \tag{4.9}$$

Here *U* and *V* are orthogonal, and *V* is an orthonormal basis of the DM actuator space, $\Sigma$ is a diagonal matrix with the singular values of $D^T D$, and *U* is the basis *V* translated

into the WFS space. The singular value decomposition (SVD) generates an orthogonal set of operating modes ($V$ matrix) from the interaction matrix such that the corresponding WFS measurements ($U$ matrix) are also orthogonal. The singular values represent the sensitivity of the system to Eigen modes. The pseudoinverse can then be obtained by:

$$D^{\dagger}=(D^{T}D)^{-1}D^{T}=V\Sigma^{\dagger}U^{T} \tag{4.10}$$

where $\Sigma^{\dagger}$ is the pseudoinverse of $\Sigma$, and $D^{\dagger}$ is the reconstructor. Small singular values of the interaction matrix relate to large singular values of the reconstructor, which leads to noise amplification. Therefore, a threshold is set on the small singular values of the $D^{\dagger}$, forcing the small values to zero, while computing the reconstructor in order to avoid noise amplification. The command matrix can then be obtained. In other words, the reconstructor computes the conjugate wavefront with data from the WFS, and applies the appropriate signals to the controller, which in turn applies that conjugate pattern to the deformable mirrors.

# 5. Point-Spread Function for Giant Segmented Mirror Telescopes

In AO applications, PSF reconstruction is used in calibrating image analysis techniques for astrometry, and in the deconvolution of images to enhance their contrast. The partial correction provided by the AO system is due to the finite sampling of the wavefront sensor, the DM (limited number of freedoms on the DM, i.e., the number of actuators) and the finite bandwidth of the control system. Furthermore, the correction provided by an AO system degrades across the field of view, depending on the angular separation between the guide star and the target object (anisoplanatism). The partial correction provided by the AO correction is mainly due to the high spatial frequencies introduced by the atmospheric turbulence (AO system components are not fast enough), and this translates into a halo artifact on the PSF obtained by the system's science camera. Consequently, the dimmer details of the images may not be detectable. One possible way to counteract this halo effect is through PSF reconstruction, and deconvolving this reconstructed PSF through the image gathered by the science camera of the system. In order to achieve accurate results, the analysis of the corrected images must account for the PSF temporal variation. Unfortunately, calibrating the PSF with pre- and/or post-observation of bright stars across the field does not give reliable results due to the temporal variability of the seeing. The most promising and reliable technique to achieve PSF reconstruction is to use the wavefront sensor data measured synchronously with the observation (AO exposure).

In the case of on-axis observations, only one PSF reconstruction tool has been implemented for operational use on an astronomical telescope: Veran's [30, 31] code for the

Canada-France-Hawaii Telescope (CFHT) Adaptive Optics Bonnette (also called PUEO). Although the original method was developed using a curvature wavefront sensor, the algorithm was later adapted and applied to a Shack Hartmann WFS (SH WFS) [32, 33, 34,35]. In the Woofer/Tweeter (W/T) AO bench, the methodology is also applied to a SH WFS [36].

The goal of this research is to develop a PSF reconstruction method for a dual DM AO system, where the target object is at an angular separation from the guide star. In order to achieve this objective, the following steps were undertaken:

1) An end-to-end numerical model of a single DM AO system with the target object on-axis has been performed. The model is entirely coded with Matlab, and is composed of the models of each system sub-components (e.g., a point source light, a wavefront sensor, a deformable mirror, a controller, and a science camera). The model output is the system performance in the form of the science-camera image. The single DM PSF reconstruction method is then implemented on the Matlab model and the results are compared to the PSF obtained by the science camera of the model. Based on the accurate estimation of the PSF from the numerical model, the method is experimentally evaluated. The comparison between the experimentally reconstructed PSF and the numerical model ensured the successful implementation of the methodology for an on-axis classical AO system; evidence of this can be seen in the results presented in Appendix B.

2) Building on the success of the on-axis classical AO system, the complexity of the model and of the experimental set-up has been increased to include dual DM AO architecture. The proposed PSF reconstruction methodology has been implemented on the Woofer/Tweeter AO system, but the method can also be applied to AO systems using

N number of DMs. The reconstructed PSF comparisons between the numerical and experimental evaluation resulted in close agreement, which ensured the successful implementation of the proposed methodology. Evidence of this is can be seen in the results presented in Appendix C.

3) The complexity of both the analysis and the model was extended from a single light source to a multi-light source scheme to accommodate for the anisoplanatic errors that degrade the performance of AO systems at greater angular distances from the guide star. An improved off-axis PSF reconstruction methodology has been developed and numerically evaluated for the dual DM (Woofer/Tweeter) off-axis AO architecture. The comparisons between the reconstructed PSFs from the numerical model and the PSFs obtained by the science camera of the numerical model resulted in close agreement. This ensured that the effect of anisoplanatism in AO-compensated image quality can be improved by the successful implementation of the proposed methodology. Evidence of this is can be seen in the results presented in Appendix D.

## 5.1 Chapter Overview

This chapter was written to give an overview and describe the PSF reconstruction work performed at the UVic AO laboratory as part of the Ph.D. thesis project.

The following chapter sections present key definitions, methods and results of PSF reconstruction in general, and PSF reconstruction work at the UVic AO Laboratory:

- Section 5.2 defines the importance of PSF reconstruction in AO systems employed in giant segmented mirror telescopes. The effect of atmospheric

turbulence on on/off axis PSFs obtained by imaging systems of telescopes will be discussed.

- In Sections 5.3 to 5.5, Appendix B, the paper, *"Point-spread function reconstruction from Woofer/Tweeter adaptive optics bench,"* written as part of the Ph.D. thesis project will be discussed. The article details the adapted methodology, and numerical-based experimental evaluation of PSF reconstruction from a classical AO system scheme.
- In Sections 5.6 to 5.8, Appendix C, the paper, *"Derivation and experimental evaluation of a point-spread function reconstruction from a dual deformable mirror adaptive optics bench,"* written as part of the Ph.D. thesis project will be discussed. The article describes the proposed PSF reconstruction methodology for a dual DM AO scheme, and the implementation of this methodology both by numerical modelling, and experimental evaluation.
- In Sections 5.9 to 5.10, Appendix D, the paper, *"Derivation and numerical evaluation of an off-axis point-spread function reconstruction from Woofer/Tweeter adaptive optics bench,"* written as part of the Ph.D. thesis project will be discussed. The article describes the improved off-axis PSF reconstruction methodology for a dual DM AO scheme, and the numerical evaluation.

## 5.2 The Importance of PSF Reconstruction in AO

In seeing-limited telescopes, long-exposure imaging properties of the optical system are relatively the same over the whole field of view. Therefore, telescopes can be called *isoplanatic* because only static aberrations occur in the telescope optics. In a seeing-limited telescope, the optical effects of turbulence cause image-quality limitations. In Figure 31, the optical effect of atmospheric turbulence on a long-exposure PSF, obtained by the science camera, is illustrated.

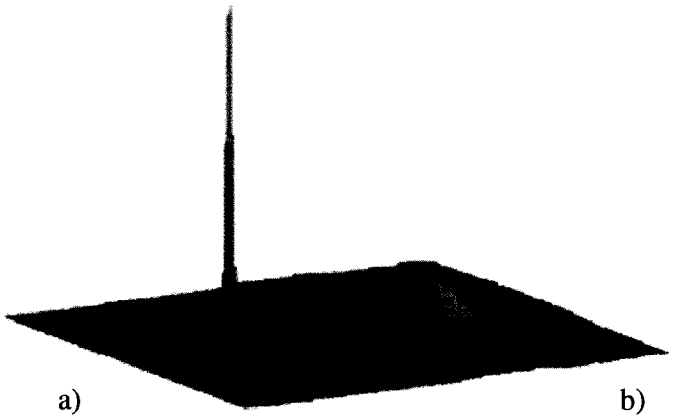


**Figure 31: The effect of turbulence on a telescope imaging system: (a) long-exposure PSF with no turbulence; (b) long-exposure PSF with turbulence.**

The illustration of the PSF reconstruction process can be seen in Figure 32. To improve science-camera images, the PSF is estimated in the post-processing stage (red dashed section), which uses the residual wavefront error (data measured by the WFS) and the DM mirror-mode error commands (i.e., closed-loop residual command coefficients sent to the DM) during the exposure time. Equations 1.11 and 1.12 show that the target object ($O$) can be rebuilt by deconvolving $I$ (science-camera image) and the estimated

PSF. It must be noted that rebuilding $O$ is limited by the WFS/DM sampling of the AO system.

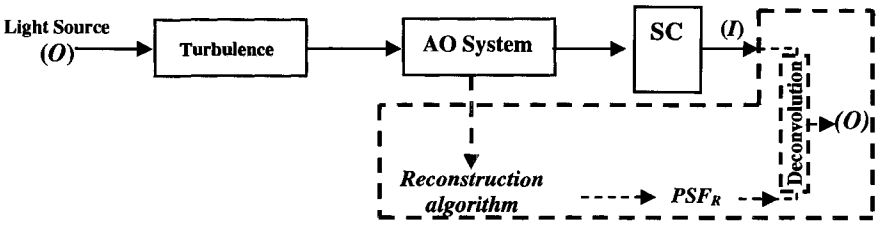


**Figure 32: Illustration of PSF reconstruction: the red dashed section in the figure represents the PSF reconstruction in the post-processing stage, later *I*, and the *PSF* can be used to reconstruct *O*.**

The PSF obtained by an AO system is space-variant. This space-variance originates from the different viewing directions of the AO system (at the guide star, GS) and the object of interest (in the direction relatively close to the guide star). Therefore, AO systems are anisoplanatic, but if the angular separation between the GS and of the object of interest is fairly small, the anisoplanatism does not influence the long-exposure PSF. It must be noted that even the off-axis performance of AO-system results are better than seeing-limited telescopes. Figure 33 illustrates the effect of anisoplanatism that degrades the performance of an AO system relative to the angular separation between the GS and the object of interest.

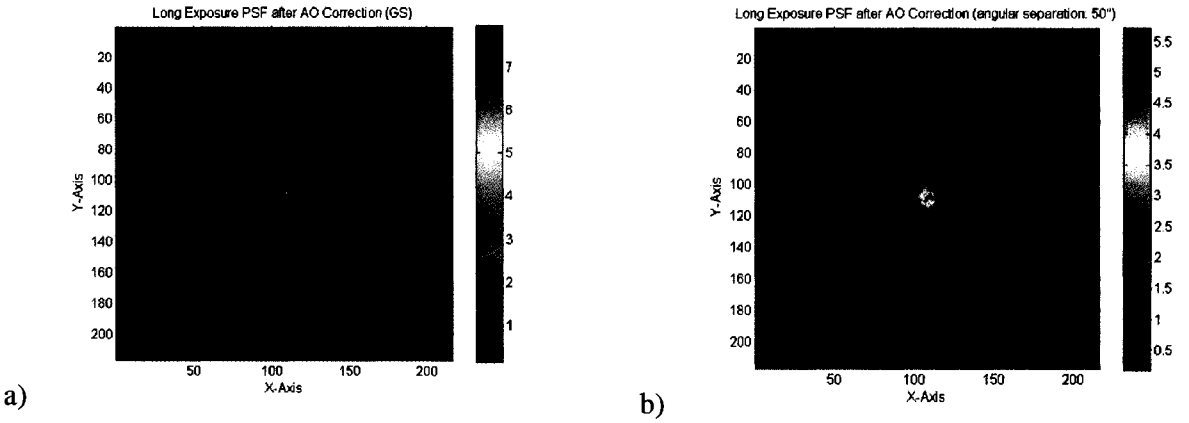


a) b)

**Figure 33: Long exposure PSFs after AO correction in direction of the guide star: (a) PSF obtained on the science camera in the direction of the guide star; (b) PSF obtained on the science camera in the direction of the object of interest at 50" separation.**

## 5.3 PSF Reconstruction from a Classical AO System

In order to reconstruct the PSF from a classical AO system, a variation of Veran's [31] methodology has been used. The method has the advantage of a PSF estimation based on the data measured synchronously with the observation. The PSF estimation can be done (in the post-processing stage) by averaging several seconds' worth of instantaneous PSFs in order to get an estimate of the long-exposure PSF characteristic of the AO system. The optical transfer function (OTF) can be described as the response of an imaging system to a point source or point object. The system optical transfer function ($OTF_{Total}$) is the product of AO system OTF and telescope OTF. As described in Chapter 1, it is assumed that the PSF, therefore the OTF, is stationary over the pupil and is dependent on the separation $\rho$, within the telescope pupil, between a point $\vec{r}$ and a nearby point $(\vec{r}+\vec{\rho})$:

$$OTF(\vec{\rho},\lambda)_{Total} = OTF(\vec{\rho},\lambda)_{AO}.OTF(\vec{\rho},\lambda)_{TEL} \quad (5.1)$$

where $OTF_{TEL}$ is the ideal auto-correlation function of the telescope pupil. However, it also contains the effects of the uncorrected static aberrations of the telescope. $OTF_{AO}$ is the OTF of the sum of the phase of the turbulent atmosphere and of the DM shapes. The phase of the turbulent atmosphere is a function of time. In a closed-loop operation, the DM shape opposes the shape of the turbulent phase in order to compensate for atmospheric distortions.

The correction provided by an AO system is limited to the cut-off frequency of the DM, and only the mirror component of the incidental phase undergoes a correction while crossing the adaptive optics system. As explained in Chapter 1.1.4, this results in a residual wavefront error that is time-variant. This residual phase of the turbulence must be estimated for each sample of the AO system in order to determine the long-exposure PSF. The residual phase after AO correction ($\varphi_{tot}$) can then be decomposed into the sum of the mirror component of the phase and an orthogonal component:

(i) $\varphi_{P\varepsilon}$, Mirror component (it will be referred as parallel component), which contains the low spatial frequency component up to the DMs cut-off frequency; and

(ii) $\varphi_O$, The orthogonal component, which is composed of the high spatial frequency introduced by the turbulence. This high-frequency component is beyond the spatial cut-off frequency of the DM.

$$\varphi_{tot} = \varphi_{P\varepsilon} + \varphi_O \tag{5.2}$$

Note that $\varphi_{P\varepsilon}$ and $\varphi_O$ are orthogonal to each other, and $\varphi_O$ is not corrected by the AO system; it will be estimated from the Kolmogorov model of turbulence (by using the

angle of arrival method, Chapter 3.3) since the spatial frequencies of $\varphi_O$ are beyond the WFS/DM cut-off frequency.

The long-exposure atmospheric $OTF_{AO}$ can be expressed as a function of the second-order statistical moment of the residual phase: Equation 5.3 presents this in terms of the structure function of the parallel and orthogonal residual phase [31]:

$$OTF(\vec{\rho},\lambda)_{AO} = \exp\left[-\frac{1}{2}\left(D_{\varphi_{P\varepsilon}}(\vec{\rho}) + D_{\varphi_o}(\vec{\rho})\right)\right] \tag{5.3}$$

Once the structure function of the parallel and the orthogonal phases are obtained, $OTF(\vec{\rho},\lambda)_{Total}$ can be calculated by substituting $OTF_{AO}$ in Equation 5.1. The calculation of these structure functions will be given in the next section. The determination of the OTF also leads to the determination of the estimated long-exposure PSF via a single discrete Fourier transform (Equations 1.11 and 1.12).

Figure 34 illustrates the parallel and the orthogonal residual phases. The phase aberration caused by the atmospheric turbulence is compensated for by the AO system. Due to the limitations of the DM, the WFS and the bandwidth of the overall AO system, the correction is partial and the high-frequency effects of the atmospheric turbulence ($\varphi_o$) are not compensated for. Therefore, in the science-camera image, a halo artifact is noticeable (Figure 33(a)). The goal of PSF reconstruction is to suppress this halo and detect the dimmer details of the science-camera image ($I$).

In the post-processing stage, the parallel component of the phase ($\varphi_{P\varepsilon}$) is calculated from the DM commands. The orthogonal component is then estimated from Kolmogorov's atmospheric turbulence theory, as follows:

(i) The AoA experiment is used to determine the Fried coherence length ($r_0$);

(ii) Phase screens are generated by Monte-Carlo simulation from the extracted $r_0$;

(iii) The parallel component of the phase (DM phase) is removed from the generated phase screens; and

(iv) The structure function of the orthogonal component of the phase is computed. Once the structure functions of the orthogonal and parallel components are calculated, the OTF (consequently the PSF) of the AO system can be obtained by Equation 5.1. The target object ($O$) is then reconstructed by using Equation 1.11.

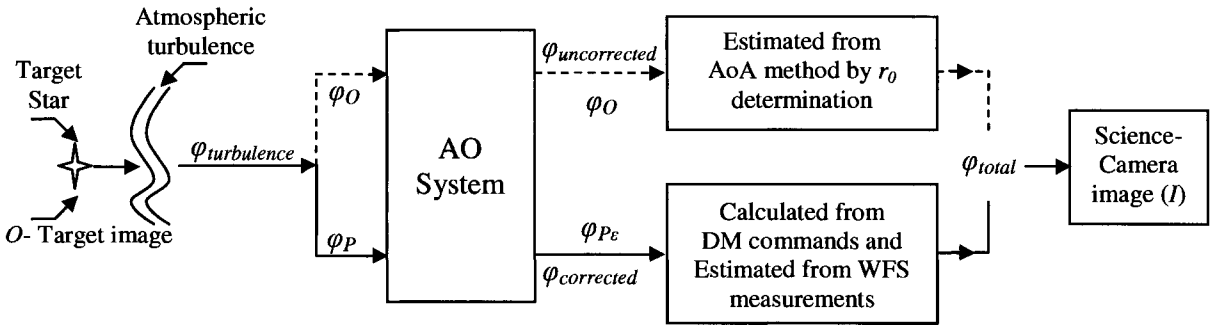


**Figure 34: Illustration of the parallel and the orthogonal residual phases; the solid lines represent the corrected phase and the dashed lines represent the uncorrected phase.**

### 5.3.1 Calculation of the Parallel Phase ($\varphi_{P\varepsilon}$)

The mirror component of the phase $\varphi_{P\varepsilon}$ is expressed as:

$$\varphi_{P\varepsilon}(\vec{r},t) = \sum_{i=1}^{N} \varepsilon_i(t) M_i(\vec{r}) \tag{5.4}$$

where $M$ are the influence functions of the mirrors in DM vector space, $\varepsilon$ are the DM mirror-mode error commands (residual commands coefficients sent to the DM), and $N$ is the number of modes corrected by the DM.

$$\varepsilon(t) = D^{+} w(t) \tag{5.5}$$

where $D^{+}$ is the command matrix for the AO system deduced from the pseudo-inverse of the interaction matrix $D$, and $w$ represents the WFS measurements. As illustrated in Chapter 1, from the phase fluctuations in different points across the telescope's pupil, the structure function of the phase aberrations can be computed as the variance of the difference between the value of the phase aberration at a point $\vec{r}$ and the value at a nearby point $(\vec{r}+\vec{\rho})$. The parallel-structure function of the residual phase is given by:

$$D_{\varphi_{P\varepsilon}}(\vec{r},\vec{\rho}) = \left\langle \left| \varphi_{P\varepsilon}(\vec{r},t) - \varphi_{P\varepsilon}(\vec{r}+\vec{\rho},t) \right|^2 \right\rangle \tag{5.6}$$

For a turbulent wavefront, according to Kolmogorov's atmospheric turbulence theory, the phase is stationary. Therefore, the structure function of that phase does not depend on the location, but only on the separation $\rho$. When the turbulent phase goes under AO correction (partial correction), the calculation of the structure function of the parallel component requires the averaging of four dimensional functions. This is very expensive in terms of computation time. Nevertheless, the pupil average structure function of the parallel component of the phase can be calculated as [32]:

$$\overline{D}_{\varphi_{P\varepsilon}}(\rho) = \left\langle \frac{\iint_P P(r)P(r+\rho)D_{\varphi_{P\varepsilon}}(\vec{r},\vec{\rho})dr}{\iint_P P(r)P(r+\rho)dr} \right\rangle \tag{5.7}$$

where $P$ is the pupil average function. This can be rewritten in a simpler form as:

$$D_{\varphi_{P\varepsilon}}(\vec{\rho}) = \sum_{i=1}^{N}\sum_{j=1}^{N} \left\langle \varepsilon_i \varepsilon_j \right\rangle U_{ij}(\vec{\rho}) \tag{5.8}$$

where $<\varepsilon_i\varepsilon_j>$ is the covariance matrix of the DM mirror mode error commands. This is updated at each loop cycle, and $U_{ij}(\vec{\rho})$ is the cross-correlation of the DM modes. $<\varepsilon_i\varepsilon_j>$ is obtained as:

$$\langle \varepsilon_i \varepsilon_j \rangle = D^+ \langle w_i w_j \rangle (D^+)' \tag{5.9}$$

$<\varepsilon_i\varepsilon_j>$ is also related to the SH WFS measurement covariance matrix $<w_iw_j>$.

### 5.3.2 The Cross-Correlation Functions ($U_{ij}(\rho)$)

$U_{ij}(\vec{\rho})$ is the cross-correlation of the DM modes, and can be represented as:

$$U_{ij}(\vec{\rho}) = \frac{\int P(\vec{r})P(\vec{r}+\vec{\rho})[M_i(\vec{r}) - M_i(\vec{r}+\vec{\rho})][M_j(\vec{r}) - M_j(\vec{r}+\vec{\rho})]d\vec{r}}{\int P(\vec{r})P(\vec{r}+\vec{\rho})d\vec{r}} \tag{5.10}$$

where $P(r)$ is the pupil function. The calculation of $U_{ij}(\rho)$ uses the Fourier transforms and the properties of the correlation function:

$$U_{ij}(\vec{\rho}) = \frac{F^{-1}\{2\,\mathrm{Re}\,al[F(M_iM_jP)F^*(P) - F(M_iP)F(M_jP)]\}}{F^{-1}(|F(P)|^2)} \tag{5.11}$$

In Equation 5.11, $F(\ )$ is the Fourier transform operator and * represents the complex conjugate. It must be noted that the calculation of $U_{ij}$ is computationally long but it is calculated only once, depending on the system's geometry.

### 5.3.3 Estimation of the Orthogonal Phase ($\varphi_O$)

The structure function of the orthogonal component of the phase can be computed by either numerical or analytical [34] methods. Here it is computed numerically using a Monte-Carlo model to generate phase screens, remove the mirror modes ($M_i$) from each phase screen and compute the average of the structure function for the corrected phase screens.

The orthogonal structure function of the residual phase is given by:

$$D_{\varphi_o}(\vec{r},\vec{\rho}) = \left\langle \left| \varphi_O(\vec{r},t) - \varphi_O(\vec{r}+\vec{\rho},t) \right|^2 \right\rangle \tag{5.12}$$

### 5.3.4 The Remaining Phase Error Calculations

The propagation of the WFS measurements' error onto the mirror modes originates from the turbulent phase's having a high-order component that gives a non-zero measurement on the WFS and is mistaken for a low-order component through the estimation process. It depends on the statistics of $\varphi_o$ and can be derived from the WFS measurements. $\varphi_o$ is not corrected by the AO system; it can be assumed to be in good agreement with the Kolmogorov atmospheric turbulence model and is computed numerically. This error is a consequence of the finite spatial sampling of the WFS and it has been shown to be the combination of two effects [37], namely, spatial aliasing and spatial cross-coupling. We will refer to it as the remaining error, $\varepsilon_r(t)$:

$$\varepsilon_r(t) = D^+ w(\varphi_o(r,t)) \tag{5.13}$$

and the covariance matrix of the remaining error, $C_{rr}$ is calculated from the numerical model, and can be given as:

$$C_{rr} = \left\langle \varepsilon_r \varepsilon_r^t \right\rangle \tag{5.14}$$

Equation 5.9 can be replaced by:

$$\left\langle \varepsilon_i \varepsilon_j \right\rangle = D^+ \left\langle w_i w_j \right\rangle (D^+)^t + C_{rr} \tag{5.15}$$

To account for the remaining error, $\varepsilon_r(t)$, and its effect on the reconstructed PSF, one can use Equation 5.15 and calculate the parallel component of the residual phase accordingly. Note that $C_{rr}$ is also calculated from the numerical model.

Once the parallel and orthogonal components of the phase are computed, the long-exposure $OTF_{AO}$ and $OTF_{Total}$ can be calculated accordingly (Equations 5.3 and 5.1). The determination of the OTF also leads to the determination of the estimated long-exposure PSF via a single discrete Fourier transform.

## 5.4 PSF Reconstruction from a Classical AO System: Numerical Evaluation

In order to test the PSF reconstruction, a numerical model has been performed to establish a baseline for future experimentation. The end-to-end model is entirely coded with Matlab using object-oriented programming and it comprises the models of the optical elements of a classical AO system. The parameters used in the numerical model are:

(i) Atmospheric turbulence is introduced by phase screens generated by a Monte-Carlo model with 1000 iterations;

(ii) Telescope diameter of 10 m;

(iii) A $D/r_0$ of 8; and

(iv) Pupil sampling on the wavefront is 108 pixels (px).

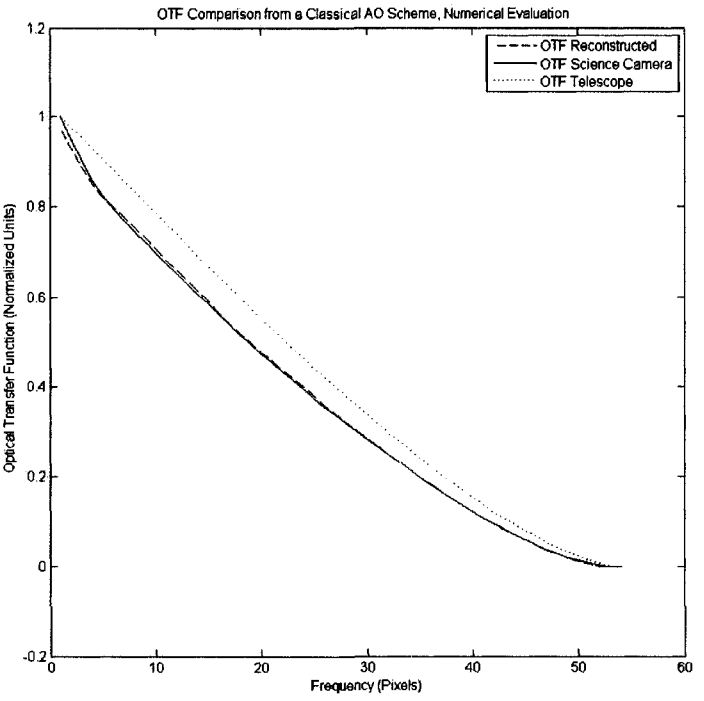


**Figure 35: Numerical evaluation of reconstructed OTF from a classical AO system and the gathered OTF from the science camera of the numerical model ($D/r_0$=8).**

In Figure 35, the comparisons between the numerical OTFs are represented. The dotted line represents the $OTF_{TEL}$ of the telescope itself in the absence of turbulence. The solid line is the $OTF_{AO}$ after the AO correction, which is gathered from the SC of the model. The dashed line represents the reconstructed OTF from the synchronous SH WFS data of the slopes obtained from the model. It is calculated using the parallel component of the phase and orthogonal component of the phase estimated from the Kolmogorov turbulence model. The reconstruction took place in the post-processing stage. The agreement between the OTF calculated and the OTF obtained from the AO correction is apparent. In this result, the remaining error calculations are taken into account. The

agreement in the numerical model ensured the successful OTF reconstruction, by the correct implementation of the methodology. The determination of the OTF led to the determination of the estimated long-exposure PSF via a single discrete Fourier transform (refer to Appendix B).

It must be noted that, for a better comparison, both real and reconstructed OTF plots are scaled so that the maximums of the real OTF are 1. The parameters used in the simulation are chosen to be compatible with modern telescopes.

## 5.5 PSF Reconstruction from a Classical AO System: Experimental Evaluation

In the experimental evaluation, the low-order-high-stroke Woofer mirror is used. The Woofer provides 25μm of maximum stroke and contains 52 actuators in the pupil (8 x 8). During the experiment, the turbulence generator is set to generate a $D/r_0 \approx 13$; pupil sampling on the WFS is 108 px.

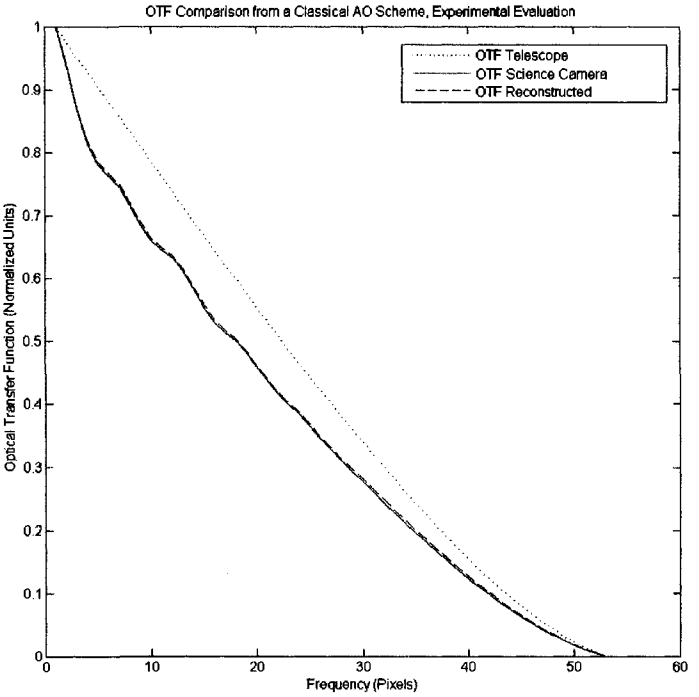


**Figure 36: Experimental evaluation of the reconstructed OTF from a classical AO system and the gathered OTF from the science camera of the experimental test bench ($D/r_0$=13).**

In Figure 36, the comparisons between the single dimensional cuts of the reconstructed OTF and the OTF obtained from the AO corrected image are represented. Here, the $r_0$ values generated in the turbulence generator at the time of the experiment were 1.52 mm (Appendix A) at a temperature difference of 103°C. The beam size was 2cm which corresponded to a $D/r_0 \approx 13$. The dotted line represents the $OTF_{TEL}$ of the telescope itself in the absence of turbulence. The solid line is the $OTF_{AO}$ after the AO correction, which is gathered from the SC of the model. The dashed line represents the reconstructed OTF from the synchronous SH WFS data of the slopes obtained from the model. It is calculated using the parallel component of the phase and orthogonal

component of the phase estimated from the Kolmogorov turbulence model (Section 4.5.3). In the estimation of the orthogonal phase, $r_0$ values are extracted using the AoA methodology (Section 3.3). The reconstruction took place in the post-processing stage. The agreement between the reconstructed OTF and the OTF obtained from the AO correction can clearly be seen. In this result, the remaining error calculations are taken into account. For further results, refer to Appendix B, "*Point-spread function reconstruction from Woofer/Tweeter adaptive optics bench.*"

## 5.6 PSF Reconstruction from a Dual DM AO System

In Appendix C, the paper, *"Derivation and experimental evaluation of a point-spread function reconstruction from a dual deformable mirror adaptive optics bench,"* written as part of the Ph.D. thesis project will be discussed. The article describes the proposed PSF reconstruction methodology, and the implementation in both the numerical model and in the experimental test-bed.

### 5.6.1 Estimation of the Parallel Phase ($\varphi_{P\varepsilon}$)

The Woofer/Tweeter AO system and its components have been presented in Chapter 4. In this architecture, improvements to Veran's methodology [31] are demonstrated in order to accommodate PSF reconstruction for an AO system with a separate tip/tilt mirror (TT), Woofer (WR) and Tweeter (TR). Therefore, this PSF reconstruction technique is applied to a system with three distinct mirrors. In the W/T architecture (TT + WR + TR), the parallel phase, $\varphi_{P\varepsilon}$, can be given by:

$$\varphi_{P\varepsilon}(\vec{r},t) = \sum_{i=1}^{N_{TT\ mirror}} \varepsilon_i(t) M_{itt\ mirror}(\vec{r}) + \sum_{i=1}^{N_{woofer}} \varepsilon_i(t) M_{iwoofer}(\vec{r}) + \sum_{i=1}^{N_{tweeter}} \varepsilon_i(t) M_{itweeter}(\vec{r}) \quad 5.16)$$

where $M$ is the influence function of the three mirrors in DM vector space, and $\varepsilon$ are the mirrors' open-loop coefficients (commands sent to three distinct DMs).

$$\varepsilon(t) = D^{+} w(t) \tag{5.17}$$

$D^{+}$ is the command matrix for the W/T system deduced from the pseudo-inverse of the interaction matrix $D$, and $w$ represents the WFS measurements.

When all the mirrors are running together, the DM vector space, $M_{itotal}$, can be expressed as the concatenation of vectors:

$$M_{i_{total}} = \left[ M_{i_{tt\ mirror}} \quad M_{i_{woofer}} \quad M_{i_{tweeter}} \right] \tag{5.18}$$

and $N_{total}$ (number of modes) where TT, WR, and TR modes are orthogonal to each other and become:

$$N_{total} = N_{TTmirror} + N_{woofer} + N_{tweeter} \tag{5.19}$$

and Equation 5.16 can be simplified to:

$$\varphi_{P\varepsilon}(\vec{r},t) = \sum_{i=1}^{N_{total}} \varepsilon_i(t) M_{itotal}(\vec{r}) \tag{5.20}$$

The parallel-structure function of the residual phase is given by:

$$D_{\varphi_{P\varepsilon}}(\vec{r},\vec{\rho}) = \left\langle \left| \varphi_{P\varepsilon}(\vec{r},t) - \varphi_{P\varepsilon}(\vec{r}+\vec{\rho},t) \right|^2 \right\rangle \tag{5.21}$$

The structure function of the parallel component of the phase can then be represented as:

$$D_{\varphi_{P\varepsilon}}(\vec{r},\vec{\rho}) = \sum_{i=1}^{N_{total}} \sum_{j=1}^{N_{total}} \left\langle \varepsilon_i \varepsilon_j \right\rangle \left[ M_{i_{total}}(\vec{r}) - M_{i_{total}}(\vec{r}+\vec{\rho}) \right] \left[ M_{j_{total}}(\vec{r}) - M_{j_{total}}(\vec{r}+\vec{\rho}) \right] \tag{5.22}$$

and the pupil average structure function of the parallel components becomes:

$$\bar{D}_{\varphi_{P\varepsilon}}(\rho)=\left\langle \frac{\iint_P P(r)P(r+\rho)D_{\varphi_{P\varepsilon}}(\vec{r},\vec{\rho})dr}{\iint_P P(r)P(r+\rho)dr} \right\rangle \tag{5.23}$$

This can be rewritten in a simpler form:

$$\bar{D}_{\varphi_{P\varepsilon}}(\vec{\rho})=\sum_{i=1}^{N_{total}}\sum_{j=1}^{N_{total}}\left\langle \varepsilon_i\varepsilon_j \right\rangle U_{ij}(\vec{\rho}) \tag{5.24}$$

where $<\varepsilon_i\varepsilon_j>$ is the covariance matrix of the WR and TR mirror commands. This is updated at each loop cycle:

$$\left\langle \varepsilon_i\varepsilon_j \right\rangle = D^{+}\left\langle w_i w_j \right\rangle (D^{+})^{t} \tag{5.25}$$

## 5.6.2 The Cross-Correlation Functions ($U_{ij}(\rho)$)

$U_{ij}(\vec{\rho})$ is the cross-correlation of the DM modes, and for a dual DM AO scheme, it can be represented as:

$$U_{ij}(\vec{\rho})=\frac{\int P(\vec{r})P(\vec{r}+\vec{\rho})\left[M_{i_{total}}(\vec{r})-M_{i_{total}}(\vec{r}+\vec{\rho})\right]\left[M_{j_{total}}(\vec{r})-M_{j_{total}}(\vec{r}+\vec{\rho})\right]d\vec{r}}{\int P(\vec{r})P(\vec{r}+\vec{\rho})d\vec{r}} \tag{5.26}$$

where $M_{total}$ represents cross-correlation between all modes for all DMs, for P($r$) is the pupil function. The calculation of $U_{ij}(\rho)$ uses the Fourier transform and the properties of the correlation function:

$$U_{ij}(\vec{\rho})=\frac{F^{-1}\left\{2\,\mathrm{Re}al\left[F(M_iM_jP)F^{*}(P)-F(M_iP)F(M_jP)\right]\right\}}{F^{-1}(\left|F(P)\right|^2)} \tag{5.27}$$

In Equation 5.27, $F$ is the Fourier transform operator and * represents the complex conjugate. Once the structure function of the parallel phase and the cross-correlation function are obtained, the structure function of the orthogonal part of the phase and the

remaining errors can be calculated as given in Chapter 5.3. The $OTF_{Total}$ from the W/T AO system can then be obtained. The determination of the OTF also leads to the determination of the estimated long-exposure PSF via a single discrete Fourier transform.

## 5.7 PSF Reconstruction from a Dual DM AO System: Numerical Evaluation

In order to test the PSF reconstruction with a dual DM AO system, a numerical modelling has been performed to establish a baseline for future experiments. The parameters used in the numerical model are:

(i) Atmospheric turbulence is introduced by phase screens generated using a Monte-Carlo model at 1000 iterations;

(ii) A telescope diameter of 10m;

(iii) A $D/r_0$ of 8; and

(iv) Pupil sampling on the WFS is 108 px.

In the simulation, the tip/tilt mirror corrects for the first two modes, the Woofer for 50, and the Tweeter for 80 modes.

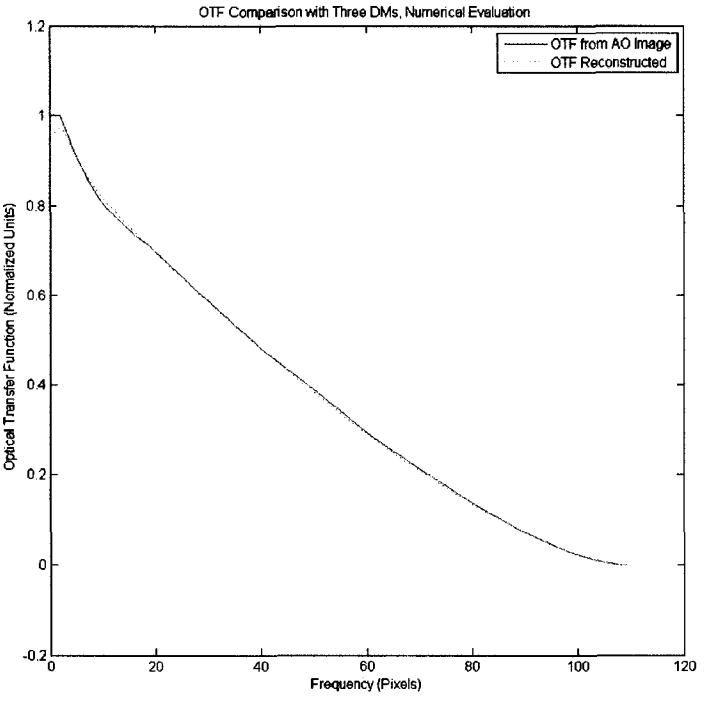


**Figure 37: Numerical evaluation of reconstructed OTF from dual DM AO system and the gathered OTF from the science camera of the numerical model ($D/r_0$=8).**

In Figure 37, the comparisons between the numerical OTFs are represented. The straight line is the $OTF_{AO}$ after the AO correction, which is gathered from the SC of the model. The dashed line represents the reconstructed OTF. The agreement between the single-dimensional cuts of the OTF obtained from the AO-corrected image and the OTF reconstructed from the SH WFS data ensured that a successful reconstruction was achieved through the correct implementation of the improved methodology. In this result, the remaining error calculations are taken into account.

## 5.8 PSF Reconstruction from a Dual DM AO System: Experimental Evaluation

The theory is validated by experimental evaluation; the simulation results ensured the successful reconstruction of the PSF. It must also be noted that, as previously discussed, the $D/r_0$ ratio is the defining factor, given that the atmospheric turbulence Fried ($r_0$) coherence length can be adjusted on the hot-air turbulence generator. For a given experimental setup, $D/r_0$ values between 14 and 36 are reproduced while keeping the entrance pupil $D$ constant. In the W/T architecture, the TR mirror is designed with sufficient spatial and temporal control bandwidth to compensate for the turbulence-induced phase distortion to the desired level of correction, but without sufficient stroke to correct the full amplitude of the expected errors. Large-amplitude errors are offloaded to the WR mirror, which has many fewer actuators but much greater stroke. As described in Chapter 4.4, in this architecture the tip/tilt mirror corrects for the first two modes, the Woofer for 50, and the Tweeter for 80 modes.

The concept is in some ways a generalization of the interaction between AO and active control systems in telescopes, where a few low-order modes are offloaded to the secondary and primary mirrors. The differences are: (i) the number of modes to be shared between the mirrors is much higher, and (ii) the WR mirror compensates for a significant fraction of turbulence-induced wavefront errors. The experimental set-up for the PSF reconstruction from a dual DM AO system was previously given in Chapter 4.3.

In Figure 38, the OTF comparisons can be seen for a Temp Diff 30°C, beam size of 42 mm, $r_0$ of 3.01 mm corresponding to a $D/r_0$=14, and a Strehl Ratio of %71. There is an inconsistency between the single dimensional cuts of the azimuthally averaged OTFs

obtained from the AO corrected image and the OTFs reconstructed from the SH WFS data.

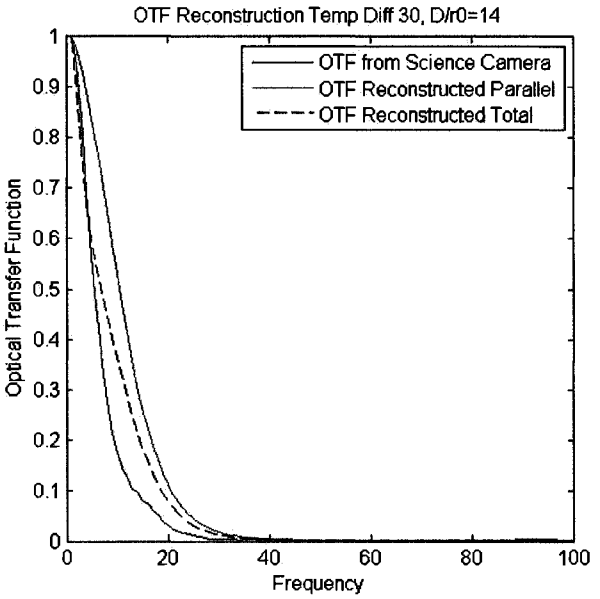


**Figure 38: Experimental OTF Reconstruction Results from the W/T Bench at D/r0= 14**

This inconsistency is due to the fact that the turbulence is not fully developed accordingly to the Kolmogorov turbulence regime (due to heat dissipation before mixing). The correlation between the turbulent phase and the telescope is an autocorrelation, and at small distances this does not cause a deviation. In the case of $D/r_0=14$ there is diffusion in the turbulence generator at low temperature differences. Therefore, the AoA variance calculation does not hold as the structure function of the turbulent phase deviates from the theoretical behavior. This inconsistency on the structure function calculation causes the discrepancy on the OTF at larger distances.

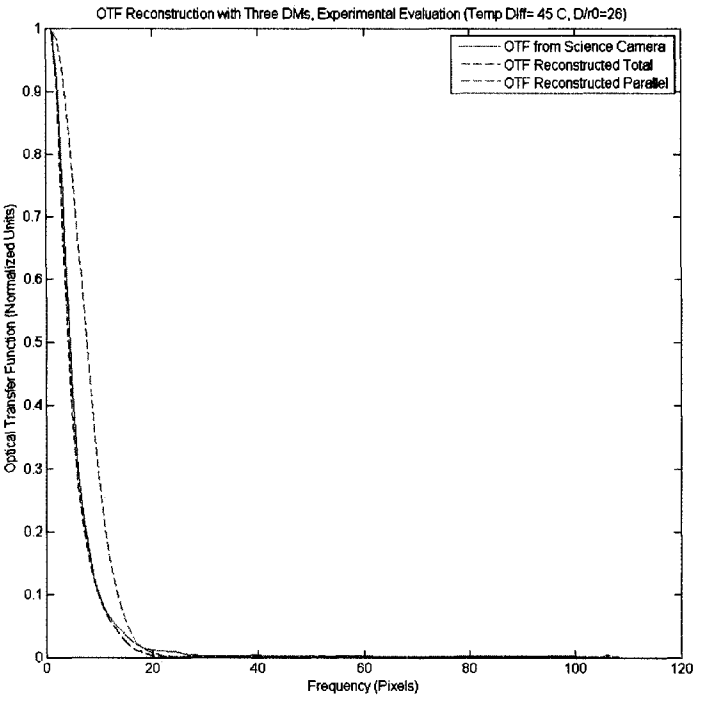


**Figure 39: Experimental evaluation of reconstructed OTF from a dual DM AO system and the gathered OTF from the science camera of the experimental test bench (D/r0= 26).**

In Figure 39, the comparisons between the single-dimensional cuts of the reconstructed OTF and the OTF obtained from the science camera of the W/T AO bench are represented. Here, the temperature difference used in the atmospheric emulation is 45°C, corresponding to $D/r_0$=26. The red line represents the OTF reconstructed with the parallel component of the phase (partial reconstruction). The dashed line represents the $OTF_{Total}$ reconstructed, calculated by the parallel component of the phase and orthogonal component of the phase estimated from the Kolmogorov turbulence model (Section 5.3.3). The $r_0$ values are extracted using the AoA methodology (Section 3.3). The blue line is the $OTF_{AO}$ after the AO correction, which is gathered from the SC of the AO

system. The reconstruction took place in the post-processing stage. Even though a 12x12 AO system may have little effect under such large $D/r_0$ values, the agreement between the reconstructed $OTF_{Total}$ and the OTF obtained from the AO correction can clearly be seen. In this result, the remaining error calculations are taken into account. For further results, refer to Appendix C, "*Derivation and experimental evaluation of a point-spread function reconstruction from a dual deformable mirror adaptive optics bench.*"

## 5.9 Off-Axis PSF Reconstruction from a Dual DM AO System

In order to reconstruct the PSF from an off-axis target, several approaches have been implemented. One approach is to estimate a reference PSF from observed data, within the isoplanatic angle, and use it in a field where multiple point sources can be deconvolved using this reference. In this approach, the characteristics of the reference PSF may be assumed field-independent [37, 38]. However, this approach does not account for the temporal evolution of the turbulence profile [39]. The Strehl ratio can be defined as the ratio of the peak intensity in the PSF of an optical system to that of the perfect theoretical image that can be obtained from the equivalent system. The comparison of the Strehl degradation due to anisoplanatism measured from the image data, and the PSF degradation expected from the measured turbulence profiles has shown a promising level of agreement between predictions and measurements [40, 41, 42, 43]. Therefore, in the analysis of the numerical modelling, measurements of the turbulence profile have been used in estimating the off-axis PSF from the AO observations.

As described in Chapter 1.1.5, assuming that the $OTF_{AO}$ does not depend on the viewing direction but only on the separation $\rho$: The system optical transfer function (OTF) in the direction of the object of interest, that differs from the GS, is the product of the anisoplanatic OTF, the AO system OTF, and the telescope OTF. This permits the factorization of the anisoplanatic and of the guide star's OTFs.

$$OTF(\vec{\rho},\lambda)_{Total} = OTF(\vec{\rho},\lambda)_{Anisoplanatic}.OTF(\vec{\rho},\lambda)_{AO}.OTF(\vec{\rho},\lambda)_{TEL} \quad (5.28)$$

In the case of $OTF_{Anisoplanatic,}$ the degree of anisoplanatism is determined by the turbulence profile; $OTF_{AO}$ is the OTF of the sum of the phase of the turbulent atmosphere and of the DM shapes.

As described earlier, $OTF_{AO}$ can be given as:

$$OTF(\vec{\rho},\lambda)_{AO} = \exp\left[-\frac{1}{2}\left(D_{\varphi_{Pe}}(\vec{\rho}) + D_{\varphi_O}(\vec{\rho})\right)\right] \quad (5.29)$$

and $OTF_{Anisoplanatic}$ is the optical transfer function of the object of interest's distance from:

$$OTF(\vec{\rho},\lambda)_{Anisoplanatic} = \exp\left[-\frac{1}{2}\left(D_{\varphi_{Ani}}(\vec{\rho})\right)\right] \quad (5.30)$$

and $OTF_{total}$ can be given in terms of the structure functions [7]:

$$\begin{aligned} OTF(\vec{\rho},\lambda)_{total} &= \exp\left[-\frac{1}{2}\left(D_{\varphi_{Ani}}(\vec{\rho})\right)\right] \\ &\times OTF_{TEL}\exp\left[-\frac{1}{2}\left(D_{\varphi_{Pe}}(\vec{\rho}) + D_{\varphi_O}(\vec{\rho})\right)\right] \end{aligned} \quad (5.31)$$

In the W/T AO system, the phase aberrations in the direction of the guide star, $\varphi_{turbulence}(0)$, are measured and compensated for by the tip/tilt mirror and two distinct DMs, namely, the Woofer and the Tweeter. Here $(r)$ is a vector in the pupil plane. In the direction of the target object, the wavefront aberration will be called $\varphi_{turbulence}(\theta)$.

If one represents the total residual phase aberrations after the AO correction by $\varphi_{tot}(\theta)$ in the direction of the object of interest, the residual aberrations after AO compensation are illustrated in Figure 40. In this figure, the AO system compensates for $\varphi_{turbulence}(0)$. Given that $\varphi_{DM} = \varphi_P - \varphi_{P\varepsilon}$ and $\varphi_{turbulence}(0) = \varphi_P - \varphi_O$, the compensation in direction of the anisoplanatic target object results in a residual wavefront error that can be given as $\varphi_{tot} = \varphi_{turbulence}(\theta) - \varphi_{DM}$. In simplified form, this can be presented as:

$$\varphi_{tot}(\vec{\theta}) = \varphi_{turbulence}(\vec{\theta}) - \varphi_{turbulence}(0) + \varphi_{P\varepsilon}(0) + \varphi_O(0) \tag{5.32}$$

where $\theta$ is the altitude-dependent angular separation between the GS and the object of interest.

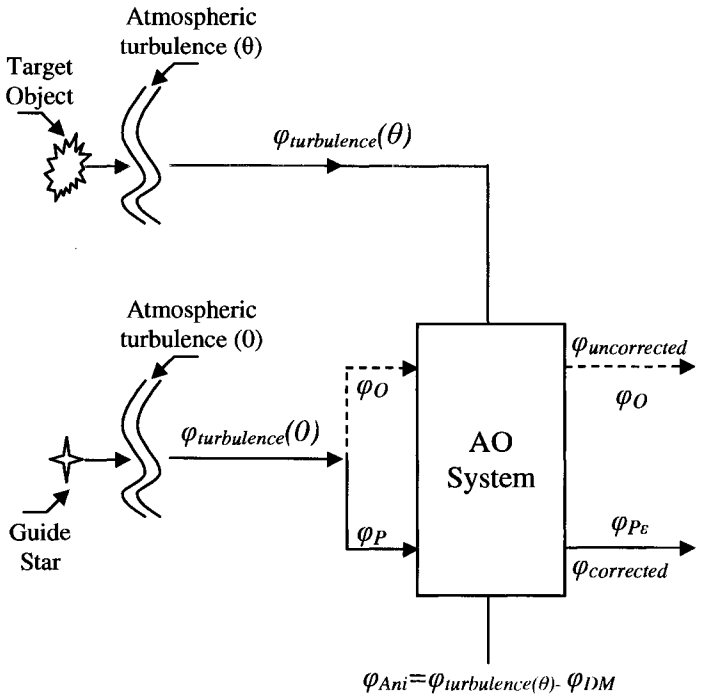


**Figure 40: Illustration of the residual phase for an anisoplanatic target object through the AO system. The solid line represents the corrected wavefront, the dashed line represents the uncorrected wavefront, and the red line represents the wavefront originated from the anisoplanatic target object.**

Note that in this equation, the effect of the time delay is not taken into account. Additionally, the statistics of turbulence induce correlations between the wavefront aberrations in the direction of the object of interest and the AO correction.

### 5.9.1 Computation of the Anisoplanatic Structure Function

Given that $\varphi_{Ani} = \varphi_{turbulence}(\theta) - \varphi_{turbulence}(0)$ and $\varphi_{AO} = \varphi_{P\varepsilon} + \varphi_{O}$, the structure function for the $\varphi_{tot}$ can be written as [43]:

$$\begin{aligned} D_{\varphi_{tot}}(r_1, r_2) &= D_{Ani}(r_1, r_2) + D_{AO}(r_1, r_2) \\ &+ 2\left\langle \left| \varphi_{Ani}(r_1)\varphi_{AO}(r_1) + \varphi_{Ani}(r_2)\varphi_{AO}(r_2) - \varphi_{Ani}(r_1)\varphi_{AO}(r_2) - \varphi_{Ani}(r_2)\varphi_{AO}(r_1) \right| \right\rangle \end{aligned} \quad (5.33)$$

The cross-terms in the equation represent the spatial correlation between the residual-phase errors from the anisoplanatism and those from the adaptive optics correction. In AO corrections, a number of errors do not correlate with anisoplanatism, namely: (i) aberrations in the optical system, (ii) non-common path errors, and (iii) measurement errors. While the importance of the errors varies from one AO system's error budget to another, in general, the cross-term in Equation 5.34 will be very small, relative to the structure functions. Therefore, the cross-terms are neglected.

The structure function $D_{Ani}$ of the anisoplanatic component of the phase can be represented as [8, 9, 23]:

$$\begin{aligned} D_{Ani}(r_1, r_2) &= 2\Xi k^2 D^{5/3} \\ &\times \int_0^\infty C_N^2(z)dz \left\{ 2|\Omega|^{5/3} + 2\left|\frac{2}{D}(r_1 - r_2)\right|^{5/3} - 2\left|\frac{2}{D}(r_1 - r_2) + \Omega\right|^{5/3} - 2\left|\frac{2}{D}(r_1 - r_2) - \Omega\right|^{5/3} \right\} \end{aligned} \quad (5.34)$$

where $k$ is the wave number ($2\pi/\lambda$), $D$ is the telescope's diameter, $r_1$ and $r_2$ represent two points in the pupil plane, the quantity $\Omega$ is:

$$\Omega(z) = \left(\frac{2z}{D}\right)\theta \tag{5.35}$$

where $\theta$ is the angular offset between the guide star and the target object and $z$ is the height in the atmosphere.

Note that the anisoplanatic structure function is defined as a function of $r_1$-$r_2$, in other words, $\rho$. It is assumed that this $D_{ani}$ is stationary over the pupil plane. In addition, $D_{Ani}$ is dependent on the telescope-aperture diameter, turbulence profile, angular separation between the guide star and the object of interest, and the observing wavelength.

## 5.10 PSF Reconstruction from an Off-Axis Dual DM AO System: Numerical Evaluation in the Direction of the Object of Interest

*Target object set at 50 arcseconds:* Figure 41 represents anisoplanatic transfer function for a target object at a 50'' offset from the GS; it is computed through Equation 5.31. In the simulation, the observing wavelength is 2.2 μm, for a 10-meter telescope. In this picture, due to the anisoplanatism that is generated by orienting the target object in the x-axis, the anisotropy can be seen. It must be noted that despite this anisotropy, the structure function is stationary over the pupil plane.

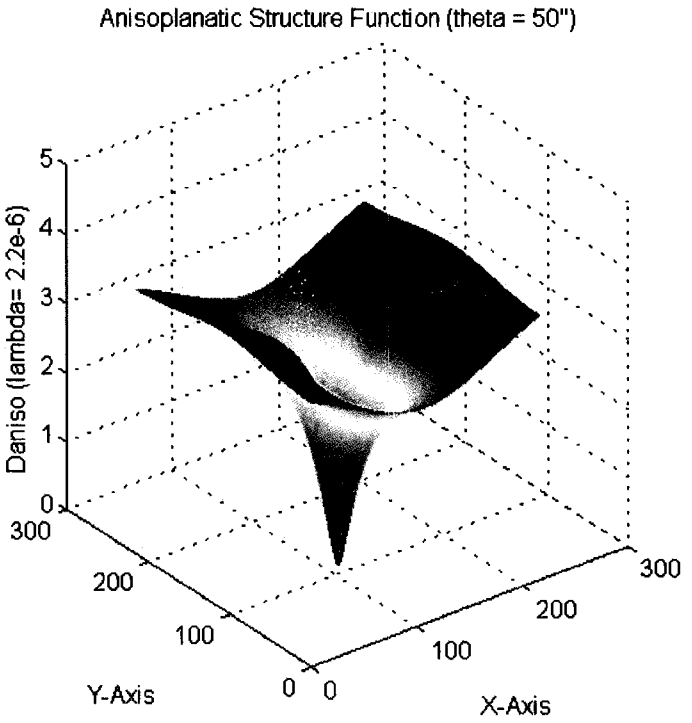


**Figure 41: In anisoplanatic structure function calculated for 16" angular separation; the anisotropy is noticeable.**

Figure 42 illustrates the reconstructed OTF from the target object, and it must be noted that even in the smaller angular offsets, the degradation in the obtained final image from the AO system is noticeable. It must be noted that the $OTF_{Anisoplanatic}$ depends only on the anisoplanatic structure function.

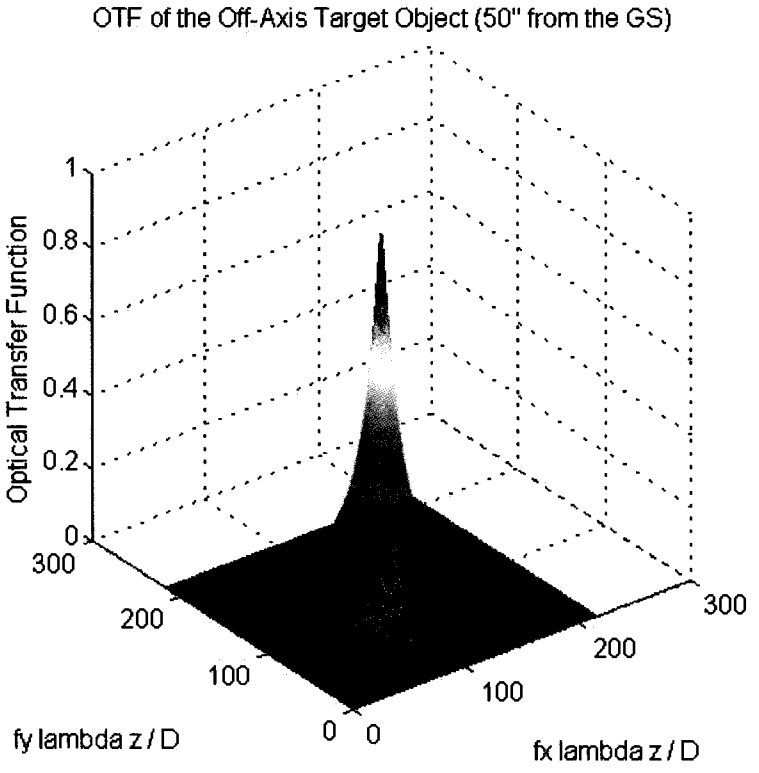


**Figure 42: Reconstructed OTF from the target object at 50-arcsec. separation from the guide star.**

Figure 43 represents a comparison between the single dimensional cuts of the azimuthally averaged anisoplanatic OTF reconstructed and the OTF obtained from the AO-corrected image (from the SC of the model). The agreement in this result ensured that a successful reconstruction was achieved through the correct implementation of the methodology.

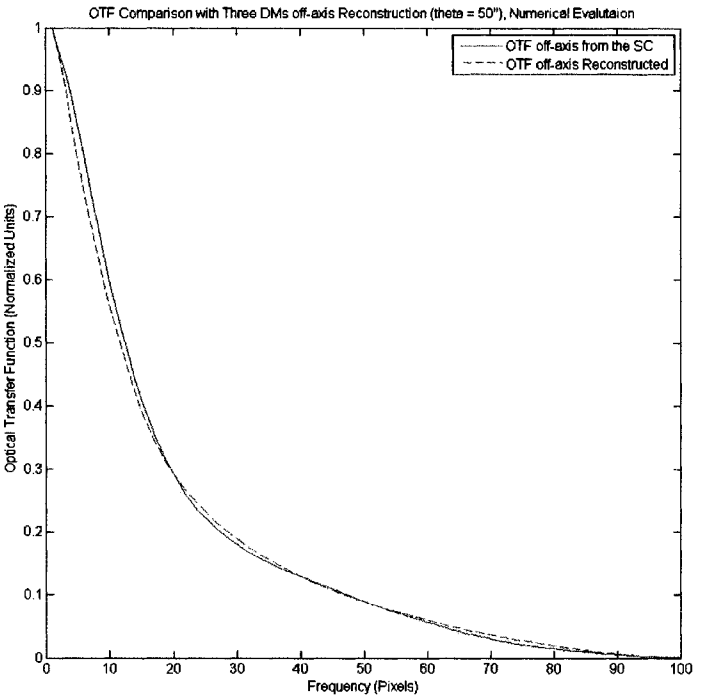


**Figure 43: Numerical evaluation of reconstructed anisoplanatic OTF from dual DM AO system (50'' separation) and the gathered OTF from the science camera of the numerical model ($D/r_0$=8).**

It must be noted that in the case of 50-arcseconds separation, the target object is significantly far from the angular separation of the isoplanatic angle (32.5 arcseconds) defined in the numerical model. At large-angular separations, the target object and the GS are far from each other and the correlation between them is very small even though the effect of anisoplanatism is large. Here, the assumption that the OTF is stationary holds. For further results, refer to Appendix D, "*Derivation and numerical evaluation of an off-axis point-spread function reconstruction from Woofer/Tweeter adaptive optics bench.*"

# 6. Conclusions

With the off-axis PSF reconstruction from a dual DM AO system as a general objective, a model-based experimental evaluation of PSF reconstruction from classical AO systems has been performed. The end-to-end model is entirely coded with Matlab, and it comprises the models of the optical elements of the Woofer-Tweeter AO bench. The software, the controllers and the opto-mechanical components of the W/T AO system have been integrated in the experimental test bench, and the loop has been successfully closed. The PSF reconstruction from the system model is a close match to the real system, and evidence of this is can be seen in Appendix B.

Building on the success of on-axis classical AO systems, the complexity of the model and the experimental set-up has been gradually increased to a multi-DM AO system. Results consist of the demonstration of the use of the WFS measurements and the DM commands in order to estimate the long-exposure PSF of a multi-DM AO system using a TT mirror, a WR and a TR for phase correction. The data used in the estimation of the PSF are gathered from the control computer after each acquisition. It is demonstrated that the long-exposure OTF, in the case of N number of DMs, may still be expressed as (i) the product of a static contribution (auto-correlation of the telescope's pupil in the absence of atmospheric turbulence); (ii) a contribution from the DM components of the phase (partially corrected by the AO system); and (iii) a contribution from the high-order component of the phase, which is not corrected by the AO system due to the limitations of the DMs and the WFS. This high-order component is estimated from the Kolmogorov model of turbulence, and the $D/r_0$ is derived from the Angle of Arrival (AoA) variances for an accurate estimation of this high-order component. The remaining error is defined

as the aliasing and cross-coupling between the DM and the high-order component, and this error is taken into account. The agreements between the numerical and experimental evaluation of the reconstructed OTFs and PSFs comparisons ensured the successful implementation of the methodology; evidence of this can be seen in Appendix C. It can be concluded that the improved methodology allows a good reconstruction of the PSF once the $D/r_0$ is accurately established in order to assess the multi-DM AO system performance. It must be noted that the reconstructed PSF is valid only within the isoplanatic patch.

Lastly, the complexity of the analysis and of the model is extended from a single light source to a multi-light source scheme, and the PSF reconstruction is achieved in order to accommodate for the anisoplanatic errors that degrade the performance of the AO systems at greater angular distances from the guide star. Evidence of this can be seen in Appendix D. The results consist of the demonstration of the use of the WFS measurements and the DM commands in order to estimate the long-exposure PSF of a guide star from a multi-DM AO system using a TT mirror, a WR and a TR for correction. The analytic methodology uses the observing wavelength, turbulence profile, angular offset, the aperture diameter, and the zenith angle in the prediction of the anisoplanatic PSF. For the guide-star PSF, data used in the estimation are gathered from the control computer after each acquisition. It is demonstrated that the long-exposure anisoplanatic OTF, in the case of N number of DMs, may still be expressed as (i) the product of a static contribution; (ii) a contribution from the DM components of the phase (partially corrected by the AO system); (iii) a contribution from the high-order component of the phase that is not corrected by the AO system due to the limitations of the DMs and

the WFS; and (iv) a contribution from the anisoplanatic structure function. The high-order component and the anisoplanatic component are estimated from the Kolmogorov model of turbulence, and the $D/r_0$ is derived by the Angle of Arrival variances for an accurate estimation of this high-order component. The remaining error is defined as the aliasing and cross-coupling between the DM and the high-order component. The agreements between the reconstructed OTF and PSF comparisons ensured that the effect of anisoplanatism in AO-compensated image quality can be improved by the successful implementation of the methodology, evidence of this can be seen in Appendix C. It can be concluded that the improved methodology allows a good reconstruction of the off-axis PSF once the turbulence profile is accurately established in order to assess the multi-DM AO system performance. It must be noted that the methodologies used in the computation of the reconstructed PSF and the OTF are valid only with the assumption that the PSF is stationary over the pupil plane.

One of the challenges in interpreting PSF over wide fields arises from the field-dependent evolution of the adaptive optics PSF. The methodology described in this thesis allows a quantitative analysis of such wide-field observations that can account for these effects. Finally, agreement between predictions and results may serve as an important on-sky validation that anisoplanatism is accurately understood in the context of near-infrared astronomical observations over large fields of view.

The outcome of the proposed research is important for performance assessment and for the improvement of the next-generation AO systems. Although the results are unique to the UVic W/T AO bench, the proposed PSF reconstruction methodologies will be applicable to other dual DM systems and to multi-DM AO systems. More precisely, the

importance of this thesis is to propose a PSF reconstruction technique for the Narrow Field Infrared Adaptive Optics System that will be the main facility adaptive optics system for the Thirty Meter Telescope. TMT will be one of the first of the next generation of extremely large telescopes. The availability of UVic AO laboratory W/T dual DM bench offers a unique opportunity to test the techniques developed in the theoretical part of the work on real hardware.

# 7. Future Work

It is expected that the next-generation AO systems will carry multi-DM AO systems (e.g., narrow-field infrared adaptive optics system that will be built for the Thirty Meter Telescope). In this context, the on- and off-axis PSF reconstruction methodology described in this thesis is a useful tool for scientists and engineers on the road to the post-processing of AO-system images obtained by GSMTs.

Future research work will examine the following areas:

- Experimental evaluation of the off-axis PSF reconstruction methodology in a similar architecture but with different DMs can be performed (e.g., a thousand actuator DM for the Tweeter and a piezo-stack DM for the Woofer to satisfy AO system requirements for TMT).
- Application of this technique to the imaging and deconvolution of stellar objects in a large field of view for multi-object AO systems (MOAO) would constitute a natural progression.
- Multi-conjugate AO systems (MCAO) employing DMs are conjugated to different heights in the atmosphere, and require tomographic reconstruction of atmospheric turbulence using wavefront measurements from multiple guide stars to form an estimate of the wavefront in a different direction. In this framework, PSF reconstruction for MCAO systems will be a natural progress.

# References

[1] I. S. Newton. "Opticks; or a Treatise of the Reflections, Refractions Inflections, and Colors of Light," *Opticks* by Sir. Isaac Newton New York, NY: *Dover Publications*, (1952).

[2] C.A. Primmerman, D. V. Murphy, D.A. Page, B.G. Zollars, H.T. Barclay, "Compensation of atmospheric turbulence optical distortion using a synthetic beacon," *Nature* (London), 353, 141, (1991).

[3] H. W. Babcock. "The Possibility of Compensating Astronomical Seeing." *PASP,* 65:229, (1953).

[4] D. L. Fried, "Statistics of a Geometric Representation of Wavefront Distortion," *J. Opt. Soc. Am.* 55, 1427, (1965).

[5] A. N. Kolmogorov, "Local structure of turbulence in incompressible fluids with very high Reynold's number," *Dokl. Akad.* Nauk SSSR **30,** 301–305 (1941).

[6] V. I. Tatarski, "Wave Propagation in a Turbulent Medium," *Dover publications*, (1961).

[7] A. M. Obukhov, "Structure of the temperature field in a turbulent flow," Izv. *Acad. Nauk.* SSSR Ser. Geograf. Geofiz. **13,** 58 (1949) [German translation in *Sammelband zur Statischen Theoric der Turbulenz* (Akademie Verlag, 1958)].

[8] A. M. Yaglom, "On the local structure of the temperature field in a turbulent flow," Doklady *Acad. Nauk.* SSSR Ser. Geograf. Geofiz. **69,** 73 (1949) [German translation in *Sammelband zur Statischen Theoric der Turbulenz* (Akademie Verlag, 1958)].

[9] D. L. Fried, "Statistics of a Geometric Representation of Wavefront Distortion," *J. Opt. Soc. Am.* 55, 1427, (1965).

[10] D. L. Fried, "Optical resolution through a randomly inhomogeneous medium for very long and very short exposures," *J. Opt. Soc. Am.* **56,** 1372–1379, (1966).

[11] F. Roddier, "The effects of atmospheric turbulence in optical astronomy," in *Progress in Optics,* E. Wolf, ed. (North-Holland, 1981), Vol. 19., (1981).

[12] R. J. Noll, "Zernike polynomials and atmospheric turbulence," *J. Opt. Soc. Am.* **66,** 207–211, (1976).

[13] G. A. Tyler, "Bandwidth considerations for tracking through turbulence," *Journal of the Optical Society of America,* 11:358–367, (1994).

[14] J. M. Conan, G. Roussel, and P. Y. Madec, "Wave-front temporal spectra in high-resolution imaging through turbulence," *J. Opt. Soc. Am.* A **12,** 1559–1570 (1995).

[15] G. Taylor, "The spectrum of turbulence," *Proc R Soc* London A 164:476–490, (1938).

[16] D. M. Winker, "Effect of a finite outer scale on the Zernike decomposition of atmospheric optical turbulence," *J. Opt. Soc. Am.* A **8,** 1568–1573, (1991).

[17] T. Von Karman, "Progress in the statistical theory of turbulence," *J. Mar. Res.* 7, 252–264, (1948).

[18] A. Consortini and C. Innocenti, "Estimate of characteristics scales of atmospheric turbulence by thin beams: comparison between the Von Karman and Hill-Andrews models," *J. Mod. Opt.* 51, 333–342, (2004).

[19] E. Masciadri and J. Vernin, "Optical technique for inner-scale measurement: possible astronomical applications," *Applied Optics.* 36, pp. 1320-1327, (1997).

[20] R. W. Wilson, "SLODAR: measuring optical turbulence altitude with a Shack-Hartmann wavefront sensor," *Mon. Not. R. Astron. Soc.* 337, pp.103-108, (2002).

[21] T. Von Karman, "Progress in the statistical theory of turbulence," *J. Mar. Res.* 7, 252–264 (1948).

[22] Roddier, "Adaptive Optics in Astronomy," *Cambridge University Press*, pp.15, (1999).

[23] V. I. Tatarski, "Wave propagation in a turbulent medium," *Dower Publications*, New York, (1961).

[24] G. Herriot, P. Hickson, B.L. Ellerbroek, D.A. Endersen, T. Davidge, D.A. Erickson, I.P. Powell, R. Clare, M. Smith, L. Saddlemyer, J.P. Veran, "NFIRAOS: TMT facility adaptive optics with conventional DMs", *SPIE proceedings* 5903, (2004).

[25] R. Dekany, M. Britton, D. Gavel. B. Ellerbroek, G. Herriot, C. Max, J.P. Veran, "Adaptive optics requirements definition for TMT", *SPIE proceedings* 5490, 879-890, (2004).

[26] O. Keskin, L. Jolissaint, C. Bradley, "Hot-air optical turbulence generator for the testing of adaptive optics systems: principles and characterization," *Applied Optics*, Vol. 45, Issue 20, pp. 4888-4897, (2006).

[27] D. L. Fried, "Statistics of a Geometric Representation of Wavefront Distortion," *Journal of the Optical Society of America*, 55:1427–1435, (1965).

[28] M. Kasper, D. Looze, S. Hippler, R. Davies, and A. Glinderman, "Increasing the Sensitivity of a Shack-Hartmann sensor," *In Canterbury Conference on Wavefront Sensing and its Applications*, (1999).

[29] R. Conan, C. Bradley, P. Hampton, **O. Keskin**, A. Hilton, and C. Blain, "Distributed Modal Command for a Two Deformable Mirror Adaptive Optics System," *Applied Optics*, Vol. 46, Issue 20, pp. 4329-4340, (2007).

[30] J.P. Veran, F.Rigaut, H. Maiter, and D. Rouan, "Estimation of the adaptive optics long exposure point spread function using control loop data," *J. Opt. Soc. Am.* A, 14, (1997).

[31] J.P. Veran, "Estimation de la reponse impulsionelle et restauration d'image en optiique adaptative: Application au system d'optique adaptative du telescope Canada-France-Hawaii," *Ecole National Superieure des Telecommunications, Thesis*, (1997).

[32] S. Harder, A. Chelli, "Estimating the point spread function of the adaptive optics system ADONIS using the wavefront sensor measurements," *A&AS*, 142, 119, (2000).

[33] Fitzgerald M. in The 1st Victoria Workshop on AO-PSF reconstruction, ed. L. Jollissaint, J.-P. Veran, J. Christou, & T. Rimmele, *http://cfao.ucolick.org/meetings/psf reconstruction*, (2004).

[34] L. Jolissaint, J.P. Veran, "OPERA, an automatic PSF reconstruction software for Shack-Hartmann AO systems: application to Altair," *Proc. SPIE*, volume 5490, 151-163, (2004).

[35] E. Gendron, Y. Clénet, T. Fusco, G. Rousset, "New algorithms for adaptive optics point-spread function reconstruction," *Astronomy and Astrophysics*, Volume 457, Issue 1, pp.359-363, (2006).

[36] O. Keskin, R. Conan, C. Bradley, "Point spread function reconstruction from Woofer-Tweeter adaptive optics bench," *Advances in Adaptive Optics II*, volume 6272. Proc. SPIE, (2006).

[37] J.C. Christou, and G. Pugliese, "Photometric and Astrometric Analysis of Gemini/Hokupa'a Galactic Center Adaptive Optics Observations," *Publications of the Astronomical Society of the Pacific* (PASP), **116**:734–744, (2004).

[38] De Pater, I., Marchis, F., Macintosh, B., Roe, H., le Mignant, D., Graham, J. and Davies, A., "Keck AO observations of Io in and out of eclipse", *Icarus* 169, 250, (2004).

[39] E. Steinbring, et al, "Characterizing the Adaptive Optics Off-Axis Point-Spread Function. I. A Semi-empirical Method for Use in Natural Guide Star Observations," *PASP*, 114, 1267, (2002).

[40] V.V. Voitsekhovich, V.G. Orlov, S. Cuevas, R. Avila, "Efficiency of off-axis astronomical adaptive systems: Comparison of theoretical and experimental data," *A&AS*, 133, 427, (1998).

[41] T. Fusco, J-M. Conan, L.M. Mugnier, V. Michau, G. Rousset, "Characterization of adaptive optics point spread function for anisoplanatic imaging. Application to stellar field deconvolution," *A&AS*, 142, 149, (2000).

[42] Weiss, A., et al., in Astronomical Site Evaluation in the Visible and Radio Range, ed. J. Vernin, Z. Benkhaldoun, & C. Muñoz-Tuñón, ASP Conf. Proc., 266, 86, (2002).

[43] M.C. Britton, "The Anisoplanatic Point-Spread Function in Adaptive Optics," *PASP*, 118, 885, (2006).

# Appendix A:

## *Hot air turbulence generator for the testing of adaptive optics systems: Principles and characterization*

**Applied Optics,**

**Volume 45, Issue 20, pp. 4888 (2006)**

# Hot-Air Optical Turbulence Generator for the Testing of Adaptive Optics Systems: Principles and Characterization

**Onur Keskin [a], Laurent Jolissaint [bc], Colin Bradley [a]**

[a] University of Victoria, Department of Mechanical Engineering, PO Box 3055, Stn. CSC, Victoria, BC, V8W 3P6, Canada

[b] Herzberg Institute of Astrophysics, National Research Council, Victoria, BC, Canada

[c] Fonds National de la Recherche Scientifique, Berne, Suisse

**Abstract.** A statistically repeatable, hot air optical turbulence generator, based on the forced mixing of two air flows with different temperatures, is described. Characterization results show that it is possible to generate any turbulence strength up to $C_N^2 \Delta h \approx 6.10^{-10} m^{1/3}$, allowing a ratio of beam diameter to Fried's parameter as large as $D/r_0 \approx 25$ for one crossing through the turbulator, or $D/r_0 \approx 38$ for two crossings. The outer scale ($L_0 \approx 133 \pm 60mm$) is found to be compatible with turbulator mixing chamber size ($170$ $mm$) and inner scale ($l_0 \approx 7.6 \pm 3.8$ $mm$) is compatible with the values in the literature for the free atmosphere. The temporal power spectrum analysis of the centroid of the focused image shows a good agreement with Kolmogorov's theory. Therefore the device can be used with confidence to emulate realistic turbulence in a controlled manner. A calibrated $C_N^2$ profile, both in layer altitude and strength, is necessary for testing off-axis adaptive optics correction (as MCAO). A testing was done to calibrate the $C_N^2$ profile using

the SLODAR (Slope Detection and Ranging) technique. First results, with only one layer, show the validity of the approach and indicate that a multiple pass scheme is viable with a few modifications of the current set-up.



*OCIS codes: 010.1080, 010.7060, 010.1290*

## 1. Introduction

This paper describes a simple, characterized, and statistically repeatable optical turbulence generator based on the forced mixing of cold and hot air for use in laboratory testing of adaptive optics (AO) systems. It is an alternative to other techniques to simulate the optical effect of atmospheric turbulence, such as etched rotating phase screens that are expensive to manufacture and do not allow turbulence strength adjustment. This limitation prevents real-time assessment of AO control system performance versus turbulence strength and particularly high-$\sigma$ events (e.g. sudden bursts of turbulence). The Adaptive Optics Laboratory at the University of Victoria is currently investigating multi-conjugate adaptive optics (MCAO) and multi-object adaptive optics (MOAO) systems. Therefore, a hot air optical turbulence generator, based on a previous design by Jolissaint [1] (the prototype), has been developed.

In order to generate real optical turbulence (i.e. turbulent fluctuation of the refractive index), one needs to create dynamic turbulence (i.e. velocity) and temperature fluctuation of the air flow. This is achieved by mixing two air flows with different temperatures in a confined space: the turbulence chamber. The air intake at one end of the

channel remains at room temperature (cold intake), the other intake is heated (hot intake) and both fans are operated at identical fixed velocities. The turbulence generator is versatile for emulating $C_N^2$ and wind velocity by changing the fan speeds and ΔT. Due to the fact that the prototype was made out of wood, temperature differences were limited to approximately 40K, giving rise to $r_0$ values of about 4 mm minimum. In order to create stronger turbulence (i.e. smaller $r_0$), an all Aluminum design was developed allowing maximum hot intake temperature of about 200 C.

In the MCAO/MOAO studies, anisoplanatism is a critical issue, and for that reason it is necessary to reproduce off-axis decorrelation of the optical turbulence in the laboratory environment. For the experimentations at the UVic AO bench, it has been computed that the reproduction of anisoplanatism effects can be achieved by emulating two layers of turbulence with equivalent thickness of ~1km. This is larger than the natural case (~ 100 m) but acceptable to demonstrate deformable mirror (DM) conjugation. These layers are positioned at equivalent altitudes of 5Km and 15 Km relative to the AO system's entrance pupil.

Fried parameter ($r_0$) of the turbulator has been calibrated versus the temperature difference (ΔT). The $C_N^2$ profile can be simulated using either two turbulence generators in series or two optical beam passes through one turbulator. The former approach provides layer independence while the latter requires no beam overlap to avoid spatio-temporal correlation between the two layers. The multi-pass scheme also requires altering the beam diameter to achieve a variable $D/r_0$ per layer.

The SLODAR technique (Wilson [2]) (Slope Detection and Ranging) was performed to characterize the $C_N^2$ profile. The results of characterizing a turbulent layer are presented herein:

- Section 2 recalls the effect of atmospheric turbulence on optical beam propagation.
- Section 3 outlines the turbulator design.
- Section 4 discusses the principles and experimentations of characterization methods.
- Discussions and conclusions are presented in Section 5 and 6 respectively.

## 2. Effect of Atmospheric Turbulence

### 2.1 Dynamic Turbulence

Dynamic turbulence, i.e. turbulence of the air velocity field, arises when the velocity fluctuations energy rate ($\approx U^2$) are much larger than the energy that can be dissipated by viscous friction.

$$\mathrm{Re} = \frac{KineticEnergy}{DissipatedEnergy} = \frac{UL}{v} \gg 1 \qquad (1)$$

*Re* is the Reynolds number, *L* the flow scale, and *v* is the kinematic viscosity $15.10^{-6}$ $(m^2/s)$. In the free atmosphere, *Re* is generally in the range of $10^6$ to $10^{10}$ and it can be assumed that the free atmosphere is fully turbulent in most conditions.

Kolmogorov's theory of atmospheric turbulence describes the spatio-temporal properties of the turbulence (see Tatarski [3]). The idea is that the turbulent flow is limited by an outer spatial scale, whereas the kinetic energy fluctuation is injected by a large scale displacement forcing of the wind. From this scale, after the forming of the turbulent

eddies, the air flow breaks down to smaller and smaller eddies up to an inner spatial scale where the kinetic energy is dissipated due to the viscous friction (the energy cascade of the turbulent flow).

## 2.2 Optical Turbulence and Fried's Parameter

Based on the fundamental Kolmogorov hypothesis, stating that the energy flow rate is constant from larger to smaller eddies, Obukhov [4] and Yaglom [5] have shown that in homogeneous and isotropic turbulence the structure function of the temperature field, defined by:

$$D_T(\vec{\rho}) = \left\langle \left[ T(\vec{r} + \vec{\rho}) - T(\vec{r}) \right]^2 \right\rangle_r \tag{2}$$

becomes:

$$D_T(\vec{\rho}) = D_T(|\vec{\rho}|) = C_T^2 \rho^{2/3} \tag{3}$$

Where, $C_T^2$ defines the structure constant of the temperature field. This equation is the starting point for the development of the theory of optical effects of the atmospheric turbulence.

The mixing of air masses at different densities, due to dynamic turbulence creates a random and turbulent field of refractive index. The refractive index fluctuation is directly proportional to the air density as given by the Dale-Gladstone law: $n - 1 = \alpha_n P / T$, where $\alpha_n = 80.10^{-8} K / Pa$ , $P$ is the air pressure and $T$ the air temperature. If the temperature field is turbulent, so will be the refractive index and its structure function is given by:

$$D_N(\rho) = C_N^2 \rho^{2/3} \tag{4}$$

where $C_N^2$ defines the structure constant of the refractive index, linked to $C_T^2$ by:

$$C_N^2 = \left(\frac{\alpha_n P}{T^2}\right)^2 C_T^2 \quad : \tag{5}$$

and as it can be shown that $C_T^2 \sim \delta T^2$, it becomes: (see Tatarski [3])

$$C_N^2 \sim \left(\frac{\alpha_n P}{T^2}\right)^2 (\delta T)^2 \tag{6}$$

where $\delta T^2$ is the temperature fluctuation variance within the turbulent flow (see also Lukin [6]for a measurement of $C_T^2$ and $C_N^2$ relationship). The Equation 5 is used as the fundamental relation of the hot air turbulence generator.

The Fried [7] parameter ($r_0$) is defined as the diameter of the telescope having the same Strehl resolution (integral of the optical transfer function (OTF)) than the atmospheric OTF. It can also be seen as a measure of the coherence length of the aberrated optical phase. The parameter is wavelength dependent, and related to the refractive index structure constant by (Roddier [8]):

$$r_0^{-5/3} = 0.4234(2\pi/\lambda)^2 \int_0^\infty C_N^2(h)dh \tag{7}$$

where $\lambda$ is the optical beam wavelength.

The main effect of the optical turbulence in an optical beam having a diameter $D$ is to create phase aberrations. When expressed in the Zernike polynomial basis, the aberration variances can be shown to be proportional to the ratio $(D/r_0)^{5/3}$, and decrease with the aberration's radial order $n$ (see Noll [9]).

Optical turbulence is created in the laboratory by mixing hot and cold air with a judicious selection of temperature difference, wind velocity (fan power) and optical beam diameter to achieve $D/r_0$ ratios compatible with the average working conditions at good

astronomical sites. The turbulence generator has one layer, and it will be assumed that the $C_N^2$ remains constant in this layer. In Equation (7), the integral can be replaced by the factor $C_N^2 \Delta h$, where $\Delta h$ is the layer thickness. Note that $r_0$ is temperature dependant via the $C_N^2$ temperature dependence. This characteristic enables its value to be tuned by changing the temperature difference between the hot and cold intakes.

## 2.3 The Outer and Inner Scale Effects of the Optical Turbulence

The outer scale $L_0$ is the upper limit of the turbulent flow extension. This scale limit has the effect of damping the low order optical aberrations, relative to the case of an infinite extension of the flow (Winker [10]) as it is assumed in the Kolmogorov [11] model; therefore the Kolmogorov model overestimates the effect of turbulence. The Von Karman [12] (VK) empirical phase power spectrum is generally used to take into account the effect of the $L_0$-damping effect on the low orders (i.e. low spatial frequencies) and is given by:

$$\phi(f) = \frac{0.023}{r_0^{5/3}} \left( f^2 + \frac{1}{L_0{}^2} \right)^{-11/6} \tag{8}$$

where $f$ is the spatial frequency in the pupil plane.

The inner scale $l_0$ has basically the same effect for the high order aberrations, and the $l_0$-damping factor of the phase power spectrum can be approximated with:

$$\eta[l_0] = \exp(-l_0{}^2 f^2) \tag{9}$$

Another, more sophisticated model for inner scale damping is provided by the Hill-Andrew empirical damping factor (see Consortini [13]) but is not discussed here. The cutting spatial frequency associated to a given Zernike polynomial in the radial order $n$ is

given by, (Conan [14]), $fc= 0.37(n+1)/D$. Replacing the spatial frequency in Equation 9 with $f_c$, the inner scale damping becomes:

$$\eta[l_0] \approx \exp[-0.137(n+1)^2(l_0 / D^2)] \quad \textbf{(10)}$$

which gives an empirical relation that can be used to assess the $D/l_0$ ratio from Zernike aberration variances experimental measurement.

Due to the strong decrease of the VK power spectrum at high frequencies, the $l_0$-damping effect is generally negligible for astronomical telescopes, where $D>>l_0$. For our turbulator, however, effect of $l_0$ must be taken into account: $l_0$-damping is noticeable as D is $>\sim l_0$.

## 2.4 Temporal Properties of the Optical Turbulence

The temporal power spectrum of the Zernike aberrations induced by the turbulence has a power law dependency in $f^0$ or $f^{-2/3}$ at low frequencies and $\sim f^{-17/3}$ at high frequencies, Conan [13]. The temporal cutting frequency, or knee frequency, $f_c$ between these two regimes for a radial order $n$ is given by:

$$f_c = 0.3(n+1)\frac{V}{D} \quad \textbf{(11)}$$

where $V$ is the main layer velocity, $n$ the radial order of the polynomial and $D$ is the diameter of the telescope. To reproduce the same dynamical behavior in the turbulator, it is in principle sufficient to reproduce the $V/D$ ratio.

Equation 11 assumes a single layer, frozen (Taylor hypothesis) to the beam of the telescope. In our turbulator, due to its structure, Taylor hypothesis does not apply, but we will see (Section 4) that this is in fact a minor problem.

# 3. Turbulence Generator Design

## 3.1 Design Specifications for the Turbulence Generator

In section 2, spatio-temporal properties of the turbulent phase aberrations were defined by ratios. In order to emulate the same properties, as measured on the astronomical observation sites, these ratios must be reproduced in the turbulator:

- $D/r_0$, $D/L_0$, and $D/l_0$ which are related to the spatial properties, and
- $D/V$ which is related to the temporal properties

For a telescope of 8 m in diameter, in the free atmosphere, typical values can be given as: $D/r_0 \approx 40$, $D/L_0 \approx 0.08 \rightarrow 0.8$, $D/l_0 \approx 600 \rightarrow 2000$, and $D/V \approx 0.4 \rightarrow 1.6s$. If a 42 mm diameter optical beam is sent through the turbulator, an $r_0 = 1$ *mm can* be achieved by reproducing the ratio ranges with, $L_0 = 525$ *to* $52$ *mm*, $l_0 = 0.02$ *mm to* $0.07$ *mm*, $V = 0.026$ *to* $0.1$ *m/s*. Unfortunately, the inner scale is not adjustable in the turbulator due to the fact that real atmosphere is being used, so $l_0$ will be in the usual range of a few millimeters. Note that the lack of inner scale adjustability is not a drawback because the high order aberrations are not intended to be corrected. Indeed, with a beam diameter of 42 mm, and an $l_0$ value of $\approx 6$ mm, we find (Equation 10) that the $l_0$-damping becomes significant (1/e) for radial orders above 18 (I.e. Zernike aberrations J= 172 and above). For a moderate order AO system like MCAO or MOAO this attenuation is not an issue as aberrations amplitude is needed at low order mostly, and high order aberrations are in principle not affected by the correction, so it would still be possible to evaluate the performance of the AO system by looking at the low order aberrations attenuation. The isoplanatic angle of a turbulent profile is given by (Fried [15]):

$$\theta_{iso} = 0.314\frac{r_0}{\langle h \rangle}$$

*with,* **(12)**

$$\langle h \rangle^{5/3} = \frac{\int_0^\infty C_N^2(h) h^{5/3} dh}{\int_0^\infty C_N^2(h) dh}$$

Where $\langle h \rangle$ is the average altitude of the turbulent layers, relative to the telescope entrance pupil, weighted by the layer's strength.

If the isoplanatic angle must also be reproduced, the $C_N^2$ thickness must be broadened at the turbulator level which can be done by adding several turbulators in series. Unfortunately, this solution is not practical due to the limited space on most AO benches. Using the same turbulator several times (not yet implemented) is an alternative which can be achieved by folding the optical beam back and forth through the same turbulent area and carefully avoiding beam overlap (folding of the beam was previously studied by Smith [16, 17]). Beam diameter would have to be expanded or shrank if one wants to generate different $D/r_0$ values. Unwanted spatio-temporal cross-correlation between the emulated layers can be minimized by a careful separation of the beams into the turbulent chamber.

To put things in perspective, if the turbulator is set at an $r_0$ of 2 mm, with a double-pass, then, an average turbulent layer distance (equivalent altitude) of 13 m will give an isoplanatic patch of about 10 arc seconds, which is a typical value for most observatories. Such a distance, while not small, is certainly manageable in the constrained space of an AO laboratory, using a set of nearly parallel mirrors to fold the optical beam several times before resending it through the turbulator.

## 3.2 Turbulence Generator Design

Our turbulence generator (illustrated in the Figure 1) is made of Aluminum and has plates that divide the inner area into two ducts so that hot and cold air intake can mix-up in the turbulent chamber.

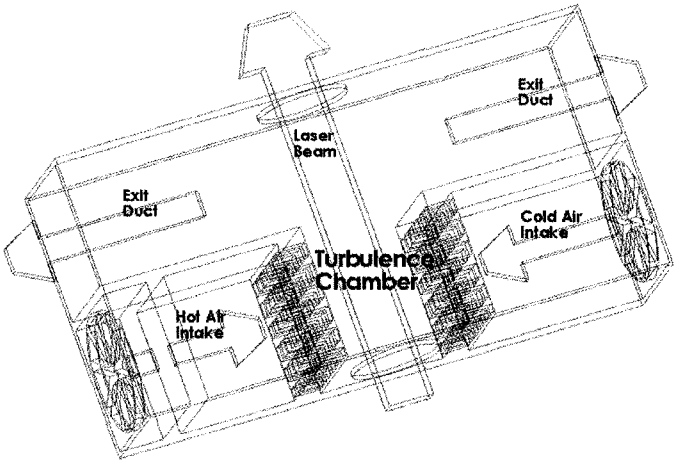


**Figure 1: The turbulence generator**

Variable fan speeds were selected. Off the shelf heaters, which fit the turbulator's dimensions, were used to allow maximum temperature differences of about *200K*. Honeycombs regularized the air flow before the mixing chamber.

Due to the fact that the temperature is a critical parameter, a temperature mapping on the hot and cold air side of the turbulence generator was required. Indeed the dissipation of the hot air into the duct could reduce the optical turbulence strength in the generator. The mapping proved that the optical beam path crossed the turbulent area where the temperature difference was maximum, optimizing the disturbance effect on the laser beam.

## 3.3 Optical Set-Up for Turbulator Characterization

The experimental arrangement is shown in Figure 2. The key features of this arrangement are:

- *A collimated laser beam* is created from a point light source (a laser through a spatial filter in our experiment).
- *Neutral filters* are used to prevent saturation or damage to the CCD chip.
- A stop is placed after the turbulence generator having the role of the entrance pupil on a telescope.
- The last lens has the function of simulating the telescope optics as seen from the CCD camera
- *CCD camera:* The long exposure focused images of the turbulent beam are collected by the CCD camera for the full width at half maximum experiment (section 4.1). For the angle of arrival experiment (section 4.2), the displacement of the instantaneous image is tracked by the CCD camera with *522 frames/sec* sampling frequency.

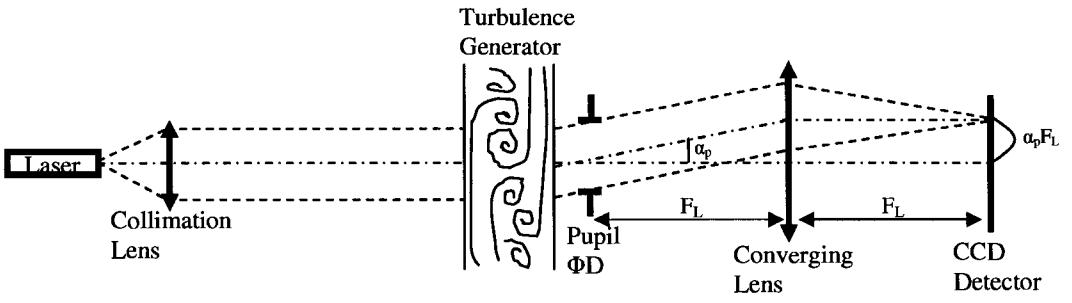


**Figure 2: Optical set-up for the Fried parameter characterization**

### 3.4 Optical Arrangement for $C_N^2$ Characterization

In order to characterize and calibrate the $C_N^2$ profile, a SLODAR set-up was implemented. The required set-up is similar as the one shown in Figure 2. The same turbulence generator is used. A Shack Hartman lenslet array is placed in a plane conjugated to the entrance pupil. However for the experimentation two or more guide stars (GS) had to be simulated with a known angle of separation between them. For that purpose, a pig-tailed laser diode unit, with fibers separated by a known angle (1.7 arc seconds as seen from entrance pupil) was used. In order to obtain the known angle of separation in the experimental set-up, a laser mount unit was manufactured by Micro-Electro Discharge Machining to obtain a precise 30 μm separation between the two star images on the SH WFS focal plane, corresponding to a separation of 2 pixels on the CCD. The diverging light from the fibers is collimated to a 25 mm diameter.

## 4. Principles and Experimentations of the Characterization Methodologies

### 4.1 FWHM Experiment

The Point Spread Function (PSF) is the pattern produced by the spread-out light from a single point source. Full Width at Half Maximum (FWHM) is the width of the light intensity profile at half the maximum peak intensity of the PSF. The maximum resolution available from a telescope of a diameter D is set by diffraction, in the ideal case of no turbulence, and the corresponding FWHM is $\lambda/D$ where $\lambda$ is the wavelength. Optical turbulence broadens the FWHM of long exposure images, and to a first approximation the contribution of the telescope and atmosphere on the FWHM add in quadrature. In the Kolmogorov regime, we get:

$$FWHM \cong \sqrt{(FWHM_{Telescope})^2 + (FWHM_{Atmosphere})^2} \cong \lambda / D\sqrt{1 + (D / r_0)^2} \qquad \textbf{(13)}$$

When $L_0 < \infty$ the $FWHM_{Atm} < 0.98\ \lambda/D$, so the equation above becomes an upper limit; this equation then provides a fast and simple way of determining an upper limit for $r_0$.

**Results:**

The long exposure turbulent PSF is shown in Figure 3. Seeing limited FWHM values gathered with $\Delta T = 53K$, and $\Delta T = 0\ K$ (no turbulence) are compared to assess the increase of the FWHM. From these values (using Equation 13), we found a Fried parameter (@ 500 nm) of $r_0 = 7.0 \pm 0.8\ mm$.

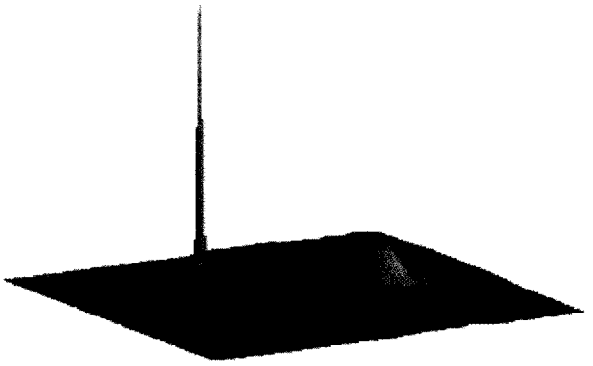

**Figure 3: Left: PSF without turbulence, Right: Turbulator "on" with ΔT= 53 K**

In this experiment, the damping effect due to the infinite outer and inner scale turbulence is not taken into account. Therefore, the actual $r_0$ can certainly be expected to be smaller than 7.0 mm.

## 4.2 The Angle of Arrival Method

The Angle of Arrival (AoA) is defined as the mean slope of the turbulent wavefront $W(x,y)$ into the pupil $P(x,y)$ of the telescope, or the exit pupil of the turbulator in this experiment:

$$\alpha_P = \frac{X_C}{F_L} = \frac{\iint P(x,y)\frac{\partial W}{\partial x}(x,y)dxdy}{\iint P(x,y)dxdy} \quad \textbf{(14)}$$

where $F_L$ is the focal length, and $X_C$ is the x-coordinate of the image centroid (see Figure 2). Equation 14 is given for the x-coordinate on the focal plane. The relation for y-coordinate is the same as x-coordinate and obtained by derivation versus y instead.

In the general case of a limited flow, the AoA variance is given, for a turbulent layer of thickness $\delta h$, by (Masciadri [18]):

$$\sigma^2_{AoA}[x,y] = (2\pi)^{4/3}\,0.033C_N^2\,\delta h \iint_{R^2} f_{X,Y}^2 (f^2 + L_0^{-2})^{-11/6} e^{-l_0^2 f^2}\left[\frac{2J_1(\pi Df)}{\pi Df}\right]^2 df_X\, df_Y \quad \textbf{(15)}$$

Only in the infinite scale regime ($L_0 = \infty$ *and* $l_0 = 0$), this equation has an analytic solution:

$$\sigma^2_{AoA}[x,y] = 2.8375C_N^2\,\delta h D^{-1/3} = 0.1698(\lambda/D)^2(D/r_0)^{5/3} \quad \textbf{(16)}$$

We see that the AoA variance decreases when increasing the pupil diameter. In the limited regime, this is still the case, but with departure from the $D^{-1/3}$ law at small and large values of $D$, due to the damping effect of $L_0$ and $l_0$. Masciadri [18] has suggested using this dependency as a way to measure the $L_0$ and $l_0$ in turbulent flows. The characterization of the turbulence generator using the AoA method is done in two steps:

- The heaters and the fans are set to a fixed temperature difference and wind velocity. The displacement of the instantaneous image centroid $(x_c, y_c)$ is tracked at

a sampling frequency of 522 frames/sec for 20 seconds, see Figure 5. The tracked displacements are later divided by the focal length $F_L$ to get the AoA.

- Empirical variance of the AoA is calculated for each diameter, and the $C_N^2 \Delta h$, $L_0$ and $l_0$ values are assessed by the fit of the theoretical model, given by Equation 15, to the empirical variances, see Figure 6.

The flow apparent velocity modulus can be determined from the knee frequency of the AoA temporal power spectrum: It can be shown (Tyler [19]) that at low and high temporal frequency the AoA spectrum has a power law dependency in, respectively, $f^{-2/3}$ and $f^{-11/3}$ (instead of $f^{-17/3}$ at high frequencies for Zernike polynomials). Now, the intersection of these two asymptotes defines the power spectrum knee frequency $f_c=0.3V/D$ which is in fact the same relation than the Zernike knee frequency for radial order n=1 (tip-tilt). This knee frequency is measured on the graphs of our experimental AoA temporal power spectrum, (by extrapolation of the low and high frequency asymptotes in a log-log representation, carefully avoiding the outer scale and inner scale damping areas), from which the apparent flow velocity V can be extracted. This can be repeated for a range of fan's command voltage, allowing the calibration of the turbulator velocity.

**Experimentation and results:**

An iris was used as the entrance pupil of the telescope (Figure 2), with variable diameters from 2mm to 20 mm. Temperature differences were selected in the range 33 K to 163 K. The expected behavior was that the magnitude of the AoA variance should decrease with an increase of the pupil diameter, according to Equation 16. That was indeed the case in our experiment. A spot tracking software was implemented to provide

the time and centroid displacement on $x$ and $y$ axes. As can be seen in the Figure 4, it seems that the displacement has practically the same amplitude in any direction: the optical turbulence as seen from the output of the turbulator seems isotropic.

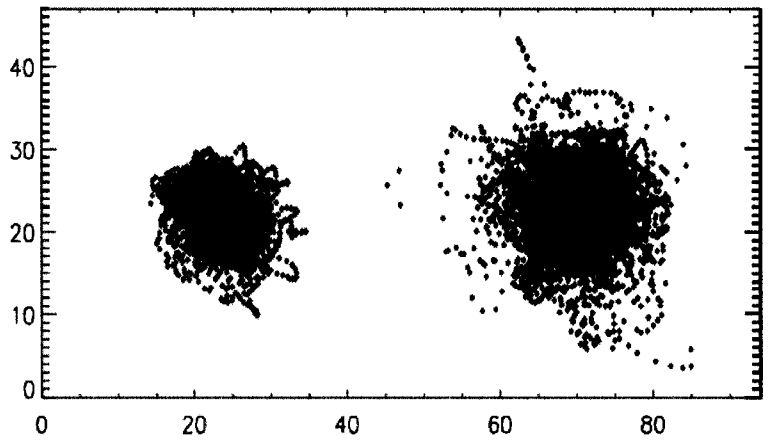


**Figure 4: Left: Centroid displacement for ΔT= 33 K, Right: ΔT= 163 K.**

**Pupil diameter 6 mm, tracking time 20 s**

In the Figure 5, all the variances for $\sigma_x^2$ and $\sigma_y^2$ are plotted for each experiment done with ΔT varying from 33 K to 163 K and beam diameters from 2 to 20 mm. It can be seen that the AoA variance is nearly isotropic ($\sigma_x^2/\sigma_y^2 \approx 0.84$) for all beam diameter and temperature differences as it can be expected. It is worth mentioning that the spatial properties of the turbulence inside the box is not examined, and it might not be perfectly isotropic. But the optical properties of the beam going through the turbulence are nearly isotropic.

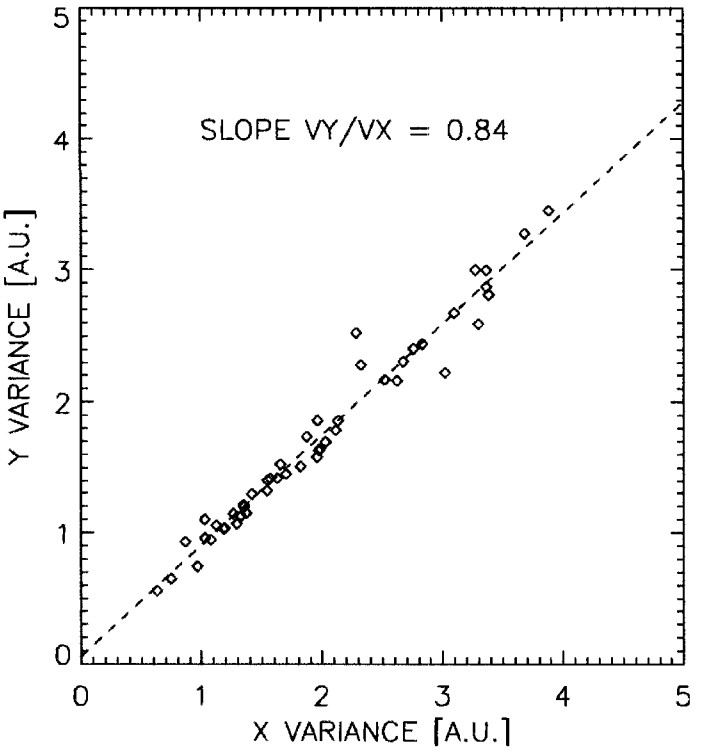


**Figure 5: Turbulator anisotropy**

In Figure 6 the AoA variance are shown with a fit of the theoretical model (Equation 15). We can see that there is a discrepancy relative to the $D^{-1/3}$ law expected for an infinite Kolmogorov regime, particularly evident for large beam diameter. In fact, a fitting with a $D^{-1/3}$ law cannot reproduce the experimental measurements at large diameter, and the fitting error RMS is about twice (1.94) that of the fitting error when using the VK based model. This behavior was noticeable on most $\Delta T$ cases, so we believe it is reasonable to associate this discrepancy to the effect of the outer scale damping. For the inner scale, though, the damping at small diameter is not really noticeable on the figure, but as the inner scale value extracted from the ensemble of our measurement (given below) is definitely compatible with most other authors values, we believe that the inner scale effect is present in our measurements and would become more

noticeable with a higher sampling of the AoA variance at low diameter – say in the range 1 to 5 mm.

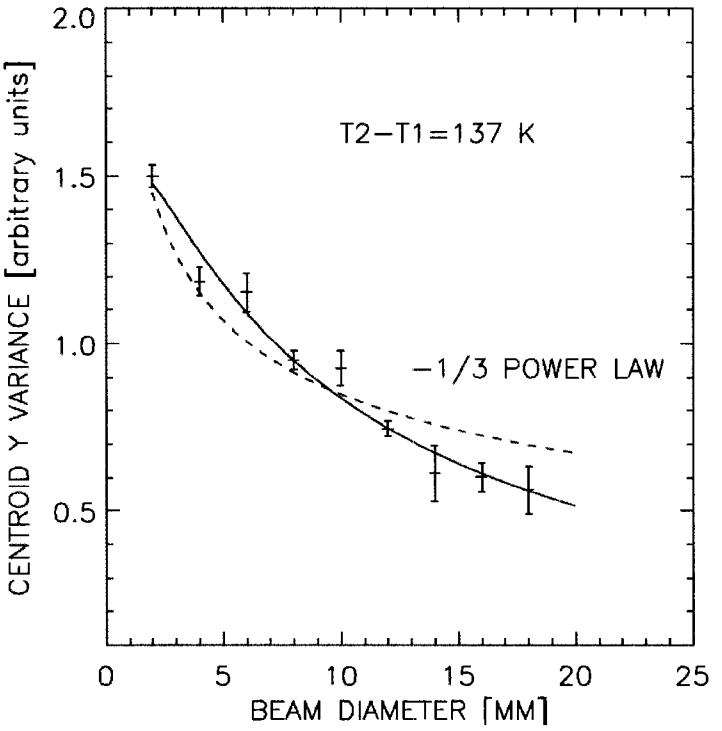


**Figure 6: Theoretical model fit to the variances, for ΔT= 137 K;**

**Continuous line: VK-based model; dashed line: Best fit of a $D^{-1/3}$ model.**

**Outer and inner scale:** As $L_0$ and $l_0$ are only related to the dynamic properties of the turbulent flow, the outer and inner scales are not dependent of the temperature differences occurring on the turbulence and the mean values of $L_0$ and $l_0$ amongst all temperature difference measurements are $L_0$= *133±60 mm* and $l_0$= *7.6±3.8 mm*. The $L_0$ value is compatible with the turbulence generator's dimensions mixing chamber ($17*17cm^2$), and the $l_0$ value is compatible with measurements made by other authors, Masciadri [18] (6 ±1 mm), and Lukin [20, 21] (2-6 mm).

**$C_N^2\Delta h$ and $r_0$:** In table 1 experimental values of $C_N^2\Delta h$ and Fried parameter $r_0$ at 500 nm are given. Using these $r_0$ values and a beam diameter of 42 mm, it is possible to

achieve, in the turbulence generator, $D/r_0$ ratios as large as 25 for a single pass, and 38 for double passes. The difference of $r_0$ values from the FWHM ($r_0$ = 7.0 mm) and AoA experiments can be explained by the damping effect of the outer and inner scales of the turbulence on the low and high order aberrations that were not taken into account in the FWHM experiment.

**Table 1: Experimental measured $C_N^2$ and associated $r_0$ values.**

| $\Delta T$ [K] | $C_N^2 \Delta h$ X [$10^{-10} m^{1/3}$] | $r_0$ X [mm] | $C_N^2 \Delta h$ Y [$10^{-10} m^{1/3}$] | $r_0$ Y [mm] | $C_N^2 \Delta h$ (mean) [$10^{-10} m^{1/3}$] | $r_0$ (mean) [mm] |
|---|---|---|---|---|---|---|
| 33 | 2.55 | 2.89 | 2.21 | 3.15 | 2.38 | 3.01 |
| 63 | 4.28 | 2.12 | 3.61 | 2.35 | 3.95 | 2.23 |
| 103 | 4.38 | 2.09 | 3.95 | 2.22 | 4.17 | 2.15 |
| 133 | 5.47 | 1.83 | 4.83 | 1.97 | 5.15 | 1.90 |
| 163 | 6.16 | 1.70 | 5.53 | 1.82 | 5.85 | 1.76 |

**$C_N^2 \Delta h$ and $\Delta T$:** In the Figure 7, combined results from the prototype (diamonds), and the characterization (squares) of the turbulence generator are shown. The continuity between results gathered from the two different turbulators demonstrate a good repeatability of the process.

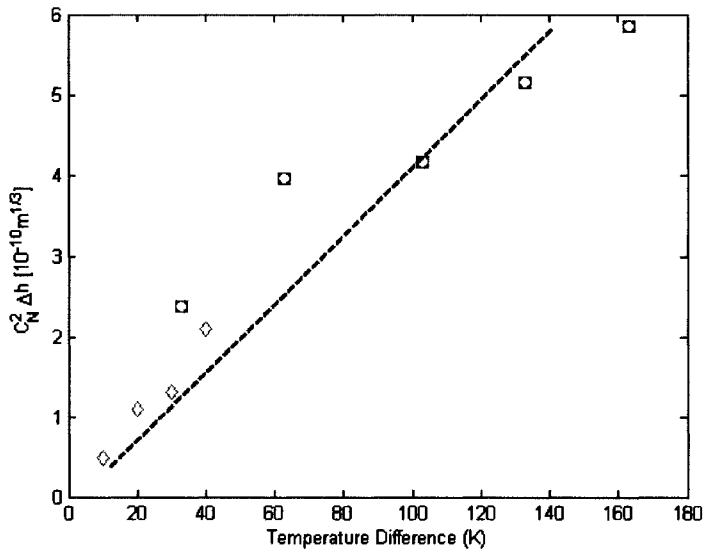


**Figure 7: The empirical relationship between ΔT and measured $C_N^2\Delta h$ average values**

**Squares: Current experiment, Diamonds: Low temperature Jolissaint's results**

Theoretically (Equation 6), $C_N{}^2\Delta h$ is proportional to $\Delta T{}^2$(see Tatarski [3]) but it seems in the results that $C_N{}^2\Delta h$ is looking proportional to $\Delta T$ as well. This can be explained by the fact that $\Delta T$ drops by diffusion from the output of the honeycomb, where the temperatures were measured, to the distance where the hot and cold are mixed in the chamber. The $\Delta T$ is then smaller than expected, giving rise to smaller values of $C_N^2\Delta h$. A way to counteract this effect would be to measure the temperature fluctuation right inside the turbulent mixing area using high-speed thermal probes.

**Apparent wind velocity:** The temporal power spectrum of the centroid fluctuation for the case $\Delta T = 90\ K$ and pupil diameter 12 mm is presented in the Figure 8. . From this graph, the knee frequency $f_c = 0.3V/D$ can be assessed to be approximately 20-30 Hz, from which it can be concluded that the apparent wind velocity of the air flow is in the range *0.8-1.2m/s.*

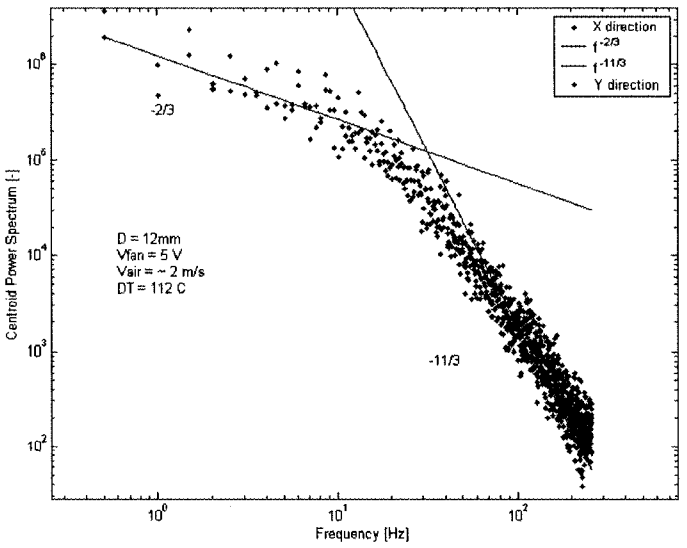


**Figure 8: Power spectrum of the centroid displacement (arbitrary units)**

Using a pupil diameter of 42 mm would give a knee frequency of 5.7-8.6 Hz, which is about 10 times higher than the classical value at the focus of an astronomical telescope, (e.g. *V=10m/s* gives $f_c$= *0.75 Hz*). It is therefore mandatory to implement slower fans in the turbulator. The effect of several layers of turbulence is to widen the knee region between low and high frequencies.

In our turbulator mixing chamber, none of the Taylor assumptions are valid: the flow mixing occurs at a fixed location, and there is no frozen translation. Moreover the turbulent flow also moves in the direction of the beam. But it must be possible to project any movement of the air masses on an arbitrary number of lateral frozen flow displacements (perpendicular to the optical beam) with appropriate apparent velocities. The fact that the temporal power spectrum of the angle-of-arrival (Figures 8 & 10) shows an asymptotic behavior compatible with a Kolmogorov optical turbulence, and a rather wide low to high frequency transition range tends to support the assumption of a multiple "apparent layers" with different velocities and $C_N^2$. Indeed, as each layer has its own

velocity and $C_N^2$ intensity, each layer's temporal power spectrum is displaced relatively to each others. The result is the broadening of the transition range between the -2/3 and -11/3 parts of the total temporal power spectrum.

## 4.3 The SLODAR Method

The principle of the SLODAR technique is the following:

- Two stars a few arc seconds apart are observed with a slope wavefront sensor (SH for instance).
- The cross-correlation of the time series of the slopes from lenslet to lenslet can be interpreted as a measure of the $C_N^2$ profile within the altitude range where the two star beams overlap.

Practically, the cross-correlation has to be deconvolved with the single star auto-correlation (taken from any of the two stars), and the $C_N^2$ is given by:

$$C_N^2 \sim F^{-1}\left\{\frac{F\left[C(\delta_i,\delta_j)\right]}{F[A(\delta_i,\delta_j)]}\right\}(\delta_i,0) \qquad \textbf{(17)}$$

Where $F$ is the Fourier transform operator, $\delta_{i,j}$ are the lenslet cross-correlation shifts in the WFS focal plane, $C(\delta_i,\delta_j)$ are the cross-correlation between the stars slopes (or centroid) time series $\delta_i,\delta_j$, and A is the auto-correlation for the same shift.

$C_N^2$ is retrieved from the deconvolved cross-correlation matrix along a line corresponding to the guide stars separation. In our case the two stars have been oriented along the x-axis of the WFS. To determine the $C_N^2$ profile absolute magnitude, we can use the turbulator's calibration curve $r_o(\Delta T)$ built using the AoA experiment (see Figure 7).

The vertical resolution of the $C_N^2$ measurement in SLODAR mode is given by $\delta H=D/n_s/\theta$, where $D$ is the optical beam diameter, $ns$ is the number of SH lenslets across the beam diameter (10 in our case), and $\theta$ the angular separation of the two guide stars, as seen from the entrance pupil of the SLODAR set-up (45 degrees in our case). The maximum sensing altitude is given by $H_{max}=D/\theta$.

**Results:**

The SLODAR experiment has been implemented for temperature differences from 30 K to 160 K, generating $r_0$ values from about 3 to 1.7 mm as calculated from AoA characterization. Centroid position for each star is tracked using an algorithm able to read separately both regions on the CCD sub-lenslet images around each star centroid. 10000 samples are taken, with a frame rate of 522 Hz, short enough to freeze the centroid motion during the exposure.

Figure 9 shows an example of centroid tracking for one of our measurements. Even with such a small separation (2 pixels) the two star's centroids are easily tracked. Mean values of the centroid time series are subtracted before computing the cross-correlation and auto-correlation matrices.

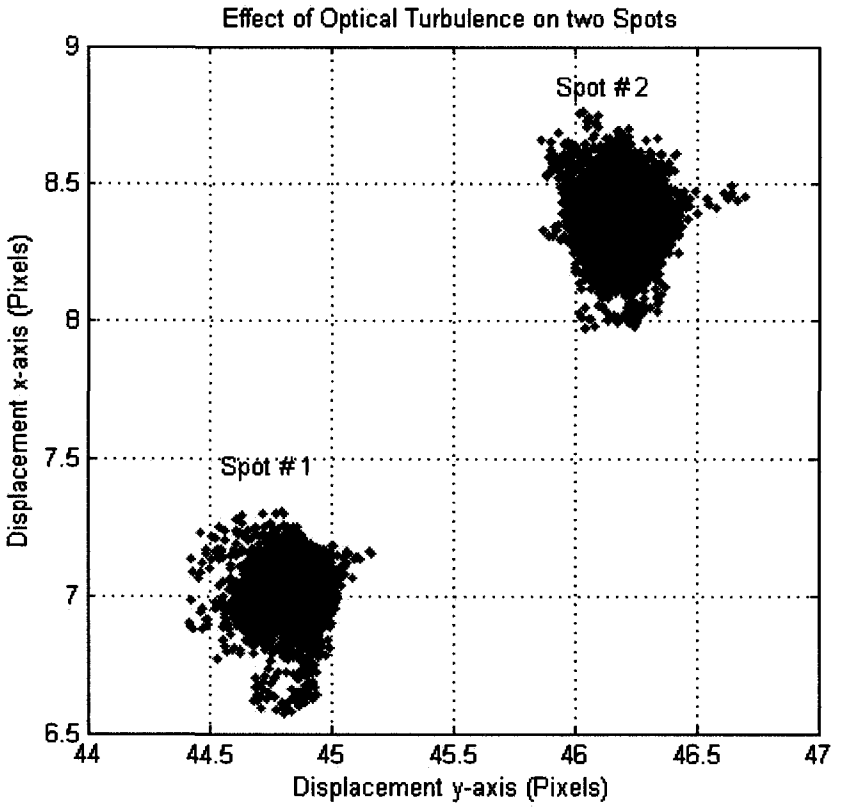


**Figure 9: Centroid movement for the two stars on a sub-image lenslet.**

On the Figure 9 the centroid displacement of the two guide stars, positioned at an angle of 45 degree, can be seen under the effect of the turbulence. It is also clear that the displacement amplitude is practically the same for both axes and for both stars: the optical turbulence seems isotropic.

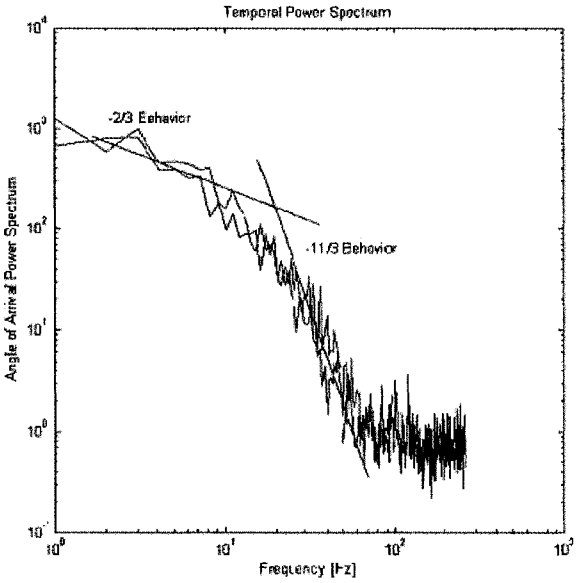


**Figure 10: Centroid Temporal Power Spectrum for both Stars ($\Delta T$= 90 K)**

Figure 10 shows the AoA temporal power spectrum for both stars: the *-2/3* and *-11/3* power law expected is clearly seen (dashed lines) for both the stars. The knee frequency is ≈ 20 Hz, which gives, with D= 42mm, an apparent velocity of 0.8m/s.

With such set-up, 10 repetitions of $C_N^2$ samples at altitudes of 0 and 21.24 m are gathered. It turns out that the - virtual - entrance pupil of the SLODAR set-up is in the middle of the turbulator. Therefore, we expected to find a one-layer $C_N^2$ profile concentrated at the first (0 m) sample (Equation 17).

Auto-correlation and cross-correlation algorithm have been implemented, and the deconvolution was done using a maximum entropy algorithm. Figure 11 shows an example of cross-correlation, auto-correlation, and deconvolved cross-correlation matrices. A unique central peak is indeed seen in the deconvolved $C_N^2$ profile. The cross-correlation is broader than the auto-correlation, which can be interpreted as the fact that the $C_N^2$ profile is not a single thin layer. To see the details of the $C_N^2$ profile within the turbulator, the SLODAR resolution of the set-up has to be increased to a few cm.

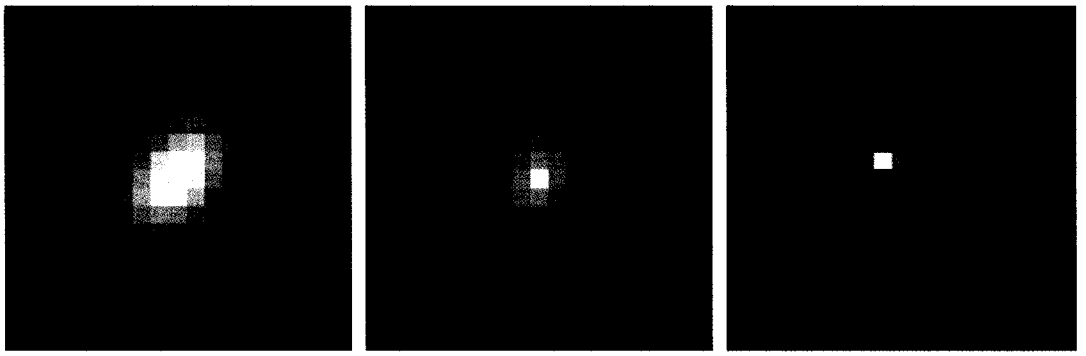

**Figure 11: Case at ΔT=160 K. Left: raw cross-correlation matrix, Center: auto-correlation matrix, Right: Deconvolved cross-correlation**

## 5. Discussions

In this section possible improvements on the set-up are discussed. First, a Shack-Hartmann WFS would be useful to characterize the turbulator's high order aberrations; measuring the damping effect of the inner scale will particularly be interesting. The high temporal frequency measurements can also be performed more precisely using a SH WFS, by the measurement of each mode's temporal power spectrum. Second, a sensitive issue is the fan's velocity: clearly, the velocity in our turbulator is too high, and slower fans must be implemented. The slower the air velocity, though, the more the hot air has time to cool before entering the mixing area, decreasing the optical turbulence strength. Third, vertical temperature gradient into the turbulator can be decreased by turning the turbulator by 90 degrees up around the axes of the input pipes, so the air rising due to natural convection will simply be embedded in the forced movement of the flow. Horizontal temperature gradient of the turbulator (the fact that $\Delta T^2$ is not necessarily constant along the horizontal path crossed by the light beam) can be improved by having double cold-hot half-channels instead of one. Fourth, the hot air channel should be thermally isolated up to the entrance of the mixing area to get rid of heat loss and

temperature gradient within the channel, which might be a problem when operating at low fan speeds, as stated above. Fifth, we have only implemented and tested the SLODAR procedure here, but we have not done any real $C_N^2$ characterization. This said, based on the fact that we were able to actually see a single layer at the apparent altitude we expected, with our poor vertical resolution, gives us confidence that a multiple folding might work for implementing a $C_N^2$ profile. Finally, the turbulator's $C_N^2$ ($\Delta T$) calibration curve can be improved by increasing the number of measurements and the sampling in the $\Delta T$ range.

## 6. Conclusions

From the AoA experimentation, it can be concluded that the spatio-temporal properties of the generated turbulence are in a very good agreement with Kolmogorov and Von Karman theories (including the effect of the outer and inner scales). Also, the generated optical turbulence seems isotropic. The $D/L_0$ and $D/l_0$ values are within the expected range. $L_0$= *133±60 mm* is compatible with turbulator's mixing chamber dimensions (170*170 mm). If a higher $L_0$ is required, the dimension of the turbulence generator has to be increased (or vice versa for a lower $L_0$). $D/r_0$ measurements are close to the specifications for an 8 meter diameter telescope when a temperature difference of 163 K is used. As the empirical relationship between $C_N^2$ and $\Delta T$ is predictable (but can be made more accurate with a better sampling), it can be concluded that higher temperature differences will generate stronger optical turbulence. $D/V$ is too small, but still in the correction range of the MCAO control system. A laboratory multiple-layer $C_N^2$ profile that can be measured using the SLODAR technique, using a hot air turbulence generator, appears to be feasible.

## Acknowledgments

The authors would like to thank the support of the University of Victoria, the NRC (National Research Council of Canada) for their technical support, and the Fonds National de la Recherche Scientifique Suisse. We also thank the anonymous reviewers for their useful comments, leading to a significant improvement of the paper.

## References

1. L. Jolissaint, "Optique adaptative au foyer d'un telescope de la classe 1 metre," Universite de Geneve, (Geneve, Suisse, 2000).
2. R. W. Wilson, "SLODAR: measuring optical turbulence altitude with a Shack-Hartmann wavefront sensor," Mon. Not. R. Astron. Soc. 337, pp.103-108, (2002).
3. V.I. Tatarski, "Wave propagation in a turbulent medium," translated by R.A. Silverman, Dover Publications, (New York, 1961).
4. A.M. Obukhov, "Structure of the temperature field in a turbulent flow," Izv. Acad. Nauk. SSSR, Ser. Geograf. Geofiz. (German translation in: Sammelband zur Statischen Theoric der Turbulenz, Akademie Verlag, Berlin, 1958) 13, p. 58, (1949).
5. A. M. Yaglom, "On the local structure of the temperature field in a turbulent flow," Doklady Acad. Nauk. SSSR, Ser. Geograf. Geofiz. (German translation in: Sammelband zur Statischen Theoric der Turbulenz, Akademie Verlag, Berlin, 1958) 69, p. 73, (1949).
6. V.P. Lukin, V.M. Sazanovich, "Investigations of turbulent characteristics in conditions of convection," Atmospheric and Ocean Physics, V.14, No.11, 1978, pp.1212-1215

7. D. L. Fried, "Optical resolution through a randomly inhomogeneous medium for very long and very short exposures," journal of Optical Society of America 56, (1966).
8. F. Roddier, "The effects of atmospheric turbulence in optical astronomy" E. Wolf, ed., Progress in Optics 19, 1981.
9. R. J.Noll, "Zernike polynomials and atmospheric turbulence," Journal of the Optical Society of America 66, (1976).
10. D. M. Winker, "Effect of a finite outer scale on the Zernike decomposition of atmospheric optical turbulence, " J. Opt. Soc. Am. A 8(10), 1568-1573 (1991).
11. A.N. Kolmogorov, "Local structure of turbulence in incompressible fluids with very high Reynold's number," Dokl, Akad. Nauk SSSR, 30(4), 301-305, 1941.
12. T. Von Karman, "Progress in the statistical theory of turbulence," Journal of Marine Research 7, 252-264, 1948.
13. Consortini et al., "Estimate of characteristics scales of atmospheric turbulence by thin beams: comparison between the Von Karman and Hill-Andrews models," Journal of Modern Optics, 51, 333-342, 2004
14. J.M. Conan, G. Rousset, P.Y. Madec. "Wavefront temporal spectra in high resolution imaging through turbulence", JOSA A, Volume 12, issue 7, 1559, July (1995).
15. D.L. Fried , "Anisoplanatism in adaptive optics, " JOSA, V. 72, 52-61, 1982
16. J. Smith, T.H. Pries, K.J. Shipka, M.A. Hamiter, "High-frequency plane –wave filter function for a folded path," Journal of Optical Society, V. 62, No. 10, pp 1183-1187, 1972.

17. J. Smith, "Folded-path weighting function for a high-frequency spherical wave," Journal of Optical Society, V. 63, No. 9, pp 1095-1097, 1973. V.V.

18. E. Masciadri and J. Vernin, "Optical technique for inner-scale measurement: possible astronomical applications," Applied Optics. 36, pp. 1320-1327, (1997).

19. G. A. Tyler, "Bandwidth considerations for tracking through turbulence," Journal of Optical Society, vol 11, 358-367, 1994.

20. V. P. Lukin, V.V. Pokasov, "Optical wave phase fluctuations", Applied Optics, Vol. 20, No.1, pp. 121-135, January 1981.

21. V.P. Lukin, V.L. Mironov, "Phase measurements of inner scale of atmospheric turbulence," Atmospheric and Ocean Physics, V.12, No. 12, pp 1317-1319 (1976).

# Appendix B:

## *Point spread function reconstruction from woofer/tweeter adaptive optics bench*

**Proceedings of SPIE, Advances in Adaptive Optics**

**Volume 6272, pp. 62724I (2006)**

# Point Spread Function Reconstruction from Woofer-Tweeter Adaptive Optics Bench

**Onur Keskin[a], Rodolphe Conan[a], Colin Bradley[a]**

[a] University of Victoria, Department of Mechanical Engineering, Adaptive Optics Laboratory PO Box 3055, Stn. CSC, Victoria, BC, Canada

**Abstract**

This paper describes a model-based and experimental evaluation of a point spread function (PSF) reconstruction technique for a Dual Deformable Mirror (DM) Woofer-Tweeter (W/T) Adaptive Optics (AO) system. In the W/T architecture, the Woofer is a low-order-high-stroke DM, and it is used to compensate for the low-frequency-high-amplitude effects introduced by the atmospheric turbulence. The Tweeter is a high-order-low-stroke DM that is used to compensate for the high-frequency-low-amplitude effects introduced by the atmospheric turbulence. The research concept of having Dual DMs allows the W/T AO system to have a high degree of correction of large amplitude wavefront distortion. The role of the UVic AO bench is to demonstrate the closed-loop wavefront control feasibility for a W/T AO concept to be used on the science instruments of the Thirty Meter Telescope (TMT).

**Keywords:** Point Spread Function, Adaptive Optics, Woofer-Tweeter AO System

# 1. INTRODUCTION

The correction provided by an AO system is partial due to the limited number of degrees of freedom of the deformable mirror (DM), and the spatial sampling of the wavefront sensor (WFS). As a result, the high order optical aberrations introduced by the atmospheric turbulence are not compensated. This translates into a halo in the image gathered after an astronomical observation. Consequently, the finer details of the AO image can not be detected due to a deficiency in contrast. One possible way to counteract this halo is the determination of the optical transfer function (OTF) of the AO system, and the restoration of the contrast in the post-processing stage. The determination of the OTF also leads, via a single numerical Fourier Transform, to the determination of the PSF, which is the impulse response of the AO system.

An AO system is most of the time a combination of a tip-tilt (TT) mirror (i.e. a flat mirror on a tip-tilt stage) and a DM or a DM carried by a tip-tilt mount. For the Extremely Large Telescopes (ELT), due to the unavailability of a DM manufacturing technology, it will not be possible to provide an AO correction with a use of a single high-order-high-stroke DM (containing large number of actuators) as is done in current AO systems on 4-10 meter class telescopes. Therefore, on the ELTs, a solution to this problem is the use of Dual DMs, so called woofer-tweeter (W/T) configuration. In this architecture, the woofer is a low-order-high-stroke DM, and it is used to compensate for the low-frequency-high-amplitude effects introduced by the atmospheric turbulence. The tweeter is a high-order-low-stroke DM that is used to compensate for the high-frequency-low-amplitude effects introduced by the atmospheric turbulence. The research concept of having Dual DMs allows the W/T AO system to have a high degree of correction of large amplitude

wavefront distortion. The TMT fulfills the goal of a concept called the Giant Segmented Mirror Telescope (GSMT) which was identified as the highest-priority new ground based facility for the first decade of the 21st century [1, 2], and it will carry science instruments such as Narrow Field Infrared Adaptive Optics System (NFIRAOS).

## 2. Point Spread Function

In an observation of a real object through an AO system, the image formation of the object occurs on an image plane (or telescope focal plane). The object plane can be described as the infinite distance in space where the real object is situated. A point on the image plane can be spotted by its position relative to the optical axis of the AO system by a bi-dimensional angular vector. The AO system is characterized by its impulse response $PSF\ (\vec{\alpha}, \vec{\beta})$, which represents the intensity received at the point $\vec{\alpha}$ of the image plane when the observation of the real object's intensity is on the direction $\vec{\beta}$.

A real astronomical object can be described as the sum of incoherent spatial lights generated from a target object. The long-exposure image gathered on the SC during an observation can then be defined as the superposition of images from the target object through turbulence and AO correction. If $O(\vec{\beta})$ is termed as the intensity distribution of the real object on the object plane, and $I\ (\vec{\alpha})$ is referred to as the intensity distribution of the long-exposure image on the image plane, the formation of an image through an AO system becomes:

$$I\ (\vec{\alpha}) = \int O\ (\vec{\beta})\ PSF\ (\vec{\alpha}, \vec{\beta})\ d\vec{\beta} \qquad \textbf{(1)}$$

It is generally assumed that the long-exposure PSF has the same shape over the whole field of view regardless of the viewing direction (within the isoplanatic patch, where the distortion level of the atmospheric turbulence is statistically the same everywhere in the field). The stationary $PSF\ (\vec{\alpha},\vec{\beta})$ can then be described as $PSF\ (\vec{\alpha},\vec{\beta}) = PSF\ (\vec{\alpha}-\vec{\beta})$, and $I$ becomes:

$$I\ (\vec{\alpha}) = \int O\ (\vec{\beta})\ PSF\ (\vec{\alpha}-\vec{\beta})\ d\vec{\beta} = O\ (\vec{\alpha}) \otimes PSF\ (\vec{\alpha}) \qquad (2)$$

In the Fourier domain, this convolution becomes a product:

$$\tilde{I}\ (\vec{f}) = \tilde{O}\ (\vec{f})\ .\ OTF\ (\vec{f}) \qquad (3)$$

$\vec{f}$ is the angular frequency vector, which is conjugated to the angular $\vec{\alpha}$ vector in the Fourier domain. The PSF is the response of the optical system to a point source, and its relationship to $I$, and $O$ can be given as a convolution, Equation 2. To improve the final AO images, the proposed work determines the PSF, in the post-processing stage, through the use of the residual wavefront error data measured by the WFS and mirror commands of the AO system (Figure 1). Once the PSF is known, the object can be partially rebuilt up to the spatial cut-off frequency of the telescope through a deconvolution process.

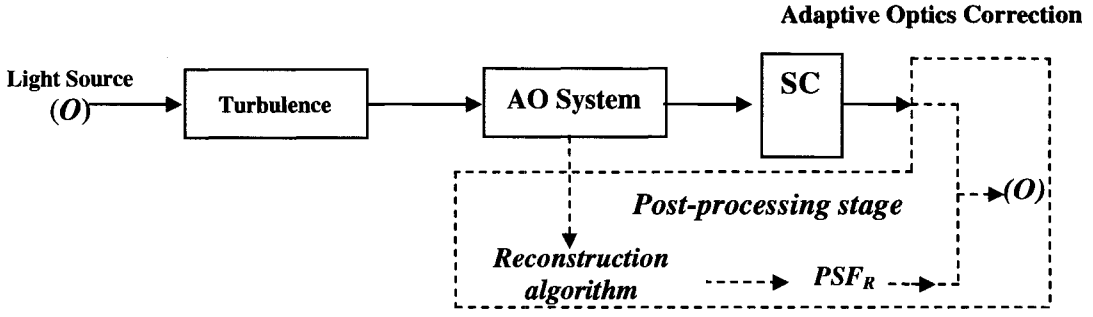


**Figure 1: Imaging principle and PSF determination on AO system**

## 3. Woofer-Tweeter AO Bench

In the W/T architecture, the tweeter mirror is designed with sufficient spatial and temporal control bandwidth to compensate for the turbulence-induced phase distortion to the desired level of correction, but without sufficient stroke to correct the full amplitude of the expected errors. Large amplitude errors are offloaded to the woofer mirror, which has many fewer actuators but much greater stroke. The concept is in some ways a generalization of the interaction between AO and active control systems in telescopes, where a few low-order Zernike modes are offloaded to the secondary and primary mirrors. The difference is that (i) the number of modes to be shared between the mirrors is much higher, and (ii) the woofer mirror compensates for a significant fraction of turbulence-induced wavefront errors.

The working scheme of the UVic W/T AO system can be seen in Figure 2. A planar wavefront generated by the light source goes through the atmospheric turbulence generator (Keskin [3, 4, 5]) and becomes aberrated. The degree of distortion of the wavefront is detected by the SH WFS. The purpose of the W/T AO system is to make this distorted wave front as flat as possible. TT mirror is a flat mirror which adjusts the position offsets of the incoming distorted wavefront by counteracting the apparent motion of the star. Both DMs use a grid of actuators to deform their physical shape to an opposing shape of the distorted wavefront. In the wavefront compensation process, the shape of both woofer and tweeter and also the angle of the TT mirror are determined by the AO controller (in closed loop), which uses the Shack-Hartmann WFS (SH WFS)

measurements. During this closed loop operation the WFS measures only the residual wavefront error (i.e. the uncorrected phase distortions of the wavefront). This process takes place in real-time, during an astronomical observation, to compensate for the constantly changing optical effects of the atmospheric turbulence.

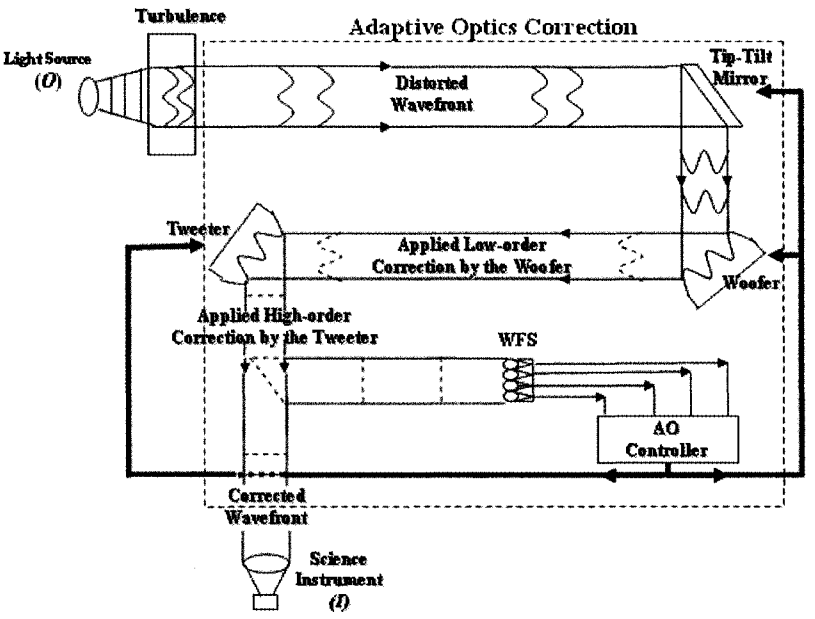


**Figure 2: Working scheme of the UVic W/T AO bench**

The wavefront that leaves the W/T AO system is ideally flat when it strikes the science instrument. The point spread function (PSF) is the response of the optical system to a point source (i.e. the impulse response of the AO system), and the role of the science camera (SC) is to capture images of the corrected long exposure PSF, *I*, gathered during an observation of an object, *O*.

## 4. Adapted Methodology for PSF Reconstruction

The classical method of obtaining a PSF from a single DM AO system is to observe a point source before and after the science exposure to acquire the PSF calibration. There are some drawbacks and limitations to this classical method. Due to long term variation of turbulence characteristics, the determination of an accurate PSF becomes nearly impossible. The PSF observed before or after the exposure may not correspond accurately to the PSF at the time of observation.

An alternative approach for determining the PSF was proposed and implemented by Veran [6, 7] where the reconstruction technique has the advantage of a PSF estimation based on the data measured synchronously with the observation. The PSF estimation can be done, in post-processing stage, by averaging several seconds worth of instantaneous PSF in order to get an estimate of the long-exposure PSF characteristic of the AO system.

In the system modeling and experimental evaluation of PSF reconstruction for a Single DM AO system, Veran's methodology is used. Although the original method was developed using the curvature WFS, in our modeling and experimentation the methodology is applied to SH WFS (Jolissaint [8]).

During an AO correction, the SH WFS will provide a measurement of the phase of the residual wavefront error $\varphi(\vec{r},t)$ at each acquisition. From these measurements the average structure function, $\overline{D}_{\varphi_\varepsilon}(\vec{\rho})$ of this phase can be calculated.

$$\overline{D}_{\varphi_\varepsilon}(\vec{\rho}) = \left\langle \left| \varphi_\varepsilon(\vec{r},t) - \varphi_\varepsilon(\vec{r}+\vec{\rho},t) \right|^2 \right\rangle \quad (4)$$

where vectors $\vec{r}$ and $\vec{\rho}$ represent two dimensional positions and separations in the pupil plane. SH WFS measurements obtained from the long exposure are limited to the DM's spatial cutting frequency; therefore, only the DM component of the phase variations can be measured. The residual phase can be decomposed into two components; $\varphi_P$ the parallel component of the residual phase (phase projected onto the mirror) and $\varphi_O$ the orthogonal component of the phase (residual phase that is not corrected by the mirror).

$$\varphi_{total} = \varphi_P + \varphi_O \quad (5)$$

Note that $\varphi_O$ is not corrected by the system, and it will be estimated from the Kolmogorov model of the turbulence. To reconstruct the PSF from a single DM AO system first the OTF of the system must be computed:

$$OTF_{AO}(\vec{\rho},\lambda) = \exp\left[-\frac{1}{2}\left(D_{\varphi_P}(\vec{\rho}) + D_{\varphi_O}(\vec{\rho})\right)\right] \quad (6)$$

and,

$$OTF_{Total}(\vec{\rho},\lambda) = OTF_{AO}(\vec{\rho},\lambda).OTF_{TEL}(\vec{\rho},\lambda) \quad (7)$$

where $OTF_{TEL}$ is the residual from the AO correction containing the diffraction patterns from the telescope and uncorrected static aberrations and can be calculated as the auto-correlation of the telescope pupil. $OTF_{AO}$ contains the contribution of the turbulence which constantly changes during the observation time, and must be estimated for each science exposure over the observation time for being able to determine the long-exposure PSF. The PSF can then be calculated by taking the inverse Fourier transform of the $OTF_{Total}$.

The structure function of the DM of the parallel and orthogonal component of the residual phase can be expressed as:

$$D_{\varphi_P}(\vec{r},\vec{\rho}) = \left\langle \left| \varphi_P(\vec{r},t) - \varphi_P(\vec{r}+\vec{\rho},t) \right|^2 \right\rangle, \text{and } D_{\varphi_O}(\vec{r},\vec{\rho}) = \left\langle \left| \varphi_O(\vec{r},t) - \varphi_O(\vec{r}+\vec{\rho},t) \right|^2 \right\rangle \quad \textbf{(8)}$$

If one can substitute $\varphi_P(\vec{r},\vec{\rho})$ with its modal decomposition of the mirror modes:

$$\varphi_P(\vec{r},t) = \sum_{i=1}^{N} \varepsilon_i(t) M_i(\vec{r}) \quad \textbf{(9)}$$

where $N$ is the modes of the mirror, the structure function of the DM of the parallel component of the residual phase becomes:

$$D_{\varphi_P}(\vec{\rho}) = \sum_{i=1}^{N}\sum_{j=1}^{N} \left\langle \varepsilon_i \varepsilon_j \right\rangle U_{ij}(\vec{\rho}) \quad \textbf{(10)}$$

where $U_{ij}(\vec{\rho})$ function depends only on the geometry of the system, $P$ the pupil function

$$U_{ij}(\vec{\rho}) = \frac{\int P(\vec{r})P(\vec{r}+\vec{\rho})\left[M_i(\vec{r}) - M_i(\vec{r}+\vec{\rho})\right]\left[M_j(\vec{r}) - M_j(\vec{r}+\vec{\rho})\right] d\vec{r}}{\int P(\vec{r})P(\vec{r}+\vec{\rho}) d\vec{r}} \quad \textbf{(11)}$$

The $<\varepsilon_i\varepsilon_j>$ is the covariance matrix of the mirror modes error commands, updated at each loop cycle, and is related to WFS measurements covariance matrix $<w_iw_j>$ and the aliased orthogonal modes covariance matrix $<\alpha_i\alpha_j>$.

$$\left\langle \varepsilon_i \varepsilon_j \right\rangle = D^+ \left\langle w_i w_j \right\rangle (D^+)^t + \left\langle \alpha_i \alpha_j \right\rangle \quad \textbf{(12)}$$

where $D^+$ is the command matrix gathered from the SH WFS measurements from the mirror modes.The structure function of the orthogonal component of the phase can be calculated numerically using a Monte-Carlo model of the AO system. This can be done by removing the mirror modes out of each phase screen and then computing the average of the structure function for the corrected phase screens, Jolissaint [8].

## 5. Numerical Modelling USING Single DM AO Correction

In order to test the PSF reconstruction theory from the instantaneous SH WFS slopes, a numerical model for PSF reconstruction has been performed to establish a baseline for future experimentations. The end-to-end model is entirely coded with Matlab using object-oriented programming. The object-oriented architecture makes the model fully modular and easily extendable. In the model, the simulation of atmospheric turbulence is introduced by the phase screens.

The inputs for the reconstruction of the PSF from the system modeling can be summarized as: (i) the residual wavefront error data from the synchronous SH WFS measurements, (ii) the command matrix of the control loop, and (iii) the system's geometry. The computed parameters are: (i) the commands projected onto the mirror modes, (ii) the parallel and orthogonal structure function of the atmospheric turbulence, (iii) the covariance matrix of the WFS, and (iv) the OTF of the telescope.

### 5.1 Numerical Modeling Results

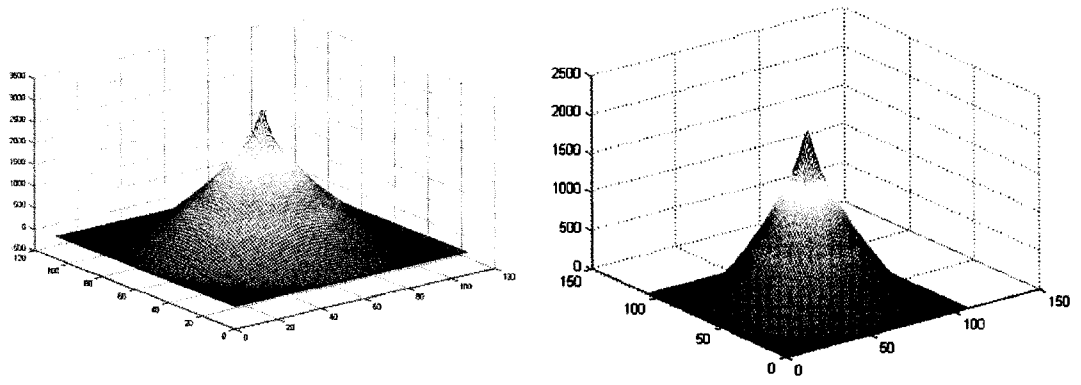


**Figure 3: a) The OTF obtained after AO correction, b) The reconstructed OTF**

In the Figure 3, the good agreement from the OTF obtained from the SC (a) of the numerical model and the OTF calculated from the SH WFS data of the system (b) are shown in a 3-D plot.

The plot (Figure 4) represents a single one-dimensional cut through the OTFs shown above. The plot represents also a symmetrical cut to be able to distinguish the discrepancies between the OTF of the telescope, OTF from the SC of the system model, and the OTF reconstructed.

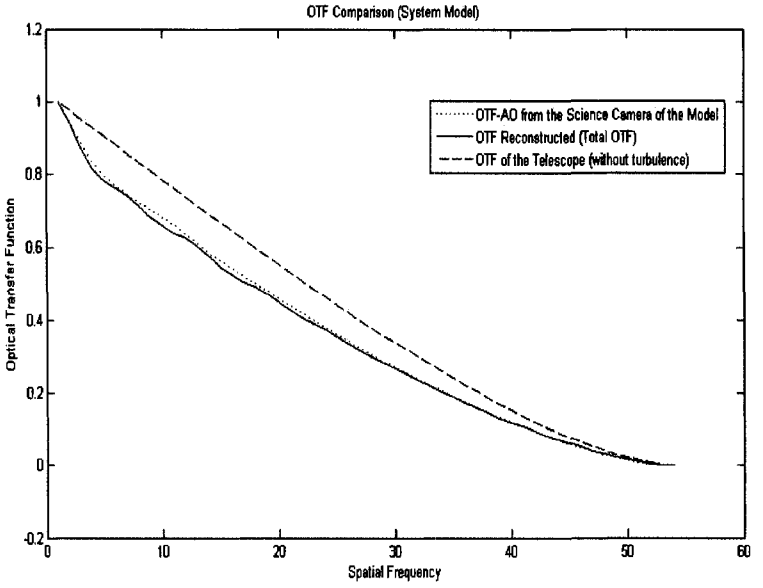


**Figure 4: Reconstructed OTFs (Numerical)**

In Figure 4, the comparisons between the numerical OTFs are represented. The dashed line represents the OTF of the telescope itself in absence of turbulence. The dotted line is the $OTF_{AO}$ after the AO correction which is gathered from the SC of the system. The continuous line represents the OTF calculation from the synchronous SH WFS data of the slopes obtained from the model multiplied by the $OTF_{TEL}$, and it is calculated using the

parallel and orthogonal component of the phase. Given that the continuous line is the total reconstructed OTF and that the dotted line is the $OTF_{AO}$, the good agreement between the OTF calculated and the OTF obtained from the AO correction can be clearly seen.

It must be added that these preliminary results (Figure 3, 4) do not include the aliasing error calculation. These modeling results ensured the successful OTF reconstruction from the modeling, by the correct implementation of the methodology.

## 6. Experimentation USING Single DM AO Correction

We decided to use UVic Dual DM AO bench (see Figure 5) to validate the numerical model. A hot air turbulence generator is placed between the artificial source and the pupil, which is capable of creating the optical effects of the atmospheric turbulence, Keskin [3, 4, 5].

The data to be used in the PSF reconstruction process is collected by the SH WFS of the experimental bench (in closed-loop). Due to the registration and alignment issues of the Tweeter, the experimentation consists of the Woofer low-order-high-stroke DM results.

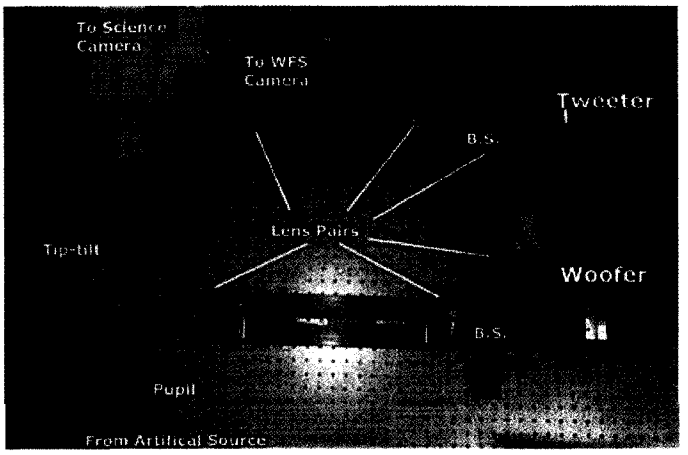


**Figure 5: UVic Woofer-Tweeter AO Bench**

The Science Camera of the system was not operational at the time of data collection. One solution was to introduce the same characteristics of the atmospheric turbulence (created by the hot air turbulence generator) into the system model (as phase screens). The SC of the system model is therefore used to compare the experimentally reconstructed OTF to the OTF after AO correction.

## 6.1 Experimental Results

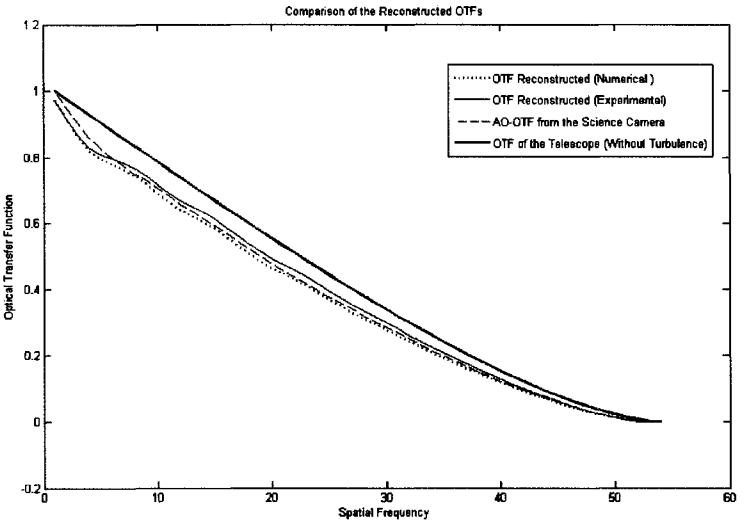


**Figure 6: Reconstructed OTFs (Experimental)**

In Figure 6, the comparisons between the numerical and experimental OTFs are represented. The continuous line on top represents the OTF of the telescope itself in absence of turbulence. The dashed line is the $OTF_{AO}$ after the AO correction which is gathered from the SC of the numerical model. The continuous line represents the OTF experimental calculated from the synchronous SH WFS data of the slopes (in closed-loop) multiplied by the $OTF_{TEL}$, and it is calculated using the parallel and orthogonal component of the phase. The dotted line is the OTF numerical reconstructed from the SH WFS data of the slopes of the system model (in closed-loop). The good agreement between the OTF calculated (both numerical and experimental) and the OTF obtained from the AO correction can be clearly seen. The experimental results proved the successful OTF reconstruction using a correct implementation of the methodology.

## 7. Conclusions

The software, the controllers and the opto-mechanical components of the W/T AO system have been integrated in the experimental test bench, and the loop has been successfully closed. Further tests are on going for the characterization of the system, for the alignment of the Tweeter, for the integration of the science camera, and for the demonstration of the closed-loop wavefront control feasibility of the W/T AO concept. The PSF reconstruction from the system model is a close match to the real system's and evidence of this is shown by the good agreement in the Figure 7.

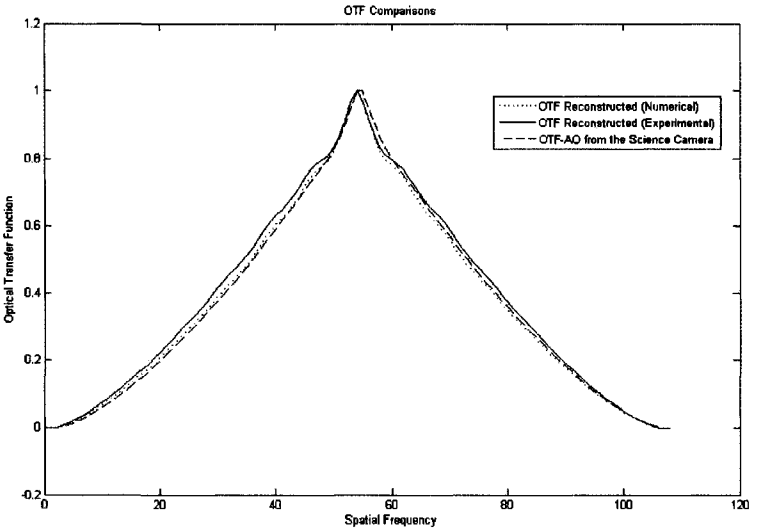


**Figure 7: OTF comparisons (Numerical / Experimental)**

## Future Work

The science camera will be integrated into the bench and the closed-loop OTF-AO will be experimentally gathered. The discrepancy between the OTF reconstructed experimentally and the OTF obtained from the science camera will be examined, and aliasing error will be observed. The accomplishments of the implementation will lead to the establishment of baseline theoretical and experimental performance. This knowledge will be used to propose a new technique for reconstructing the PSF from a Multi-Conjugated Adaptive Optics (MCAO) architecture, which will be performed both by numerical modeling and by experimentation.

## Acknowledgments

The authors would like to thank the support of the University of Victoria, Herzberg Institute of Astrophysics NRC-CNRC (National Research Council of Canada) for their technical support and collaboration.

## References

1. G. Herriot, P. Hickson, B.L. Ellerbroek, D.A. Endersen, T. Davidge, D.A. Erickson, I.P. Powell, R. Clare, M. Smith, L. Saddlemyer, J.P. Veran, "NFIRAOS: TMT facility adaptive optics with conventional DMs", SPIE proceedings 5903, 2004.

2. R. Dekany, M. Britton, D. Gavel. B. Ellerbroek, G. Herriot, C. Max, J.P. Veran, "Adaptive optics requirements definition for TMT", SPIE proceedings 5490, 879-890, 2004.

3. O. Keskin, L. Jolissaint, C. Bradley, S. Dost, I. Sharf *"Hot Air Turbulence Generator for Multi-Conjugate Adaptive Optics"*, Proceedings of SPIE, Volume 5162, 49-57, 2003.

4. L. Jolissaint, O. Keskin, C. Bradley, B. Wallace, A. Hilton *"Multiple-Layer Optical Turbulence Generator Principle and SLODAR Characterization: Preliminary Results,"* Proceedings of SPIE, Volume 5572, 256-261, 2004.

5. O. Keskin, L. Jolissaint, C. Bradley *"A Hot Air Turbulence Generator for Adaptive Optics: Applications, Principles, and SLODAR Characterization"* Applied Optics (received/accepted), 2006

6. J.P. Veran, F.Rigaut, H. Maiter, and D. Rouan, "Estimation of the adaptive optics long exposure point spread function using control loop data," J. Opt. Soc. Am. A, 14, 1997.

7. J.P Veran, "Estimation de la reponse impulsionelle et restauration d'image en optiique adaptative: Application au system d'optique adaptative du telescope Canada-France-Hawaii," Ecole National Superieure des Telecommunications, Thesis, 1997.

8. L. Jolissaint and J.P.Veran, "Fast computation and morphologic interpretation of the adaptive optics point spread function," Beyond Conventional Adaptive Optics, ESO Conference and Workshop Proceedings 58, pp. 201, 2002.

---

Send correspondence to Onur Keskin

E-mail: okeskin@me.uvic.ca, Telephone: +1 (250) 721-8624

# Appendix C:

## *Derivation and experimental evaluation of a point spread function reconstruction from a dual deformable mirror adaptive optics system*

**Optical Engineering**

**Accepted / to be Published (2007)**

# Derivation and Experimental Evaluation of a Point Spread Function Reconstruction from a Dual Deformable Mirror Adaptive Optics System

**O. Keskin[1], R. Conan[1], P. Hampton [2], C. Bradley[1]**

*University of Victoria, Adaptive Optics Laboratory, Engineering Lab Wing B 133,*

*PO Box 3055 STN CSC, Victoria, BC, Canada, V8W 3P6,*

*Phone: +1 (250) 721 8624*

*Fax: +1 (250) &21 6500*

*[1]Department of Mechanical Engineering*

*[2]Department of Electrical and Computer Engineering*

*okeskin@me.uvic.ca, rconan@uvic.ca, phampton@engr.uvic.ca, cbr@me.uvic.ca*

**Keywords:** Adaptive Optics, Point Spread Functions

**Abstract:** This paper presents the derivation, implementation and testing of an improved Point Spread Function (PSF) reconstruction technique for the University of Victoria's dual Deformable Mirror (DM) Woofer-Tweeter (W/T) Adaptive Optics (AO) system. The methodology has been tested on numerical models and implemented on an experimental dual DM AO system. The methodology is based on the data saved by the AO system during the science exposure. This data is later used in the post-processing stage to reconstruct the PSF. Although the results are unique to the UVic W/T AO bench, the proposed PSF reconstruction methodology will be applicable to other dual DM systems and to multi DM AO systems.

## 1. Introduction

In AO applications, PSF reconstruction is used in calibrating image analysis techniques for astrometry and in the deconvolution of images to enhance their contrast. The partial correction provided by the AO systems is due to the finite sampling of the wavefront sensor (WFS), the DM and the finite bandwidth of the overall system. Furthermore, the correction provided by an AO system degrades across the field of view depending on the angular separation between the guide stars and the target object. This partial correction is due to the high spatial frequencies introduced by the atmospheric turbulence, which translates into a halo artifact on the PSF. Consequently, the dimmer details of the AO image may not be detectable. One possible way to counteract the halo effect is through PSF reconstruction. In order to achieve accurate results, the analysis of the corrected images must account for the PSF temporal variation. Unfortunately, calibrating the PSF with pre and/or post observation of bright stars across the field does not give reliable results due to the temporal variability of the seeing. Therefore, the PSF calibration must be done during the AO exposure itself. Reconstructing the PSF from wavefront sensor data is the most promising and reliable technique to achieve this objective.

Only one PSF reconstruction tool has been implemented for operational use on an astronomical telescope: Veran's [1,2] code for the Canada-France-Hawaii Telescope (CFHT) Adaptive Optics Bonnette (also called PUEO). Although the original method was developed using the curvature WFS, the algorithm was later adapted and applied to Shack Hartmann WFS (SH WFS) [3,4,5,6]. In the W/T AO Bench, the methodology is also applied to SH WFS [7].

The RMS amplitude of turbulence-induced wavefront distortions increases with the five-sixths power of the telescope aperture diameter $D$ [8], while at the same time the number of DM degrees of freedom required to compensate the distortions to any given level of correction is growing as $D^2$. Extremely Large Telescopes (ELTs) will have primary mirror diameters that are at least 3 times larger than the current major optical telescopes. This would require DMs with at least 2.5 times greater stroke and 9 times the number of actuators to achieve equivalent correction comparable to current AO systems. It appears that, due to the unavailability of a manufacturing technology for such a DM, it will not be possible to satisfy both of these requirements for the ELTs with a single high-order-high-stroke DM. The power spectrum of the atmospheric turbulence follows a decaying ($f^{-11/3}$) power law [9]. Therefore, most of the turbulence energy is concentrated at low spatial frequencies and requires large stroke for correcting the first modes of the atmospheric turbulence; whereas at high spatial frequencies, the stroke requirement for the AO correction drops substantially. A solution to this problem is the use of dual DMs; the so called W/T configuration. In W/T architecture, the Woofer (WR) is a low-order-high-stroke DM used to compensate for the low-frequency effects introduced by the atmospheric turbulence. The Tweeter (TR) is a high-order-low-stroke DM used to compensate for the high-frequency effects. Having dual DMs allows the W/T AO system to have a high degree of correction of large amplitude wavefront distortion. Therefore, an improved PSF reconstruction methodology has been developed for the W/T AO architecture.

In Section 2, original and current PSF reconstruction techniques for single DM AO systems are investigated and improvements to the methodology are demonstrated in order

to accommodate PSF reconstruction for an AO system with separate tip/tilt mirror (TT), WR and TR architecture. Therefore, this PSF reconstruction technique is applied to a system with 3 distinct mirrors. Numerical modeling of a W/T AO system has been performed and these PSF reconstruction results are presented in Section 3. The PSFs reconstructed from the W/T experimental bench were compared to the PSFs recorded by the Science Camera (SC) of the real system. This comparison is presented in Section 4. The outcome of this research is significant for the performance characterization and improvement of the next generation AO systems. Although the results are unique to the UVic W/T AO bench, the proposed PSF reconstruction methodology will be applicable to other multi DM AO systems. Therefore, this paper consists of the improvement of the current PSF reconstruction technique progressing from a single DM AO system to a dual DM AO system, and furthermore to N DMs. In that sense, the availability of UVic AO laboratory dual DM bench offers a unique opportunity to validate the theoretical methods on real hardware.

## 2. Point Spread Function

The focal plane of the SC can be considered as the image plane and its position coordinates is $\vec{\alpha}$. The object plane, $\vec{\beta}$, is considered to be at an infinite distance from the image plane. These planes, $\vec{\alpha}$ and $\vec{\beta}$, are orthogonal to the optical axis.

The intensity distribution of the object across the object plane is $O(\vec{\beta})$. Similarly the intensity distribution of the long exposure image measured on the SC is $I(\vec{\alpha})$. This can be represented by a Fredholm integral equation, and the formation of an image through an AO system can then be defined as

$$I(\vec{\alpha}) = \int O(\vec{\beta})\, PSF(\vec{\alpha}, \vec{\beta})\, d\vec{\beta} \quad \textbf{(1)}$$

The PSF of the point source represents the intensity received at the point $\vec{\alpha}$ of the image plane when the point-like object's intensity at position $\vec{\beta}$ is observed.

The isoplanatic patch is the area where the distortion level of the atmospheric turbulence is statistically the same everywhere in the field. It is generally assumed that the long exposure PSF has the same shape regardless of the viewing direction within this isoplanatic patch. The stationary $PSF(\vec{\alpha}, \vec{\beta})$ can then be described as $PSF(\vec{\alpha} - \vec{\beta})$ [2]. Equation 1 can then be rewritten as a convolution

$$I(\vec{\alpha}) = \int O(\vec{\beta})\, PSF(\vec{\alpha} - \vec{\beta})\, d\vec{\beta} = O(\vec{\alpha}) \otimes PSF(\vec{\alpha}) \quad \textbf{(2)}$$

In the Fourier domain, this convolution becomes a product

$$\tilde{I}(\vec{f}) = \tilde{O}(\vec{f}) \;.\; OTF(\vec{f}) \quad \textbf{(3)}$$

The relation between the AO system imaging performance and the characterization of the residual error using the PSF of the AO correction will be described in the following sections.

### 2.1 Imaging through an AO system

To improve the final AO images, the PSF is estimated in the post-processing stage. This uses the residual wavefront error data measured by the WFS and the mirror commands of the multi-DM AO system (Figure 1). Once the PSF is known, the object can be partially rebuilt up to the spatial cut-off frequency of the telescope through a deconvolution process.

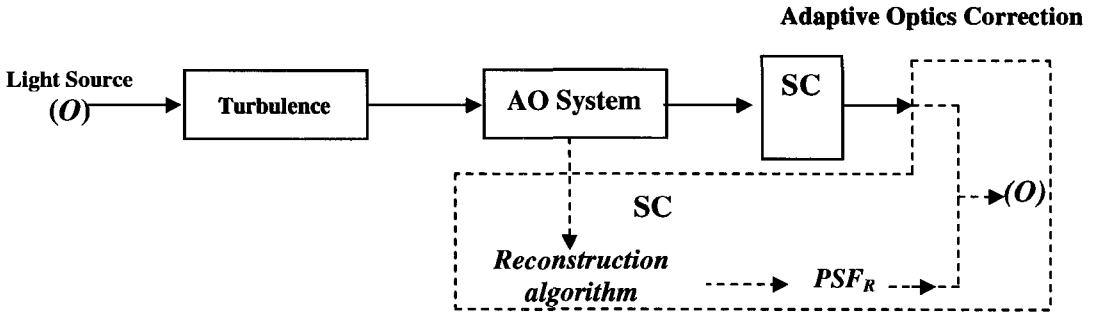


**Figure 1: Imaging through an AO system and schematically representation of the PSF reconstruction process (dashed lines represents operations in the post-processing stage)**

## 2.2 Methodology

The classical method of obtaining a PSF from a single DM AO system is to observe a point source before and after the science exposure (e.g. an image gathered at the science camera) to acquire the PSF calibration. There are some drawbacks and limitations to this classical method. Due to long term variation of turbulence characteristics, the determination of an accurate PSF becomes nearly impossible. The PSF observed before or after the exposure may not correspond accurately to the PSF at the time of observation.

An alternative approach for determining the PSF was proposed and implemented by Veran [2] where the reconstruction technique has the advantage of a PSF estimation based on the data measured synchronously with the observation. The PSF estimation can be done, in post-processing stage, by averaging several seconds worth of instantaneous PSFs in order to get an estimate of the long-exposure PSF characteristic of the AO system.

The system optical transfer function ($OTF_{Total}$) is the product of AO system OTF and telescope OTF, as given in Equation 4. It is assumed that the OTF is stationary over the pupil; and is not dependent on the direction of the observation; and is dependent on the separation $\rho$

$$OTF(\vec{\rho},\lambda)_{Total} = OTF(\vec{\rho},\lambda)_{AO}.OTF(\vec{\rho},\lambda)_{TEL} \quad \textbf{(4)}$$

The $OTF_{TEL}$ is ideally the auto-correlation of the telescopes pupil, but in practice it also contains the effects of uncorrected static aberrations of the telescope. $OTF_{AO}$ is the OTF of the sum of the phase of the turbulent atmosphere and of the DM shapes. The phase of the turbulent atmosphere is a function of time. The DM shape opposes the turbulent phase which results in a residual phase that is also a function of time. This residual turbulence must be estimated for each sample of the AO system in order to be able to determine the long exposure PSF.

The WFS measurements *(w)* determine the residual phase, $\varphi_{tot}$. The residual phase can then be decomposed into two components: (i) $\varphi_P$, parallel component which contains low frequency component up to the DMs cut-off frequency, and (ii) $\varphi_O$, orthogonal component which is composed of the high spatial frequency that is beyond the spatial cut-off frequency of the DM.

$$\varphi_{tot} = \varphi_P + \varphi_O \quad \textbf{(5)}$$

Note that $\varphi_P$ and $\varphi_O$ are orthogonal to each other, and $\varphi_O$ will be estimated from the Kolmogorov model of the turbulence since the spatial frequencies of $\varphi_O$ is beyond the WFS cut-off frequency.

### 2.2.1 Estimation of the $\varphi_P$

As an improvement to Veran's approach, in the TT + WR + TR architecture, $\varphi_P$ can be given by

$$\varphi_P(\vec{r},t) = \sum_{i=1}^{N_{TT\ mirror}} \varepsilon_i(t) M_{i\,tt\ mirror}(\vec{r}) + \sum_{i=1}^{N_{woofer}} \varepsilon_i(t) M_{i\,woofer}(\vec{r}) + \sum_{i=1}^{N_{tweeter}} \varepsilon_i(t) M_{i\,tweeter}(\vec{r}) \quad \textbf{(6)}$$

Where $M$ is influence functions of the mirrors in DM vector space, *and* $\varepsilon$ are the mirrors residual phase coefficients.

$$\varepsilon(t) = D^{+}w(t) \tag{7}$$

$D^{+}$ is the command matrix for the W/T system deduced from the pseudo-inverse of the interaction matrix $D$.

When all the mirrors are running together, the DM vector space, $M_{itotal}$, can be expressed as the concatenation of vectors

$$M_{i_{total}} = \left[ M_{i_{tt\ mirror}} \quad M_{i_{woofer}} \quad M_{i_{tweeter}} \right] \tag{8}$$

and $N_{total}$ (number of modes) becomes, it must also be noted that TT, WR, and TR modes are orthogonal to each other

$$N_{total} = N_{TTmirror} + N_{woofer} + N_{tweeter} \tag{9}$$

and Equation 6 can be simplified to

$$\varphi_P(\vec{r},t) = \sum_{i=1}^{N_{total}} \varepsilon_i(t) M_{i\,total}(\vec{r}) \tag{10}$$

The parallel structure function of the residual phase is given by

$$D_{\varphi_P}(\vec{r},\vec{\rho}) = \left\langle \left| \varphi_P(\vec{r},t) - \varphi_P(\vec{r}+\vec{\rho},t) \right|^2 \right\rangle \tag{11}$$

The structure function of the parallel component of the phase can then be represented as

$$D_{\varphi_P}(\vec{r},\vec{\rho}) = \sum_{i=1}^{N_{total}} \sum_{j=1}^{N_{total}} \left\langle \varepsilon_i \varepsilon_j \right\rangle \left[ M_{i_{total}}(\vec{r}) - M_{i_{total}}(\vec{r}+\vec{\rho}) \right] \left[ M_{j_{total}}(\vec{r}) - M_{j_{total}}(\vec{r}+\vec{\rho}) \right] \tag{12}$$

and the pupil average structure function of the parallel components becomes

$$\overline{D}_{\varphi_P}(\rho) = \left\langle \frac{\iint_P P(r)P(r+\rho) D_{\varphi_P}(\vec{r},\vec{\rho}) dr}{\iint_P P(r)P(r+\rho) dr} \right\rangle \tag{13}$$

This can be rewritten in a simpler form

$$\bar{D}_{\varphi_P}(\vec{\rho}) = \sum_{i=1}^{N_{total}} \sum_{j=1}^{N_{total}} \left\langle \varepsilon_i \varepsilon_j \right\rangle \; U_{ij}(\vec{\rho}) \tag{14}$$

Where $<\varepsilon_i\varepsilon_j>$ is the covariance matrix of the WR and TR mirror mode error commands. This is updated at each loop cycle.

$$\left\langle \varepsilon_i \varepsilon_j \right\rangle = D^{+} \left\langle w_i w_j \right\rangle (D^{+})' \tag{15}$$

$<\varepsilon_i\varepsilon_j>$ is also related to SH WFS measurement covariance matrix $<w_iw_j>$. The definition of $U_{ij}(\rho)$ can be found in the next section.

### 2.2.2 The $U_{ij}(\rho)$ functions

$U_{ij}(\vec{\rho})$ is the cross-correlation of the DM modes, and can be represented as:

$$U_{ij}(\vec{\rho}) = \frac{\int P(\vec{r}) P(\vec{r}+\vec{\rho}) \left[ M_{i_{total}}(\vec{r}) - M_{i_{total}}(\vec{r}+\vec{\rho}) \right] \left[ M_{j_{total}}(\vec{r}) - M_{j\,total}(\vec{r}+\vec{\rho}) \right] d\vec{r}}{\int P(\vec{r}) P(\vec{r}+\vec{\rho}) d\vec{r}} \tag{16}$$

where $P(r)$ is the pupil function. The calculation of $U_{ij}(\rho)$ utilizes the Fourier transforms and the properties of the correlation function:

$$U_{ij}(\vec{\rho}) = \frac{F^{-1}\left\{ 2\,\mathrm{Re}\,al\left[ F(M_i M_j P) F^{*}(P) - F(M_i P) F(M_j P) \right] \right\}}{F^{-1}\left( \left| F(P) \right|^2 \right)} \tag{17}$$

In Equation 17, $F$ is the Fourier transform operator and * represents the complex conjugate. It must be noted that the calculation of $U_{ij}$ is computationally long but it is calculated once depending on the system's geometry.

### 2.2.3 Calculation of $\varphi_O$

The structure function of the orthogonal component of the phase can be computed either numerical or analytical [5] methods. Here it is computed numerically using a Monte-Carlo model to generate phase screens; remove the mirror modes ($M_{itotal}$) out of each phase screen; and then compute the average of the structure function for the corrected phase screens.

The orthogonal structure function of the residual phase is given by

$$D_{\varphi_o}(\vec{r},\vec{\rho}) = \left\langle \left| \varphi_O(\vec{r},t) - \varphi_O(\vec{r}+\vec{\rho},t) \right|^2 \right\rangle \tag{18}$$

and its pupil average can be derived similarly

$$\bar{D}_{\varphi_o}(\rho) = \left\langle \frac{\iint_P P(r)P(r+\rho)D(\vec{r},\vec{\rho})dr}{\iint_P P(r)P(r+\rho)dr} \right\rangle \tag{19}$$

### 2.2.4 The remaining error calculations

The propagation of the WFS measurements error onto the mirror modes originates from the turbulent phase having a high order component which gives a non-zero measurement on the WFS, and is mistaken for a low order component through the estimation process. It depends on the statistics of $\varphi_o$ and can be derived from the WFS measurements. $\varphi_o$ is not corrected by the AO system, it can be assumed to be in good agreement with the Kolmogorov atmospheric turbulence model, and it is computed from the model. This error is a consequence of the finite spatial sampling of the WFS and it has been shown to be the combination of two effects [10], namely spatial aliasing and spatial cross-coupling. We will refer to it as the remaining error, $\varepsilon_r(t)$:

$$\varepsilon_r(t) = D^+ w(\varphi_o(r,t)) \tag{20}$$

and the covariance matrix of the remaining error, $C_{rr}$ is calculated from the numerical model, and can be given as:

$$C_{rr} = \left\langle \varepsilon_r \varepsilon_r^t \right\rangle \tag{21}$$

Equation 13 then can be replaced by:

$$\left\langle \varepsilon_i \varepsilon_j \right\rangle = D^+ \left\langle w_i w_j \right\rangle (D^+)^t + C_{rr} \tag{22}$$

To account for the remaining error, $\varepsilon_r(t)$, and its effect on the PSF reconstruction process, one can use Equation 22 instead of Equation 13 and then calculate the parallel component of the residual phase accordingly. Note that $C_{rr}$ is also calculated from the model.

### 2.3 OTF reconstruction

The $OTF_{TEL}$ is ideally the auto-correlation of the telescope's pupil, but in practice it also contains the effects of uncorrected static aberrations of the telescope. The long exposure atmospheric $OTF_{AO}$ can then be expressed as a function of the second order statistical moment of the residual phase: Equation 23 presents this in terms of the structure function of the parallel and orthogonal residual phase:

$$OTF(\vec{\rho},\lambda)_{AO} = \exp\left[-\frac{1}{2}\left(D_{\varphi_r}(\vec{\rho}) + D_{\varphi_o}(\vec{\rho})\right)\right] \tag{23}$$

By replacing $OTF_{AO}$ in Equation 4, the $OTF(\vec{\rho},\lambda)_{Total}$ can be calculated.

The determination of the OTF also leads to the determination of the estimated long exposure PSF via a single discrete Fourier Transform.

### 3. Working Principle of the Woofer/Tweeter (W/T) AO System

The principle of operation of the UVic W/T AO system is illustrated in Figure 2. A planar wavefront, generated by a collimated point light source, goes through the hot-air atmospheric turbulence generator [11] and becomes aberrated. Using a hot-air atmospheric turbulence generator is an alternative to other techniques in simulating the optical effect of atmospheric turbulence, (e.g. etched rotating phase screens that are expensive to manufacture and do not allow turbulence strength adjustment). This limitation prevents real-time assessment of AO control system performance versus turbulence strength and particularly high-$\sigma$ events (e.g. sudden bursts of turbulence). The degree of distortion of the wavefront is detected by the SH WFS. The purpose of the W/T AO system is to make this distorted wavefront as flat as possible. TT mirror is a flat mirror which adjusts the tip/tilt position offsets of the incoming distorted wavefront by counteracting the apparent motion of the star. Both DMs use a grid of actuators to deform their physical shape to an opposing shape of the distorted wavefront. In the wavefront compensation process, the commands of both WR and TR and also the command of the TT mirror are determined by the AO controller (in closed loop), which uses the SH WFS measurements. During this closed loop operation the WFS measures only the residual wavefront error reflected onto the DMs and the TT mirror (i.e. the uncorrected phase distortions of the wavefront). This process takes place in real-time to compensate for the constantly changing optical effects of the atmospheric turbulence.

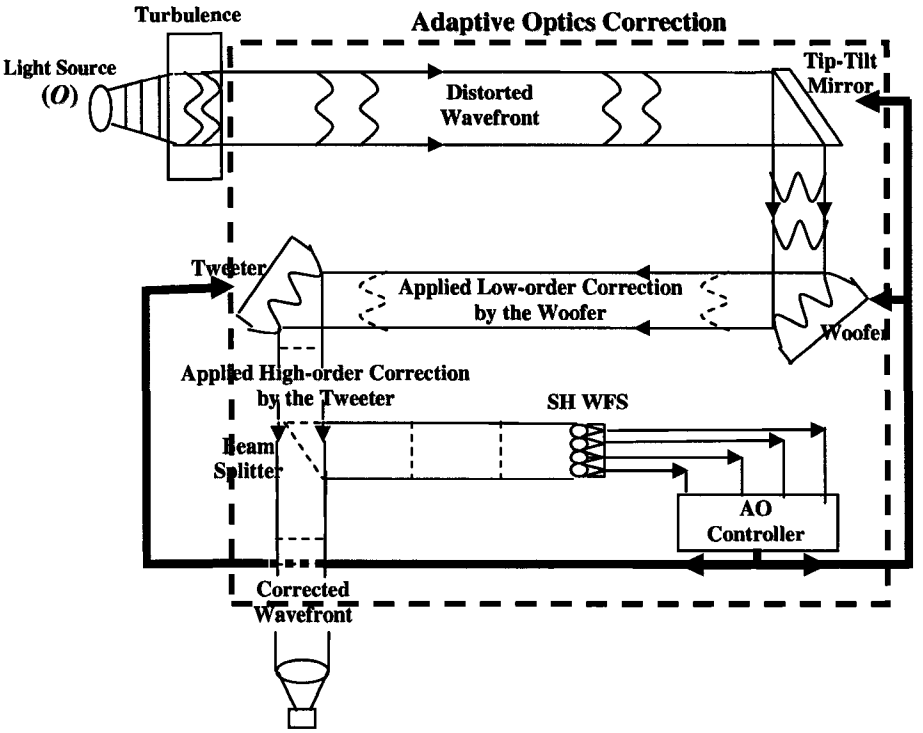


**Figure 2: Working Scheme of the W/T AO Bench (dashed lines represent AO correction)**

The wavefront that leaves the AO system is ideally flat when it strikes the science instrument. The science instrument can be a camera, spectrograph, coronagraph, or an interferometer. For AO system commissioning and PSF reconstruction verification, at the UVic AO bench, a camera is chosen as the science instrument. The role of the science camera (SC) is to capture images of the corrected long exposure PSF, *I*, gathered during an observation of the point source, *O*.

### 3.1 Experimental set-up

The UVic experimental W/T AO system is composed of seven main components (see Figure 2): light source, hot air turbulence generator, TT mirror, low-order-high-stroke WR, high-order-low-stroke TR, Shack Hartmann WFS, and SC. In addition to these

components, optical elements are used to magnify, conjugate, and focus the light beam. The optical effects of atmospheric turbulence are generated by the hot-air turbulence generator built, and characterized [11] at the Uvic AO Laboratory which can generate $D/r_0$ values up to $\approx 42$. The tip-tilt mirror is manufactured by Mad City Labs. It has a scanning frequency of 1kHz, a motion range of 2-5 milli-radian and a resolution of 4 nano-radian. On top of the stage, a 35mm diameter mirror has been bonded. The WR mirror is a magnetic mirror manufactured by ALPAO [12,13]. It is a low-order-high-stroke DM that is used to compensate for the low-order aberrations introduced by the turbulence generators. The Woofer provides 25μm of maximum stroke and contains 52 actuators in the pupil (8x8). The TR mirror is a Mirco Electro Mechanical Systems (MEMS) mirror manufactured by Boston Micromachines. It is a high-order-low-stroke DM that is used to compensate for the high-order aberrations introduced by the turbulence generators. As maximum stroke the Tweeter provides 1.2μm and it contains 144 (12x12) actuators. The edge actuators are discarded and only the 10X10 central array is employed. The Shack-Hartmann WFS (SH-WFS) uses a lenslet array manufactured by Adaptive Optics Associates Inc. It is made of 132x132 square lenslets with a pitch of 188μm and 8mm focal length. A subset of 9x9 lenslets is used to match the 10x10 tweeter actuators according to the Fried Geometry [14], and the TR mirror actuators are registered to the vertices of these lenslets.

Influence functions are a map of the physical deformations in the DM surface after applying a voltage to a given actuator. Modal basis are orthogonal to a given set of modes that restrict the DM correction to a spatial frequency domain. The methods used to derive each DM modal basis are based on the influence function of each DMs. The modal basis

has been tested on the W/T AO test bench and it has been shown that the rms amplitude of the WR DM and TR DM stroke can be reduced by a factor of 3 and 9 respectively when making the transition from a zonal-driven closed-loop to a modal-driven closed-loop with the same performance in both cases [15].

### 3.2 Numerical Modeling Results

In order to validate the PSF reconstruction method, numerical modeling is performed. The end-to-end model is entirely coded with Matlab using object-oriented programming, and it is comprised of the models of the optical elements of the W/T AO bench [16]. Atmospheric turbulence is introduced by phase screens generated using a Monte Carlo model at 1000 iterations. The parameters used in the simulation are: telescope diameter of 10m; a $D/r_0$ of 8; and sampling is 108.

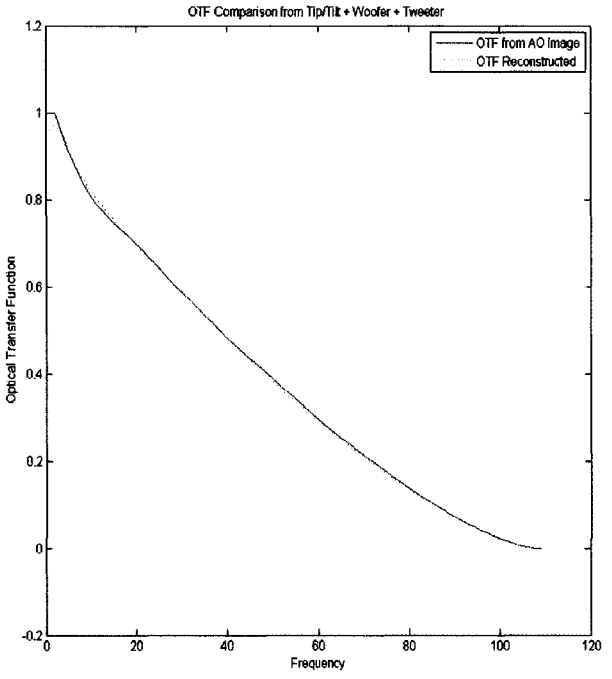


**Figure 3: Numerical Modeling OTF Reconstruction Results**

The agreement between the single dimensional cuts of the OTF obtained from the AO corrected image and the OTF reconstructed from the SH WFS data (Fig.3) ensured that a successful reconstruction was achieved through the correct implementation of the improved methodology.

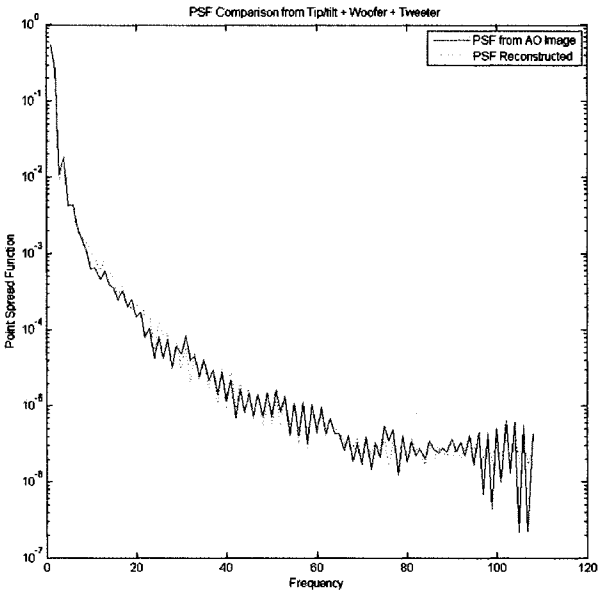


**Figure 4: Numerical Modeling PSF Reconstruction Results**

From the real and estimated long exposure OTFs, the long exposure real and reconstructed PSFs are obtained indirectly via a single discrete Fourier Transform (Fig. 4). In these results, the WFS and aliasing error are taken into account and the good agreement on both comparisons between reconstructed and gathered OTFs and PSFs lead to the establishment of an experimental evaluation.

It must also be noted that, for a better comparison, both real and reconstructed OTF and PSF plots are scaled so that the maximums of the real OTF and PSF are 1. The parameters used in the simulation are chosen to be compatible with today's telescopes.

## 4. Experimental Evaluation

The theory is also validated by experimental evaluation, the simulation results ensured the successful reconstruction of the PSF. It must also be noted that once the telescope's diameter gets larger the $D/r_0$ ratio becomes the defining factor, given that the atmospheric turbulence Fried ($r_0$) parameters can be adjusted on the hot-air turbulence generator [11], for a given experimental setup $D/r_0$ values up to 36 are reproduced while keeping the entrance pupil D constant. In the W/T architecture, the TR mirror is designed with sufficient spatial and temporal control bandwidth to compensate for the turbulence-induced phase distortion to the desired level of correction, but without sufficient stroke to correct the full amplitude of the expected errors. Large amplitude errors are offloaded to the WR mirror, which has many fewer actuators but much greater stroke.

The concept is in some ways a generalization of the interaction between AO and active control systems in telescopes, where a few low-order Zernike modes are offloaded to the secondary and primary mirrors. The differences are: (i) the number of modes to be shared between the mirrors is much higher, and (ii) the WR mirror compensates for a significant fraction of turbulence-induced wavefront errors.

### 4.1 Angle of Arrival method for determining the Fried parameter

In order to account for the high frequency component of the atmospheric turbulence generated by the well characterized [11] hot-air atmospheric turbulence generator, Fried parameter [17,18] values have been extracted using the angle of arrival method.

The Angle of Arrival (AoA) is defined as the mean slope of the turbulent wavefront *W(x,y)* into the pupil *P(x,y)* of the telescope, or the exit pupil of the turbulator in this experiment:

$$\alpha_P = \frac{X_C}{F_L} = \frac{\iint P(x,y)\frac{\partial W}{\partial x}(x,y)dxdy}{\iint P(x,y)dxdy} \quad \textbf{(24)}$$

where $F_L$ is the focal length, and $X_C$ is the x-coordinate of the image centroid.

Equation 22 is given for the *x-coordinate* on the focal plane. The relation for *y-coordinate* is the same as *x-coordinate* and obtained by derivation versus *y* instead.

In the general case of a limited flow, the AoA variance is given, for a turbulent layer of thickness $\delta h$, by [19]:

$$\sigma^2_{AoA}[x,y] = (2\pi)^{4/3} 0.033 C_N^2 \delta h \iint_{R^2} f_{X,Y}^2 (f^2 + L_0^{-2})^{-11/6} e^{-l_0^2 f^2} \left[\frac{2J_1(\pi D f)}{\pi D f}\right]^2 df_X df_Y \quad \textbf{(25)}$$

Only in the infinite scale Kolmogorov regime ($L_0 = \infty$ *and* $l_0 = 0$), this equation has an analytic solution:

$$\sigma^2_{AoA}[x,y] = 2.8375 C_N^2 \delta h D^{-1/3} = 0.1698(\lambda/D)^2 (D/r_0)^{5/3} \quad \textbf{(26)}$$

After extracting the $r_0$ values, the structure function of the orthogonal component of the phase is done by numerically using a Monte-Carlo model to generate phase screens containing the same $r_0$ values and Kolmogorov statistics [20], and removing the mirror modes out of each phase screen and then computing the average of the structure function (Section 2.2) for the residual (high spatial frequency) phase screens.

## 4.2 Experimental Results

In the graphs below, the OTF and PSF comparisons can be seen for a turbulence regime of $D/r_0 \approx 26\text{-}36$. The good agreement between the single dimensional cuts of the azimuthally averaged OTFs obtained from the AO corrected image and the OTFs reconstructed from the SH WFS data. These results ensured that a successful OTF reconstruction was achieved through the correct implementation of the methodology. From the estimated long exposure OTFs, the PSFs are obtained indirectly via a single discrete Fourier Transform for corresponding parameters and compared to the ones gathered from the SC of the system.

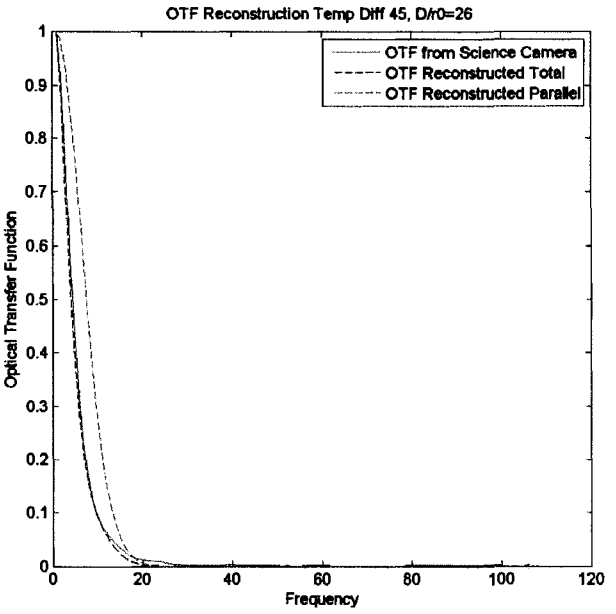


**Figure 5: Experimental OTF Reconstruction Results from the W/T Bench at $D/r_0 = 26$**

Fig.5 is the OTF comparison at Temp Diff 45°C and at $D/r_0=26$ and a Strehl ratio of %63, The good agreement between the single dimensional cuts of the azimuthally averaged OTFs obtained from the AO corrected image. From the estimated long exposure

OTFs, the azimuthally averaged PSFs are obtained indirectly via a single discrete Fourier Transform (Fig.6) for corresponding parameters and compared to the ones gathered from the SC of the system.

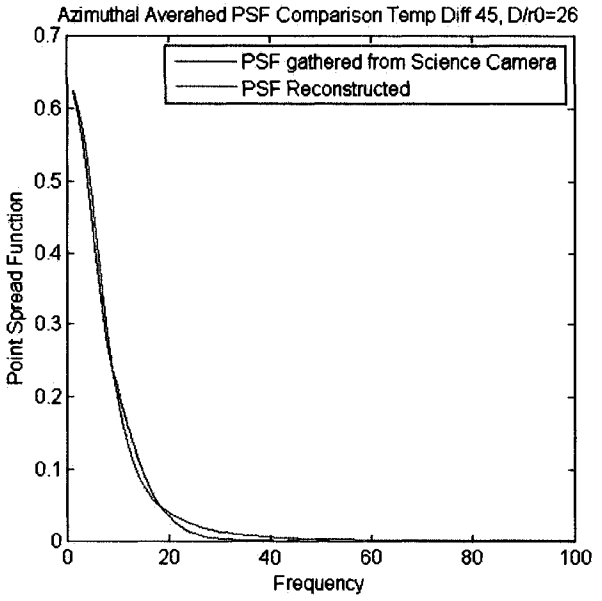


**Figure 6: Experimental PSF Reconstruction Results from the W/T Bench at $D/r_0$= 26**

In Fig. 6, it can be seen that the core of the PSF and the overall PSF is shows a good reconstruction.

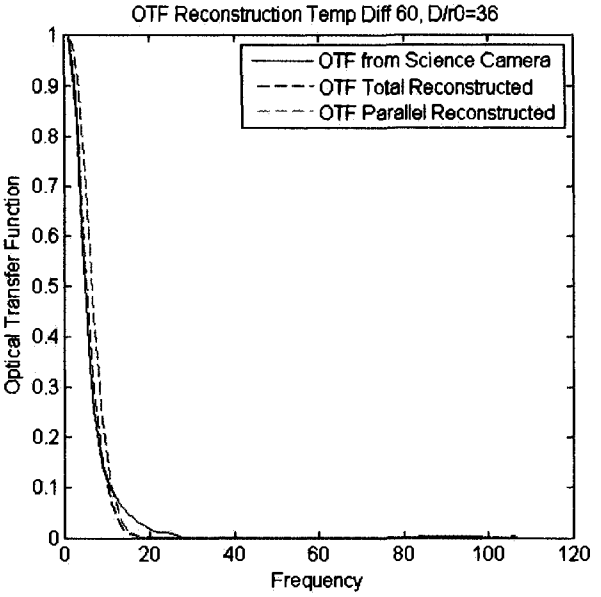


**Figure 7: Experimental OTF Reconstruction Results from the W/T Bench at $D/r_0$= 36**

Fig.7 represents the OTF comparison at Temp Diff 60°C and at $D/r_0$=36 and a Strehl Ratio of %61. The good agreement between the single dimensional cuts of the azimuthally averaged OTFs obtained from the AO corrected image can be seen.

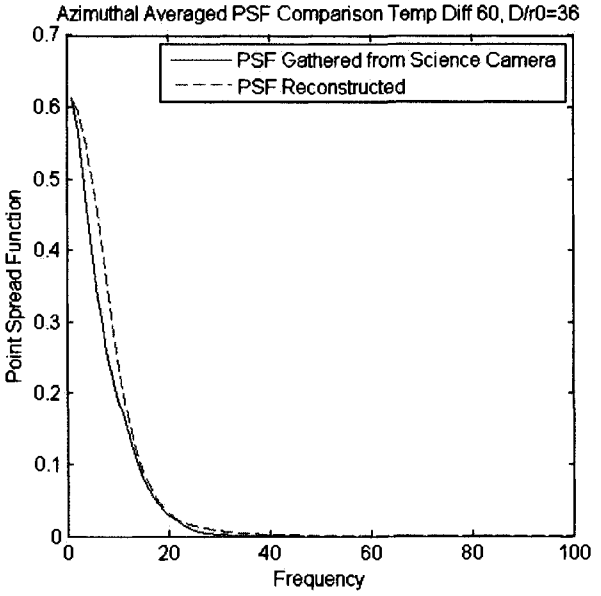


**Figure 8: Experimental PSF Reconstruction Results at $D/r_0$= 36**

On Fig. 8 there is a slight discrepancy on the core of the reconstructed PSF. This discrepancy is on the low frequency part of the reconstructed PSF and it means that the AO system was not able to perform a good correction ($\varphi_P$ was not accurate), whereas the high frequency part of the reconstructed PSF is in good agreement with the PSF gathered from the SC of the system (the $r_0$ extraction was accurate).

In Figure 9 and 10, the OTF and PSF comparisons can be seen for a Temp Diff 30°C and at $D/r_0$=14 and a Strehl Ratio of %71. In Fig. 9, there is an inconsistency between the single dimensional cuts of the azimuthally averaged OTFs obtained from the AO corrected image and the OTFs reconstructed from the SH WFS data.

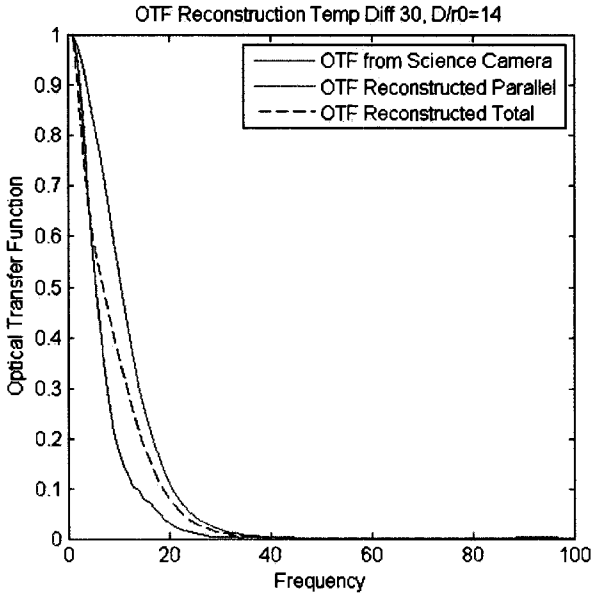


**Figure 9: Experimental OTF Reconstruction Results from the W/T Bench at $D/r_0$= 14**

This inconsistency is due to the fact that the turbulence is not fully developed accordingly to the Kolmogorov turbulence regime (due to heat dissipation before mixing), and that the AoA variance calculation does not hold.

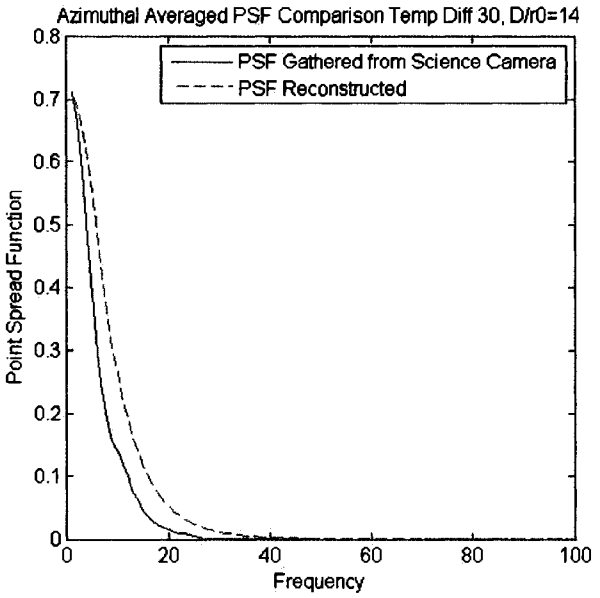


**Figure 10: Experimental PSF Reconstruction Results at $D/r_0$= 14**

From the estimated long exposure OTFs, the azimuthally averaged PSFs are obtained indirectly via a single discrete Fourier Transform (Fig.10) for corresponding parameters and compared to the ones gathered from the SC of the system. Though the inconsistency can be seen in the reconstructed PSF, it can be concluded that the methodology used on the reconstruction process is only valid under an accurate estimation of the contribution from the high order component (estimated from the Kolmogorov model of the turbulence) of the phase which is not corrected by the AO system.

To aid in the comparison of the results, both real and reconstructed OTF plots are scaled so that the maximums of the real OTFs and the OTFs reconstructed are 1. The PSF plots are scaled to the Strehl ratio which is a measure used for determination of the quality of an imaging system or of the wavefront after propagation through turbulence. The Strehl ratio is also known as the ratio of the peak intensity of the measured PSF to the theoretical maximum.

## 5. Conclusions

The results presented in this paper consist of the demonstration of the use of the WFS measurements and the DM commands in order to estimate the long exposure PSF of a multi-DM AO system using a TT mirror, a WR and a TR for correction. The data used in the estimation of the PSF is gathered from the control computer after each acquisition. It is further demonstrated that the long exposure OTF, in the case of N number of DMs, may still be expressed as the product of a static contribution (auto-correlation of the telescope's pupil in absence of atmospheric turbulence), a contribution from the DM components of the phase (partially corrected by the AO system), and a contribution from the high order component of the phase which is not corrected by the AO system due to the limitations of the DMs and the WFS. This high order component is estimated from the Kolmogorov model of the turbulence, and the $D/r_0$ is derived by the Angle of Arrival variances for an accurate estimation of this high order component. The remaining error is defined as the aliasing and cross-coupling between the DM and the high order component.

The good agreements between the numerical and experimental evaluation of the reconstructed OTFs and PSFs comparisons ensured the successful implementation of the methodology. Overall, it can be concluded that the improved methodology allows a good reconstruction of the PSF once the $D/r_0$ is accurately established in order to assess the multi-DM AO system performance. It must be noted that the reconstructed PSF is valid only within the isoplanatic patch.

The future work will be the evaluation of the methodology in a similar architecture but with different DMs (1K DM for the TR and a piezo-stack DM for the WR). Also off-

axis PSF Reconstruction for AO systems as a general objective, the complexity of the model and of the experimental set-up will then be gradually extended from a single light source to multi-light source scheme and possible implementation of new techniques will be investigated in order to accommodate for the anisoplanatic errors which can degrade the performance of the AO systems at greater angular distances from the target object. In that sense, the availability of UVic AO laboratory W/T dual DM bench offers a unique opportunity to test the techniques developed in the theoretical part of the work on real hardware.

## 6. References

[1] J.P. Veran, F.Rigaut, H. Maiter, and D. Rouan, "Estimation of the adaptive optics long exposure point spread function using control loop data," *J. Opt. Soc. Am.* A, 14, (1997).

[2] J.P. Veran, "Estimation de la reponse impulsionelle et restauration d'image en optiique adaptative: Application au system d'optique adaptative du telescope Canada-France-Hawaii," *Ecole National Superieure des Telecommunications, Thesis*, (1997).

[3] S. Harder, A. Chelli, "Estimating the point spread function of the adaptive optics system ADONIS using the wavefront sensor measurements," *A&AS*, 142, 119, (2000).

[4] Fitzgerald M. in The 1st Victoria Workshop on AO-PSF reconstruction, ed. L. Jollissaint, J.-P. Veran, J. Christou, & T. Rimmele, http://cfao.ucolick.org/meetings/psf reconstruction, (2004).

[5] L. Jolissaint, J.P. Veran, "OPERA, an automatic PSF reconstruction software for Shack-Hartmann AO systems: application to Altair," *Proc. SPIE*, volume 5490, 151-163, (2004).

[6] E. Gendron, Y. Clénet, T. Fusco, G. Rousset, "New algorithms for adaptive optics point-spread function reconstruction," *Astronomy and Astrophysics*, Volume 457, Issue 1, pp.359-363, (2006).

[7] O. Keskin, R. Conan, C. Bradley, "Point spread function reconstruction from Woofer-Tweeter adaptive optics bench," *Advances in Adaptive Optics II*, volume 6272. Proc. SPIE, (2006).

[8] Roddier, "Adaptive Optics in Astronomy," Cambridge University Press, pp.15, (1999).

[9] V. I. Tatarski, "Wave propagation in a turbulent medium," Dower Publications, New York, (1961).

[10] J. Hermann, "Cross coupling and aliasing in modal wave front estimation," *J. Opt. Soc. Am.*, 71(8): 989-992, (1981).

[11] O. Keskin, L. Jolissaint, C. Bradley, "Hot-air optical turbulence generator for the testing of adaptive optics systems: principles and characterization," *Applied Optics*, Vol. 45, Issue 20, pp. 4888-4897, (2006).

[12] O. Cugat, S. Basrour, C. Divoux, P. Mounaix, and G. Reyne, "Deformable magnetic mirror for adaptive optics: technological aspects," *Sensors and Actuators* A89, 1-9, (2001).

[13] URL http://www.alpao.fr/

[14] D. L. Fried, "Least-squares fitting a wave-front distortion estimate to an array of phase-difference measurements," *J. Opt. Soc. Am.* 67, 370–375, (1977).

[15] R.Conan, C. Bradley, P. Hampton, O. Keskin, A. Hilton and C. Blain, "Distributed modal command for a two deformable mirror Adaptive Optics System,", *Applied Optics*, Vol. 46, No. 20, 4329-4340, (2007).

[16] R. Conan, P. Hampton, C. Bradley, O. Keskin, "The woofer-tweeter experiment," *Proc. SPIE*, Advances in Adaptive Optics II, Vol. 6272., (2006).

[17] D. L. Fried, "Optical resolution through a randomly inhomogeneous medium for very long and very short exposures," *J. Opt. Soc. Am.* 56, (1966).

[18] F. Roddier, "The effects of atmospheric turbulence in optical astronomy" E. Wolf Edition, Progress in Optics 19, (1981).

[19] E. Masciadri, J. Vernin, "Optical technique for inner-scale measurement: possible astronomical applications," *Applied Optics*. 36, pp. 1320-1327, (1997).

[20] A.N. Kolmogorov, "Local structure of turbulence in incompressible fluids with very high Reynold's number," *Dokl, Akad. Nauk SSSR*, 30(4), 301-305, (1941).

# Appendix D:

## *Derivation and numerical evaluation of an off-axis point spread function reconstruction from woofer/tweeter adaptive optics system*

**Optical Engineering**

**Under Review (2008)**

# Derivation and Numerical Evaluation of an Off-Axis Point Spread Function Reconstruction from a Dual Deformable Mirror Adaptive Optics System

**O. Keskin[1], R. Conan[1], C. Bradley[1]**

*University of Victoria, Adaptive Optics Laboratory, Engineering Lab Wing B 133,*

*PO Box 3055 STN CSC, Victoria, BC, Canada, V8W 3P6,*

*Phone: +1 (250) 721 8624*

*Fax: +1 (250) 721 6500*

*[1]Department of Mechanical Engineering*

*okeskin@me.uvic.ca, rconan@uvic.ca, cbr@me.uvic.ca*

**Keywords:** Adaptive Optics, Point Spread Functions, Off-Axis Point Spread Functions

**Abstract:** This paper presents the derivation, implementation and testing of an off-axis Point Spread Function (PSF) reconstruction technique for the University of Victoria's dual Deformable Mirror (DM) Woofer-Tweeter (W/T) Adaptive Optics (AO) system. The methodology has been tested on numerical model; it is based on the data saved by the AO system during the science exposure, and on the analytical expression of the anisoplanatic transfer function. This data is later used in the post-processing stage to reconstruct the off-axis PSF that degrades the AO system's performance at greater angular distances from the guide star (GS). Although the results are unique to the UVic W/T AO bench, the proposed PSF

reconstruction methodology will be applicable to other dual DM systems and to multi DM AO systems.

## 1. Introduction

The RMS amplitude of turbulence-induced wavefront distortions increases with the five-sixths power of the telescope aperture diameter $D$ [1], while at the same time the number of DM degrees of freedom required to compensate the distortions to any given level of correction is growing as $D^2$. Extremely Large Telescopes (ELTs) will have primary mirror diameters that are at least 3 times larger than the current major optical telescopes. This would require DMs with at least 2.5 times greater stroke and 9 times the number of actuators to achieve equivalent correction comparable to current AO systems. It appears that, due to the unavailability of a manufacturing technology for such a DM, it will not be possible to satisfy both of these requirements for the ELTs with a single high-order-high-stroke DM. The power spectrum of the atmospheric turbulence follows a decaying ($f^{-11/3}$) power law [2]. Therefore, most of the turbulence energy is concentrated at low spatial frequencies and requires large stroke for correcting the first modes of the atmospheric turbulence; whereas at high spatial frequencies, the stroke requirement for the AO correction drops substantially. A solution to this problem is the use of dual DMs; the so called W/T configuration. In W/T architecture, the Woofer (WR) is a low-order-high-stroke DM used to compensate for the low-frequency effects introduced by the atmospheric turbulence. The Tweeter (TR) is a high-order-low-stroke DM used to compensate for the high-frequency effects. Having dual DMs allows the W/T AO system to have a high degree of correction of large amplitude wavefront distortion.

An AO system senses the degree of aberration in the phase of the incoming wave-front that arises from atmospheric turbulence, and compensates for his aberration. The correction provided by the AO system is valid in the direction of the guide star but degrades at greater angular distances from the GS. This is called anisoplanatism and it occurs from the cuts within the columns of turbulent atmosphere in the path of light from the guide star and of the light from a target object at an angular offset. Anisoplanatism depends on a number of parameters, namely: the vertical distribution of turbulence, angular offset from the reference source, the zenith angle, and the telescope's aperture. The vertical distribution of turbulence, at higher altitudes, generates greater anisoplanatic errors due to the larger geometric cut between the columns of atmosphere. The illustration of anisoplanatism can be seen in Figure 1.

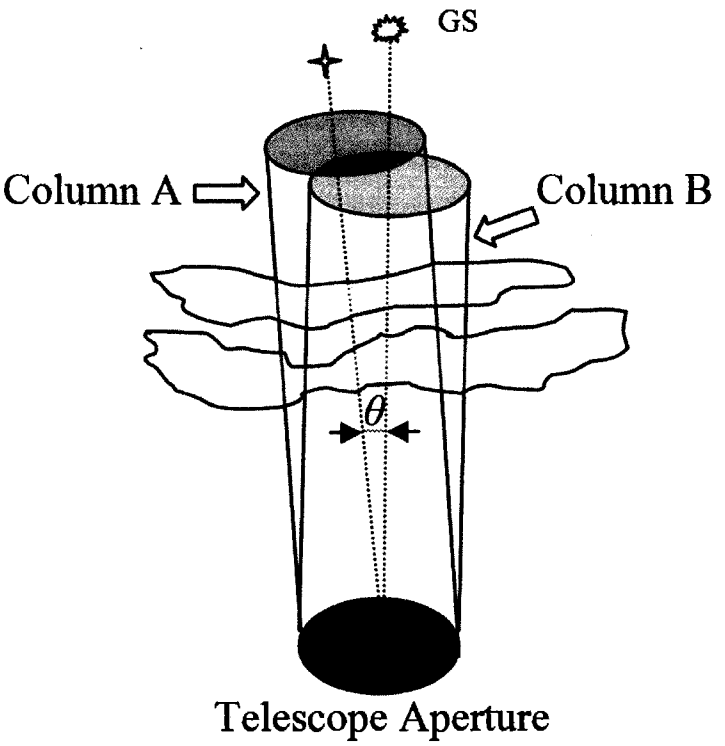


**Figure 1: Illustration of anisoplanatism**

In order to overcome the anisoplanatism effects, several approaches have been implemented. One is to estimate a reference PSF from an observed data, and use it in a field, within the isoplanatic angle, where multiple point sources can be deconvolved using this reference PSF. In this case the reference PSF may be assumed to be field independent [Christou, dePater], but these approaches do not account for the temporal evolution of the turbulence profile [Steinbring]. Nevertheless, the comparison of the Strehl degradation due to anisoplanatism measured from the image data and the PSF degradation expected from the measured turbulence profiles have shown a promising level of agreement between predictions and measurements [Voitsekhovich, Fusco, Weiss, and Britton]. Therefore, measurements of the turbulence profile have been used in estimating the off-axis PSF from the AO observations, and an improved off-axis PSF reconstruction methodology has been developed for the W/T AO architecture.

## 4. Point Spread Function

The position coordinates of the image plane (also called focal plane of the science camera (SC)) is $\vec{\alpha}$. The object plane, $\vec{\beta}$, is considered to be at an infinite distance from the image plane. These planes, $\vec{\alpha}$ and $\vec{\beta}$, are orthogonal to the optical axis.

The intensity distribution of the object across the object plane is $O(\vec{\beta})$. Similarly the intensity distribution of the long exposure image measured on the SC is $I(\vec{\alpha})$. The formation of an image through an AO system can then be defined as

$$I(\vec{\alpha}) = \int O(\vec{\beta})\, PSF(\vec{\alpha}, \vec{\beta})\, d\vec{\beta} \qquad \textbf{(1)}$$

The PSF of the point source represents the intensity received at the point $\vec{\alpha}$ of the image plane when the point-like object's intensity at position $\vec{\beta}$ is observed.

The isoplanatic patch is the area where the distortion level of the atmospheric turbulence is statistically the same everywhere in the field. It is generally assumed that the long exposure PSF has the same shape regardless of the viewing direction within this isoplanatic patch (i.e. $PSF\ (\vec{\alpha},\vec{\beta}) = PSF\ (\vec{\alpha}-\vec{\beta})$ [10,11]. Equation 1 can then be rewritten as a convolution

$$I\ (\vec{\alpha}) = \int O\ (\vec{\beta})\ PSF\ (\vec{\alpha}-\vec{\beta})\ d\vec{\beta} = O\ (\vec{\alpha}) \otimes PSF\ (\vec{\alpha}) \qquad \textbf{(2)}$$

In the Fourier domain, this convolution becomes a product

$$\tilde{I}(\vec{f}) = \tilde{O}\ (\vec{f})\ .\ OTF\ (\vec{f}) \qquad \textbf{(3)}$$

where OTF is the optical transfer function of the AO system.

The relation between the AO system imaging performance and the characterization of the residual error using the GS PSF of the AO correction will be described in the following sections.

So far only one PSF reconstruction tool has been implemented for operational use on an astronomical telescope: Veran's [10,11] code for the Canada-France-Hawaii Telescope (CFHT) Adaptive Optics Bonnette (also called PUEO). Although the original method was developed using the curvature WFS, the algorithm was later adapted and applied to Shack Hartmann WFS (SH WFS) [12,13,14,15]. In the W/T AO Bench, the methodology is also applied to SH WFS [16].

**Methodology**

The system optical transfer function (OTF) in the direction of the object of interest that differs from the GS is the product of anisoplanatic OTF, AO system OTF, and telescope OTF, as given in Equation 4. It is assumed that the OTF is stationary over the pupil; and is not dependent on the direction of the observation; and is dependent on the separation $\rho$. This permits the factorization of the anisoplanatic and of the guide star's OTFs.

$$OTF(\vec{\rho},\lambda)_{Total} = OTF(\vec{\rho},\lambda)_{Anisoplanatic}.OTF(\vec{\rho},\lambda)_{AO}.OTF(\vec{\rho},\lambda)_{TEL} \quad \textbf{(4)}$$

The $OTF_{TEL}$ is ideally the auto-correlation of the telescopes pupil, but in practice it also contains the effects of uncorrected static aberrations of the telescope. In the case of $OTF_{Anisoplanatic}$ the degree of anisoplanatism is determined by the turbulence profile, $OTF_{AO}$ is the OTF of the sum of the phase of the turbulent atmosphere and of the DM shapes. The phase of the turbulent atmosphere is a function of time. The DM shape opposes the turbulent phase which results in a residual phase that is also a function of time. This residual turbulence must be estimated for each sample of the AO system in order to be able to determine the long exposure PSF.

$OTF_{AO}$ can be given as

$$OTF(\vec{\rho},\lambda)_{AO} = \exp\left[-\frac{1}{2}\left(D_{\varphi_P}(\vec{\rho}) + D_{\varphi_O}(\vec{\rho})\right)\right] \quad \textbf{(5)}$$

and $OTF_{Anisoplanatic}$ is the optical transfer function of the object of interest's distance from

$$OTF(\vec{\rho},\lambda)_{Anisoplanatic} = \exp\left[-\frac{1}{2}\left(D_{\varphi_{Ani}}(\vec{\rho})\right)\right] \quad \textbf{(6)}$$

and $OTF_{total}$ given in the Equation 7 represents Equation 4 in terms of the structure functions [19,20,21]

$$OTF(\vec{\rho},\lambda)_{total} = \exp\left[-\frac{1}{2}\left(D_{\varphi_{Ani}}(\vec{\rho})\right)\right] \times \int P(r)P(r+\rho)dr \exp\left[-\frac{1}{2}\left(D_{\varphi_P}(\vec{\rho}) + D_{\varphi_O}(\vec{\rho})\right)\right] \quad (7)$$

The determination of the OTF also leads to the determination of the estimated long exposure PSF via a single discrete Fourier Transform.

The WFS measurements *(w)* determine the residual phase. In the W/T AO system the phase aberrations in the direction of the guide star ($\varphi_{Guide\ Star}(r)$) are measured, and compensated for by the tip/tilt mirror and two distinct DMs namely the Woofer and the Tweeter. Here $(r)$ is a vector in the pupil plane. The partial correction provided by the W/T AO system is due to the finite sampling of the wavefront sensor (WFS), the DMs and the finite bandwidth of the overall system. Therefore, the residual phase aberrations are present in the GS's wave-front after adaptive compensation. The source of this residual error are the high spatial frequencies introduced by the atmospheric turbulence (which is not corrected by the AO system), therefore the residual wave-front aberration of this object can be called $\varphi_{Anisoplanatic}(r)$.

If one represents the total residual phase aberrations after the AO correction by $\varphi_{tot}(r, \theta)$ in the direction of the object of interest, the residual aberrations after AO compensation will be:

$$\varphi_{tot}(\vec{\theta}) = \varphi_{Anisoplanatic}(\vec{\theta}) - \varphi_{Guide\,Star}(0) + \varphi_P(0) + \varphi_O(0) \quad (8)$$

where $\theta$ is the altitude dependent angular separation between the GS and the object of interest.

Note that in this equation the effect of the time delay is not taken into account. This delay represents time for which the wind pushes the turbulence past the telescope

aperture; this also causes a servo error in the guide star wave-front [9]. Additionally, the evolution of turbulence induces correlations between the wave-front aberrations in the direction of the object of interest and the AO correction. (i) $\varphi_P$, parallel component contains low frequency component up to the DMs cut-off frequency, and (ii) $\varphi_O$, orthogonal component is composed of the high spatial frequency that is beyond the spatial cut-off frequency of the DM. Here $\varphi_P$ and $\varphi_O$ are orthogonal to each other, and $\varphi_O$ will be estimated from the Kolmogorov model of the turbulence since the spatial frequencies of $\varphi_O$ is beyond the WFS cut-off frequency.

**Estimation of the $\varphi_P$**

As an improvement to Veran's approach, in the presence of W/T AO bench tip/tilt mirror (TT), woofer (WR), and tweeter (TR) the geometry of the system changes. In this TT + WR + TR architecture, $\varphi_P$ can be given by

$$\varphi_P(\vec{r},t) = \sum_{i=1}^{N_{TT\ mirror}} \varepsilon_i(t) M_{i\,tt\ mirror}(\vec{r}) + \sum_{i=1}^{N_{woofer}} \varepsilon_i(t) M_{i\,woofer}(\vec{r}) + \sum_{i=1}^{N_{tweeter}} \varepsilon_i(t) M_{i\,tweeter}(\vec{r}) \qquad (9)$$

Where $M$ is influence functions of the mirrors in DM vector space, *and* $\varepsilon$ are the mirrors residual phase coefficients.

$$\varepsilon(t) = D^{+} w(t) \qquad (10)$$

$D^{+}$ is the command matrix for the W/T system deduced from the pseudo-inverse of the interaction matrix $D$, and $w$ is the closed loop measurements.

When all the mirrors are running together, the DM vector space, $M_{itotal}$, can be expressed as the concatenation of vectors

$$M_{i_{total}} = \left\lfloor M_{i_{tt\ mirror}} \quad M_{i_{woofer}} \quad M_{i_{tweeter}} \right\rfloor \qquad (11)$$

It must also be noted that TT, WR, and TR modes are orthogonal to each other, and $N_{total}$ (number of modes) becomes,

$$N_{total} = N_{TTmirror} + N_{woofer} + N_{tweeter} \tag{12}$$

and Equation 6 can be simplified to

$$\varphi_P(\vec{r},t) = \sum_{i=1}^{N_{total}} \varepsilon_i(t) M_{i\,total}(\vec{r}) \tag{13}$$

The parallel structure function of the residual phase is given by

$$D_{\varphi_P}(\vec{r},\vec{\rho}) = \left\langle \left| \varphi_P(\vec{r},t) - \varphi_P(\vec{r}+\vec{\rho},t) \right|^2 \right\rangle \tag{14}$$

The structure function of the parallel component of the phase can then be represented as

$$D_{\varphi_P}(\vec{r},\vec{\rho}) = \sum_{i=1}^{N_{total}} \sum_{j=1}^{N_{total}} \left\langle \varepsilon_i \varepsilon_j \right\rangle \left[ M_{i_{total}}(\vec{r}) - M_{i_{total}}(\vec{r}+\vec{\rho}) \right] \left[ M_{j_{total}}(\vec{r}) - M_{j_{total}}(\vec{r}+\vec{\rho}) \right] \tag{15}$$

and the pupil average structure function of the parallel components becomes

$$\bar{D}_{\varphi_P}(\rho) = \left\langle \frac{\iint_P P(r)P(r+\rho) D_{\varphi_P}(\vec{r},\vec{\rho}) dr}{\iint_P P(r)P(r+\rho) dr} \right\rangle \tag{16}$$

This can be rewritten in a simpler form

$$\bar{D}_{\varphi_P}(\vec{\rho}) = \sum_{i=1}^{N_{total}} \sum_{j=1}^{N_{total}} \left\langle \varepsilon_i \varepsilon_j \right\rangle \; U_{ij}(\vec{\rho}) \tag{17}$$

where $<\varepsilon_i\varepsilon_j>$ is the covariance matrix of the TT, WR, and TR mirror mode error commands. This is updated at each loop cycle.

$$\left\langle \varepsilon_i \varepsilon_j \right\rangle = D^+ \left\langle w_i w_j \right\rangle (D^+)' \tag{18}$$

$<\varepsilon_i\varepsilon_j>$ is also related to SH WFS measurement covariance matrix $<w_iw_j>$. The definition of $U_{ij}(\rho)$ can be found in the next section.

**The $U_{ij}(\rho)$ functions**

$U_{ij}(\vec{\rho})$ is the cross-correlation of the DM modes, and can be represented as:

$$U_{ij}(\vec{\rho}) = \frac{\int P(\vec{r})P(\vec{r}+\vec{\rho})\left[M_{i_{total}}(\vec{r}) - M_{i_{total}}(\vec{r}+\vec{\rho})\right]\left[M_{j_{total}}(\vec{r}) - M_{j_{total}}(\vec{r}+\vec{\rho})\right]d\vec{r}}{\int P(\vec{r})P(\vec{r}+\vec{\rho})d\vec{r}} \quad \textbf{(19)}$$

where $P(r)$ is the pupil function. The calculation of $U_{ij}(\rho)$ utilizes the Fourier transforms and the properties of the correlation function:

$$U_{ij}(\vec{\rho}) = \frac{F^{-1}\left\{2real\left[F(M_iM_jP)F*(P) - F(M_iP)F(M_jP)\right]\right\}}{F^{-1}(\left|F(P)\right|^2)} \quad \textbf{(20)}$$

In Equation 17, $F$ is the Fourier transform operator and * represents the complex conjugate. It must be noted that the calculation of $U_{ij}$ depends on the system geometry, and it is computationally long but it is calculated only once.

**Calculation of $\varphi_O$**

In the simulation, the structure function of the orthogonal component of the phase is computed using a Monte-Carlo model to generate phase screens; remove the mirror modes ($M_{itotal}$) out of each phase screen; and then compute the average of the structure function for the corrected phase screens.

The orthogonal structure function of the residual phase is given by

$$D_{\varphi_O}(\vec{r},\vec{\rho}) = \left\langle \left|\varphi_O(\vec{r},t) - \varphi_O(\vec{r}+\vec{\rho},t)\right|^2 \right\rangle \quad \textbf{(21)}$$

and its pupil average can be derived similarly

$$\bar{D}_{\varphi_o}(\rho) = \left\langle \frac{\iint_P P(r)P(r+\rho)D(\vec{r},\vec{\rho})dr}{\iint_P P(r)P(r+\rho)dr} \right\rangle \quad \textbf{(22)}$$

In the calculation of the orthogonal phase, it must be noted that the $r_0$, and the $L_0$ must be accurately estimated.

**The remaining error calculations**

The propagation of the WFS measurements error onto the mirror modes originates from the turbulent phase having a high order component which gives a non-zero measurement on the WFS, and is mistaken for a low order component through the estimation process. It depends on the statistics of $\varphi_o$ and can be derived from the WFS measurements. $\varphi_o$ is not corrected by the AO system, it can be assumed to be in good agreement with the Kolmogorov atmospheric turbulence model, and it is computed from the model. This error is a consequence of the finite spatial sampling of the WFS and it has been shown to be the combination of two effects [19], namely spatial aliasing and spatial cross-coupling. We will refer to it as the remaining error, $\varepsilon_r(t)$:

$$\varepsilon_r(t) = D^{+} w(\varphi_o(r,t)) \tag{23}$$

and the covariance matrix of the remaining error, $C_{rr}$ is calculated from the numerical model, and can be given as:

$$C_{rr} = \left\langle \varepsilon_r \varepsilon_r^{t} \right\rangle \tag{24}$$

Covariance matrix of the WR and TR mirror mode error commands then becomes:

$$\left\langle \varepsilon_i \varepsilon_j \right\rangle = D^{+} \left\langle w_i w_j \right\rangle (D^{+})^{t} + C_{rr} \tag{25}$$

To account for the remaining error, $\varepsilon_r(t)$, and its effect on the PSF reconstruction process, one can use Equation 25 instead of Equation 18 and then calculate the parallel component of the residual phase accordingly. Note that $C_{rr}$ is also calculated from the model.

**Calculation of the anisoplanatic structure function**

If one can simplify $\varphi_{Ani} = \varphi_{Anisoplanatic} - \varphi_{Guide\ Star}$ and $\varphi_{AO} = \varphi_P + \varphi_O$, the structure function for the $\varphi_{total}$ can be written as

$$D_{\varphi_{tot}}(r_1, r_2) = D_{Ani}(r_1, r_2) + D_{AO}(r_1, r_2) + 2\left\langle \left| \varphi_{Ani}(r_1)\varphi_{AO}(r_1) + \varphi_{Ani}(r_2)\varphi_{AO}(r_2) - \varphi_{Ani}(r_1)\varphi_{AO}(r_2) - \varphi_{Ani}(r_2)\varphi_{AO}(r_1) \right| \right\rangle \quad (26)$$

The cross-terms in the Equation represent the spatial correlations between the residual phase errors from the anisoplanatism and those from the adaptive optics correction. In AO corrections there are number of errors that do not have correlation with anisoplanatism, namely: aberrations in the optical system, non-common path errors, and measurement errors. While the importance of those errors varies from an AO system's error budget to another, in general the cross-term in Equation 26 will be very small relative to the structure functions. Therefore, those cross-terms are neglected.

The structure function $D_{Ani}$ of the anisoplanatic component of the phase can then be represented as

$$D_{Ani}(r_1, r_2) = 2\Xi k^2 D^{5/3} \times \int_0^\infty C_N^2(z)dz \left\{ 2|\Omega|^{5/3} + 2\left|\frac{2}{D}(r_1 - r_2)\right|^{5/3} - 2\left|\frac{2}{D}(r_1 - r_2) + \Omega\right|^{5/3} - 2\left|\frac{2}{D}(r_1 - r_2) - \Omega\right|^{5/3} \right\} \quad (27)$$

Note that the anisoplanatic structure function is defined as a function of $r_1$-$r_2$. It is assumed that this $D_{ani}$ is stationary over the pupil plane. Also $D_{Ani}$ is dependent on the telescope's aperture diameter, turbulence profile, angular separation between the guide star and the object of interest, and the observing wavelength.

## 5. Working Principle of the Woofer/Tweeter (W/T) AO System

In order to validate the PSF reconstruction method, numerical modeling is performed. The end-to-end model is entirely coded with Matlab using object-oriented programming, and it is comprised of the models of the optical elements of the W/T AO bench [23].

The principle of operation of the UVic W/T AO system is illustrated in Figure 2. A planar wavefront, generated by a collimated point light source, goes through the hot-air atmospheric turbulence generator [22] and becomes aberrated. Using a hot-air atmospheric turbulence generator is an alternative to other techniques in simulating the optical effect of atmospheric turbulence, (e.g. etched rotating phase screens that are expensive to manufacture and do not allow turbulence strength adjustment). This limitation prevents real-time assessment of AO control system performance versus turbulence strength and particularly high-$\sigma$ events (e.g. sudden bursts of turbulence). The degree of distortion of the wavefront is detected by the SH WFS. The purpose of the W/T AO system is to make this distorted wavefront as flat as possible. TT mirror is a flat mirror which adjusts the tip/tilt position offsets of the incoming distorted wavefront by counteracting the apparent motion of the star. Both DMs use a grid of actuators to deform their physical shape to an opposing shape of the distorted wavefront. In the wavefront compensation process, the commands of both WR and TR and also the command of the TT mirror are determined by the AO controller (in closed loop), which uses the SH WFS measurements. During this closed loop operation the WFS measures only the residual wavefront error reflected onto the DMs and the TT mirror (i.e. the uncorrected phase distortions of the wavefront). This process takes place in real-time to compensate for the constantly changing optical effects of the atmospheric turbulence.

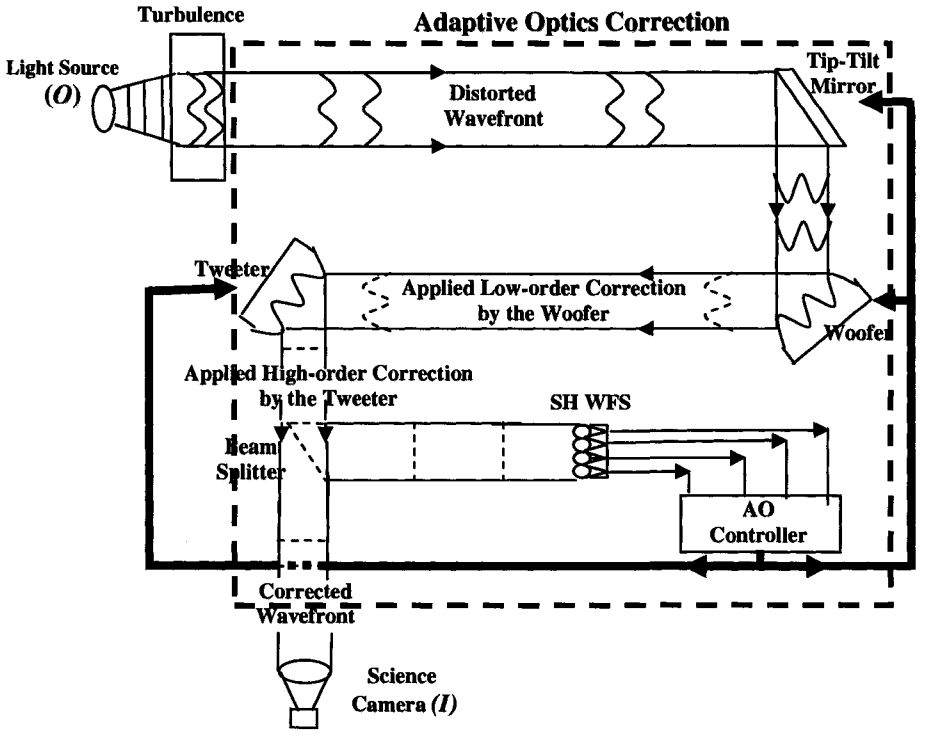


**Figure 2: Working Scheme of the W/T AO Bench (dashed lines represent AO correction)**

The wavefront that leaves the AO system is ideally flat when it strikes the science instrument. The science instrument can be a camera, spectrograph, coronagraph, or an interferometer. For AO system commissioning and PSF reconstruction verification, at the UVic AO bench, a camera is chosen as the science instrument. The role of the science camera (SC) is to capture images of the corrected long exposure PSF, *I*, gathered during an observation of the point source, *O*.

**Numerical Results from the Guide Star**

Atmospheric turbulence is introduced by a phase screen, set at 10km in the atmosphere, generated using a Monte Carlo model of1000 iterations. The parameters used in the simulation are: telescope diameter of 10m; a $D/r_0$ of 8; sampling is 108, and the observing wavelength is 2.2 μm.

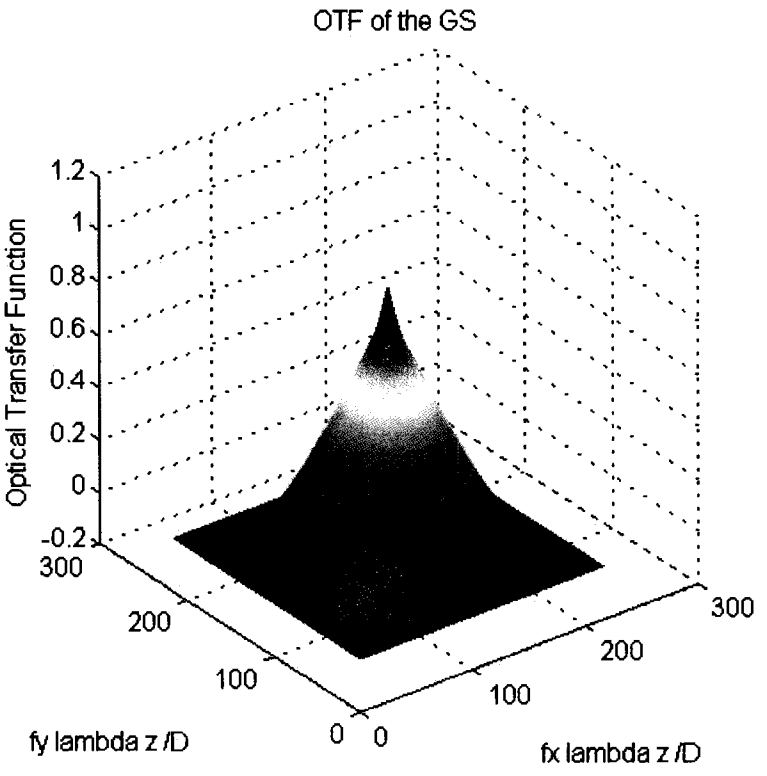


**Figure 3: The OTF of the Guide Star obtained from the SC of the Model**

The GS OTF is calculated from the wavefront sensor data. The product of the observed GS OTF and the anisoplanatic transfer function provides the predicted $OTF_{total}$ in the direction of the object of interest.

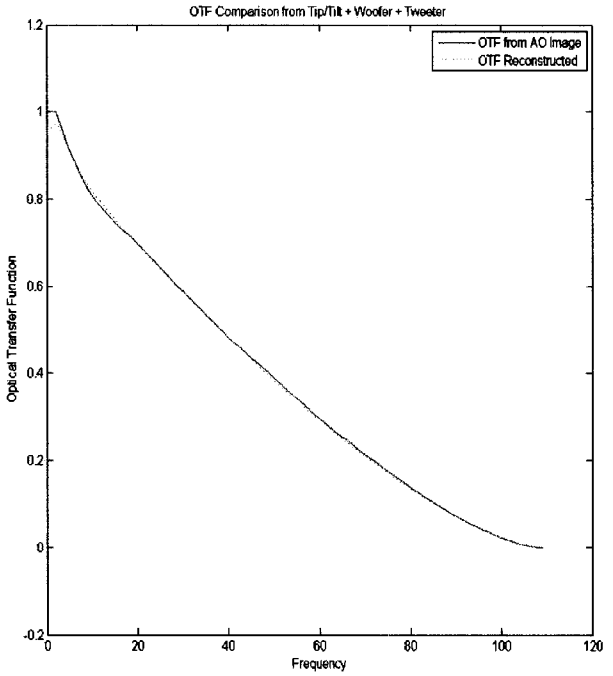


**Figure 4: Numerical Modeling OTF Reconstruction Results**

The agreement between the single dimensional cuts of the OTF obtained from the AO corrected image and the OTF reconstructed from the SH WFS data (Fig.3) ensured that a successful reconstruction was achieved in the direction of the GS through the correct implementation of the methodology.

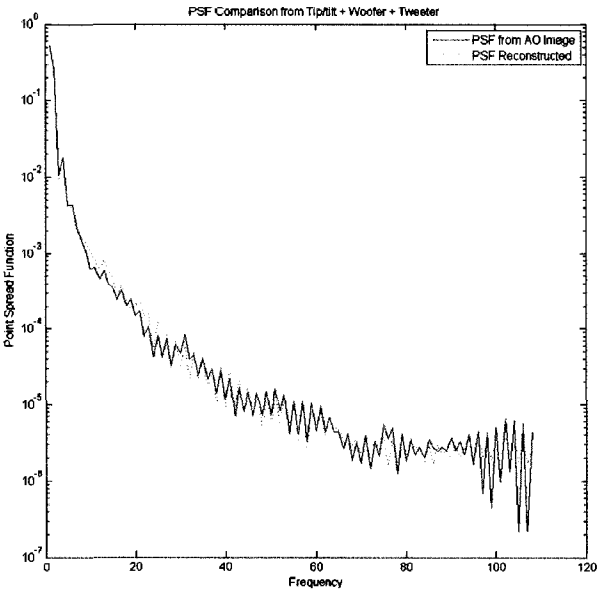


**Figure 5: Numerical Modeling PSF Reconstruction Results**

From the real and estimated long exposure GS OTFs, the long exposure real and reconstructed GS PSFs are obtained indirectly via a single discrete Fourier Transform (Fig. 4). In these results, the WFS and aliasing error are taken into account and the good agreement on both comparisons can be seen.

It must also be noted that, for a better comparison, both real and reconstructed OTF and PSF plots are scaled so that the maximums of the real OTF and PSF are 1. The parameters used in the simulation are chosen to be compatible with today's telescopes.

## Numerical Results in the Direction of the Object of Interest

**Target object set at 16 Arc seconds:** Figure 6 represents anisoplanatic transfer function for a target object at a *16''* offset from the GS, and it is computed through Equation 6. In the simulation the observing wavelength is 2.2 μm, for a 10 meter telescope. In this picture, due to anisoplanatism that is generated by orienting the target object in X-axis,

the anisotropy can be seen. But it must be noted that despite this anisotropy the structure function is stationary over the pupil plane.

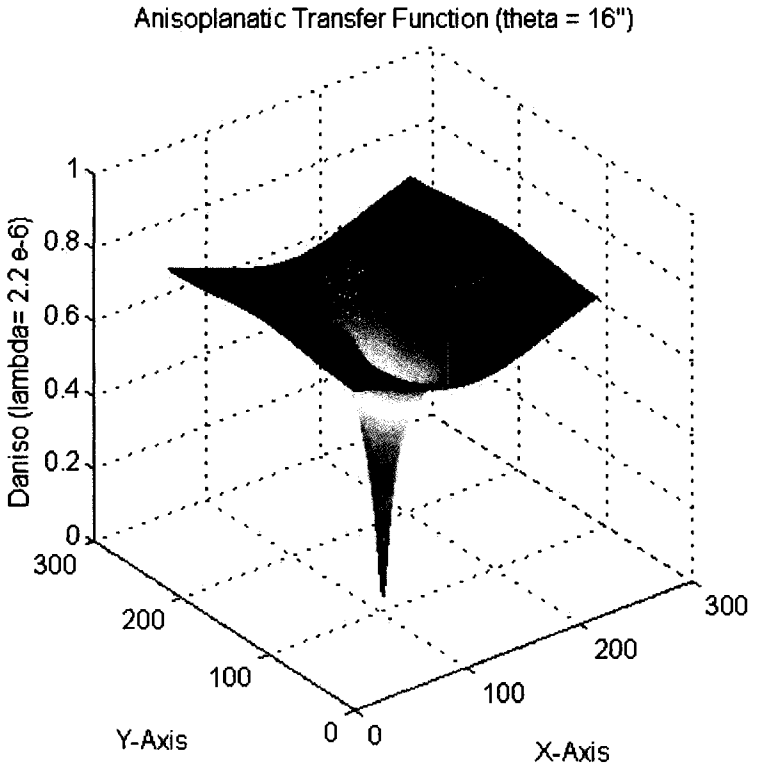


**Figure 6: Anisoplanatic Structure Function Calculated for 16" Angular Separation**

Figure 7 illustrates the reconstructed OTF from the target object. It is calculated using Equation 7, and it must be noted that even in the smaller angular offsets, degradation in the obtained final image from the AO system is noticeable. It must be noted that the $OTF_{Anisoplanatic}$ depends only on the anisoplanatic structure function. In the following results the remaining error (i.e. defined as the aliasing and cross-coupling between the DM and the high order component) is taken into account.

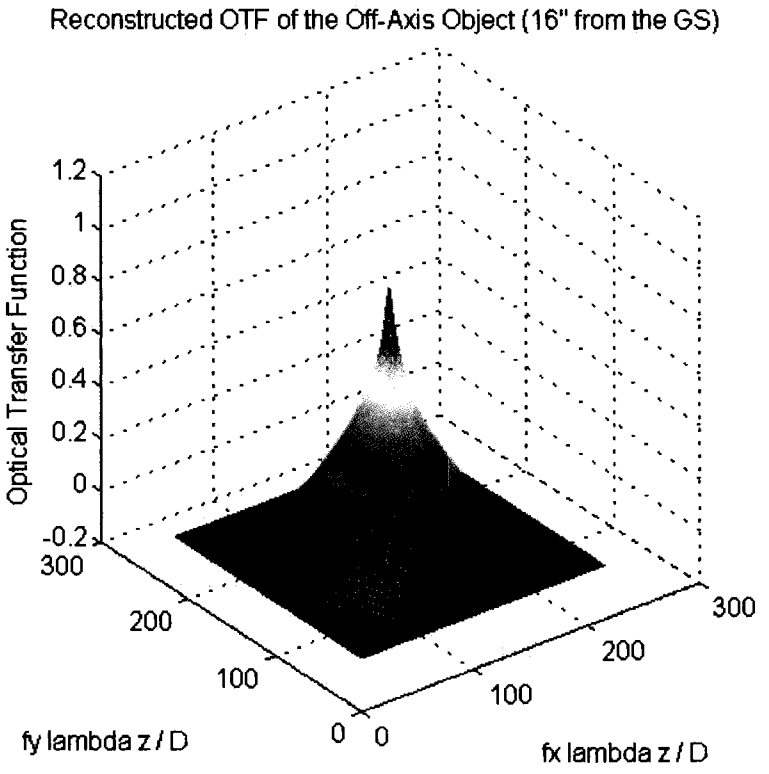


**Figure 7: Reconstructed OTF from the Target Object**

Figure 8 represents a comparison between the single dimensional cuts of the azimuthally averaged anisoplanatic OTFs obtained from the AO corrected image. The good agreement in this result ensured that a successful reconstruction was achieved through the correct implementation of the methodology.

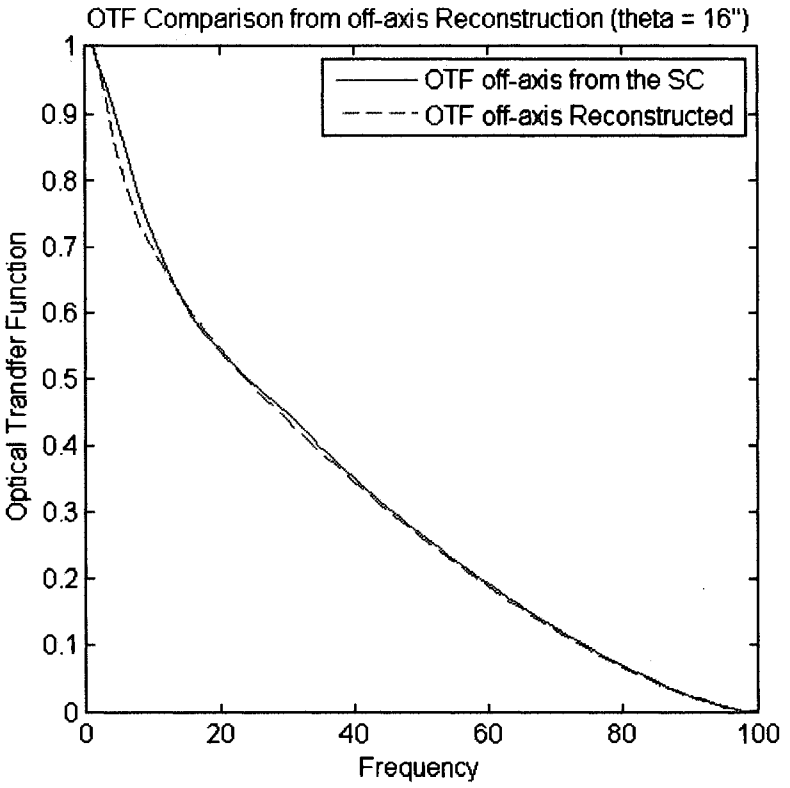


**Figure 8: Numerical Modeling Anisoplanatic OTF Reconstruction Results (16'' separation)**

It must be noted that in the case of 16 arc seconds separation the target object is at the half angular separation of the isoplanatic angle (32.5 arc seconds) defined in the numerical model.

**Target object set at 35 Arc seconds:** Figure 9 represents a comparison between the single dimensional cuts of the azimuthally averaged anisoplanatic OTFs obtained from the AO corrected image.

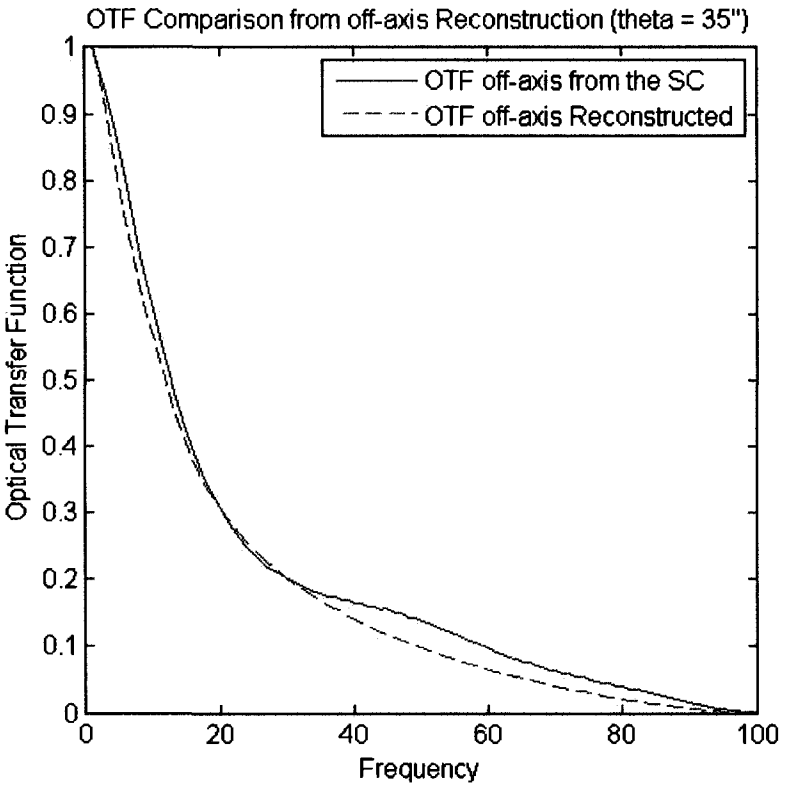


**Figure 9: Numerical Modeling Anisoplanatic OTF Reconstruction Results (35'' separation)**

It must be noted that in the case of 35 arc seconds separation the target object is very close to the angular separation of the isoplanatic angle (32.5 arc seconds) defined in the numerical model. In this result a slight discrepancy can be seen and it will be discussed in the next section, but overall it can still be noted that a good agreement in the overall reconstruction was achieved through the correct implementation of the methodology.

**Target object set at 50 Arc seconds:** Figure 10 represents a comparison between the single dimensional cuts of the azimuthally averaged anisoplanatic OTFs obtained from

the AO corrected image. The good agreement in this result ensured that a successful reconstruction was achieved through the correct implementation of the methodology.

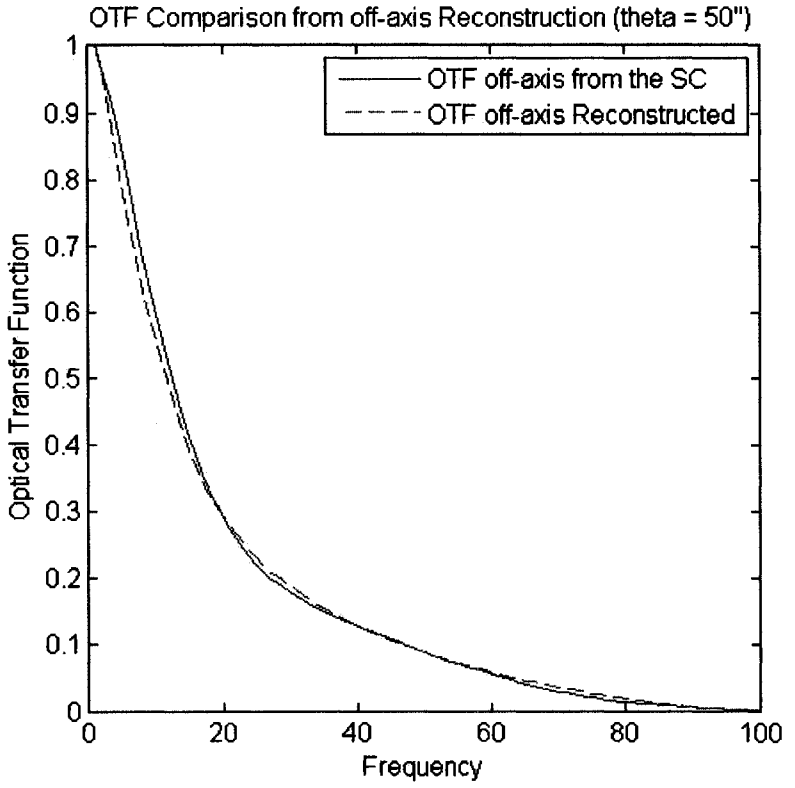


**Figure 10: Numerical Modeling Anisoplanatic OTF Reconstruction Results (50'' separation)**

It must be noted that in the case of 50 arc seconds separation the target object is significantly far from the angular separation of the isoplanatic angle (32.5 arc seconds) defined in the numerical model.

**Discussion of results**

In the reconstructed OTFs from target objects having 16, 35 and 50 arc second separations from the GS an overall good agreement can be seen from the ones gathered by the SC of the system and by the one reconstructed. In the case of 16 arc seconds angular separation, the GS and the target object are close to each other, therefore the anisoplanatism effect is small and the stationarity assumption of the OTF holds. In the case of 50 arc seconds angular separation, the target object and the GS are far from each other and the correlation between them is very small eventhough the effect of anisoplanatism is large. Here the stationarity assumption of the OTF still holds.

But in the case of 35 arc second angular separation, the discrepancy on the result arise from the fact that the OTF reconstruction algorithm is based on the stationarity of the OTF over the pupil plane. For this particular case, the correlation between the target object and the GS is strong, and the effect of anisoplanatism is large. It can be concluded that the stationarity assumption of the OTF is no longer valid.

**Conclusions**

The results presented in this paper consist of the demonstration of the use of the WFS measurements and the DM commands in order to estimate the long exposure PSF of a GS from a multi-DM AO system using a TT mirror, a WR and a TR for correction. The analytic methodology uses the observing wavelength, turbulence profile, angular offset, the aperture diameter, and the zenith angle in the prediction of the anisoplanatic PSF. For the GS PSF, data used in the estimation is gathered from the control computer after each acquisition. It is further demonstrated that the long exposure anisoplanatic OTF, in the

case of N number of DMs, may still be expressed as the product of a static contribution (auto-correlation of the telescope's pupil in absence of atmospheric turbulence), a contribution from the DM components of the phase (partially corrected by the AO system), a contribution from the high order component of the phase which is not corrected by the AO system due to the limitations of the DMs and the WFS, and a contribution from the anisoplanatic structure function. The remaining error is defined as the aliasing and cross-coupling between the DM and the high order component.

The good agreements between the reconstructed OTF and PSF comparisons ensured that the effect of anisoplanatism in AO compensated image quality can be improved by the successful implementation of the methodology. Overall, it can be concluded that the improved methodology allows a good reconstruction of the off-axis PSF once the turbulence profile is accurately established in order to assess the multi-DM AO system performance. It must be noted that the reconstructed OTF is valid only with the assumption that the OTF is stationary over the pupil plane. As it can be seen in the case of 35 arc seconds separation, due to the strong correlation between the two stars at the border of the isoplanatic angle and the strong anisoplanatism effect this assumption is no longer valid, which resulted on a slight discrepancy on the results.

The future work will be the experimental evaluation of the methodology in a similar architecture but with different DMs (1K DM for the TR and a piezo-stack DM for the WR). In that sense, the availability of UVic AO laboratory W/T dual DM bench offers a unique opportunity to test the techniques developed in the theoretical part of the work on real hardware.

**References**

[1] Roddier, "Adaptive Optics in Astronomy," Cambridge University Press, pp.15, (1999).

[2] V. I. Tatarski, "Wave propagation in a turbulent medium," Dower Publications, New York, (1961).

[3] J.C. Christou, G. Pugliese, R. Köhler, J. Drummond, "Photometric and astrometric analysis of AO images of crowded fields," PASP, 116, 734, (2004).

[4] I. de Pater, F. Marchis, B. A. Macintosh, H. G. Roe, D. Le Mignant, J. R. Graham and A. G. Davies, "Keck AO Observations of Io in and out of eclipse," *Icarus*, 169, 250-263., (2004).

[5] E. Steinbring, S. M. Faber, S. Hinkley, B. A. Macintosh, D. Gavel, E. L. Gates, J. C. Christou, M. Le Louarn, L. M. Raschke, Graham, J. P. Lloyd,, "Characterizing the Adaptive Optics Off-Axis Point-Spread Function. I. A Semiempirical Method for Use in Natural Guide Star Observations," PASP, 114, 1267-1280, (2002).

[6] V.V. Voitsekhovich, V.G. Orlov, S. Cuevas, R. Avila, "Efficiency of off-axis astronomical adaptive systems: Comparison of theoretical and experimental data," Astron. Astrophys. Suppl. Ser. 133, 427-430, (1998).

[7] T. Fusco, J.-M. Conan, L.M. Mugnier, V. Michau, G. Rousset, "Characterization of adaptive optics point spread function for anisoplanatic imaging. Application to stellar field deconvolution," Astron. Astrophys. Suppl. Ser. 142, 149-156 (2000).

[8] A. Weiss, S. Hippler, M. Kasper, N. Wooder, and J. Quartel, "Simultaneous measurements of the Fried parameter r0 and the isoplanatic angle 0 using SCIDAR and

adaptive optics - First results. In: Astronomical site evaluation in the visible and radio range," ASP Conf. Ser. 266, ASP, 86-95 (2002).

[9] M. Britton, "The Anisoplanatic Point-Spread Function in Adaptive Optics," The Publications of the Astronomical Society of the Pacific, Volume 118, Issue 844, pp. 885-900, (2006).

[10] J.P. Veran, F.Rigaut, H. Maiter, and D. Rouan, "Estimation of the adaptive optics long exposure point spread function using control loop data," *J. Opt. Soc. Am.* A, 14, (1997).

[11] J.P. Veran, "Estimation de la reponse impulsionelle et restauration d'image en optiique adaptative: Application au system d'optique adaptative du telescope Canada-France-Hawaii," *Ecole National Superieure des Telecommunications, Thesis*, (1997).

[12] S. Harder, A. Chelli, "Estimating the point spread function of the adaptive optics system ADONIS using the wavefront sensor measurements," *A&AS*, 142, 119, (2000).

[13] Fitzgerald M. in The 1st Victoria Workshop on AO-PSF reconstruction, ed. L. Jollissaint, J.-P. Veran, J. Christou, & T. Rimmele, http://cfao.ucolick.org/meetings/psf reconstruction, (2004).

[14] L. Jolissaint, J.P. Veran, "OPERA, an automatic PSF reconstruction software for Shack-Hartmann AO systems: application to Altair," *Proc. SPIE*, volume 5490, 151-163, (2004).

[15] E. Gendron, Y. Clénet, T. Fusco, G. Rousset, "New algorithms for adaptive optics point-spread function reconstruction," *Astronomy and Astrophysics*, Volume 457, Issue 1, pp.359-363, (2006).

[16] O. Keskin, R. Conan, C. Bradley, "Point spread function reconstruction from Woofer-Tweeter adaptive optics bench," *Advances in Adaptive Optics II*, volume 6272. Proc. SPIE, (2006).

[17] E. Masciadri, J. Vernin, "Optical technique for inner-scale measurement: possible astronomical applications," *Applied Optics*. 36, pp. 1320-1327, (1997).

[18] A.N. Kolmogorov, "Local structure of turbulence in incompressible fluids with very high Reynold's number," *Dokl, Akad. Nauk SSSR*, 30(4), 301-305, (1941).

[19] J. Hermann, "Cross coupling and aliasing in modal wave front estimation," *J. Opt. Soc. Am.*, 71(8): 989-992, (1981).

[20] D. L. Fried, "Anisoplanatism in adaptive optics," J. Opt. Soc. Am. Vol 72. N0.1, pp. 52, (1981).

[21] G.A. Tyler, "Merging: a new method for tomography through random media," J. Opt. Soc. Am., Vol. 1, No. 1, pp. 409, (1994).

[22] O. Keskin, L. Jolissaint, C. Bradley, "Hot-air optical turbulence generator for the testing of adaptive optics systems: principles and characterization," *Applied Optics*, Vol. 45, Issue 20, pp. 4888-4897, (2006).

[23] R. Conan, P. Hampton, C. Bradley, O. Keskin, "The woofer-tweeter experiment," *Proc. SPIE*, Advances in Adaptive Optics II, Vol. 6272., (2006).

# Appendix *E:*

## *Zernike polynomials*

# Zernike Polynomials

Zernike polynomials represent an orthonormal set over a circle. They are composed of sums of power series terms with appropriate normalizing factors, and are used in modeling to describe the phase aberrations caused by the atmosphere. Radial (index $n$), and azimuthal (index $m$) polynomials go before Zernike coefficients $A_{nm}$ and $B_{nm}$ that completely describe the wavefront up to the order specified by the largest $n$ or $m$. The Zernike series can be given as

$$\varphi(r,\theta) = A_{00} + \frac{1}{\sqrt{2}}\sum_{n=2}^{\infty} A_{n0}\Re_n^0\left(\frac{r}{R}\right) + \sum_{n=1}^{\infty}\sum_{m=1}^{n}(A_{nm}\cos(m\theta) + B_{nm}\sin(m\theta))\Re_n^m\left(\frac{r}{R}\right) \tag{1}$$

where the azimuthal polynomials are sines and cosines of multiple angles. For n-m=even $R$ is the radius of the circle over which the polynomials are defined. The radial polynomial can then be given as

$$\Re_n^m\left(\frac{r}{R}\right) = \sum_{s=0}^{\frac{n-m}{2}}(-1)^s \frac{(n-s)!}{s!(\frac{n+m}{2}-s)!(\frac{n-m}{2}-s)!}\left(\frac{r}{R}\right)^{n-2s} \tag{2}$$

Even though the polynomials appear to be complicated, they do have a number of features useful to adaptive optics. Zernike polynomials transform easily under Cartesian axes as they include a polynomial for each pair of radial (n) and azimuthal (m) order, and the coefficients of these series can be used in balancing of aberrations.

The first few radial terms for the Zernike polynomials are given in Table 2.

**Table 2 First few radial terms for Zernike Polynomials**

| | $n=0$ | $n=1$ | $n=2$ | $n=3$ | $n=4$ |
|---|---|---|---|---|---|
| $m=0$ | 1 | | $2r^2-1$ | | $6r^4-6r^2+1$ |
| $m=1$ | | $r$ | | $3r^3-2r$ | |
| $m=2$ | | | $r^2$ | | $4r^4-3r^2$ |
| $m=3$ | | | | $r^3$ | |
| $m=4$ | | | | | $r^4$ |

where, $n$ is the radial index, $m$ is the azimuthal index, and $r$ is the polar coordinate.